VNIVERSITAT DE VALÈNCIA

Composite scalars and dark matter from four-fermion interactions

PhD thesis submitted in fulfillment of the requirements of the “Programa de Doctorat en Física” in Facultat de Física, Universitat de València.

Author: **Leonardo Coito Pereyra**

Thesis Directors: **Prof. Arcadi Santamaria Luna**
Prof. Joannis Papavassiliou
Dr. Juan Andrés Herrero García

Date: July / 2022

Abstract

According to composite Higgs theories there is no fundamental scalar field in Nature and the Higgs boson is a composite state made of fermions from strong four-fermion interactions. The appeal of this dynamical framework lies in the fact that it can connect the dynamical generation of the SM particle masses, in particular the top quark and the Higgs boson, and the dynamical origin of EWSB. However, the SM particles alone can not provide predictions on m_t and m_H close to the measured values. Due to this, in the first part of this thesis we focus on improving both predictions by analyzing two types of models including new particles and/or interactions beyond the SM. A first model implements three different colored particles: $SU(3)_c$ triplet, sextet and octet (and $SU(2)_L$-doublet); the second assumes two new fundamental fermions: χ and a right-handed neutrino N, and establish the inverse seesaw scheme that leads to an explanation for light neutrino masses.

In the second part of the thesis, we aim at the consequences of two broad scenarios regarding the possibility of containing a good dark matter candidate. The analysis considers discrete Z_2 symmetries that render the candidates as stable and whose relic abundances are generated in the freeze-out mechanism.

Firstly, we examine whether four-fermion interactions between χ and N could lead to χ being a suitable dark matter candidate outside of the composite scheme. We focus the study of the DM phenomenology on the possible tree-level UV completions, and in particular the scenario in which the annihilation of dark matter to neutrinos is in t-channel. This set up fits into the well-known neutrino portal scenario.

The second scenario considers one of the simplest models containing a pseudo-Goldstone boson: the two-scalar SM-singlet case. There is a $O(2)$ global symmetry that is spontaneously and explicitly broken, and providing a discrete Z_2 symmetry the pseudo-Goldstone boson can be considered as a dark matter candidate. The phenomenology is analyzed on four minimal models containing different symmetry breaking patterns, with the purpose of recognizing disparate signatures in the physical observables.

List of publications

This PhD thesis is based on the following publications:

- *"Top quark mass from a nambu-jona-lasinio higgs with additional composite scalars"*, Work in progress (2022) [1].

- *"Composite Higgs bosons from neutrino condensates in an inverted seesaw scenario"*.

  Leonardo Coito (Valencia U., IFIC), Carlos Faubel (Valencia U., IFIC), Arcadi Santamaria (Valencia U., IFIC). Phys. Rev. D **101** (2020) 075009. [2].

- *"Dark matter from a complex scalar singlet: the role of dark CP and other discrete symmetries"*.

  Leonardo Coito (Valencia U., IFIC), Carlos Faubel (Valencia U., IFIC), Juan Herrero-García (Valencia U., IFIC), Arcadi Santamaria (Valencia U., IFIC).

  JHEP **11** (2021) 202 [3].

- *"Dark matter from a complex scalar singlet and preservation of its stabilising symmetry"*.

  Leonardo Coito (Valencia U., IFIC), Carlos Faubel (Valencia U., IFIC), Juan Herrero garcia (Valencia U., IFIC), Arcadi Santamaria (Valencia U., IFIC).

  Published in: PoS PANIC2021 (2022) 055.

- *"Sterile neutrino portals to Majorana dark matter: effective operators and UV completions"*.

  Leonardo Coito(Valencia U., IFIC), Carlos Faubel(Valencia U., IFIC), Juan Herrero-Garca(Valencia U., IFIC), Arcadi Santamaria(Valencia U., IFIC), Arsenii Titov(Valencia U., IFIC).

  `arXiv:2203.01946`. Accepted for publication in JHEP. [4].

Agradecimientos

Quisiera comenzar mis agradecimientos a las cuatro personas más importantes en mi educación académica y crecimiento como investigador.
Deseo expresar mi enorme gratitud a Arcadi Santamaria Luna, por guiarme a lo largo del doctorado con tanta dedicación, entusiasmo e inmenso apoyo. Agradezco profundamente a Juan Herrero García por todo lo que me ha enseñado y por ser tan abierto a escucharme. Agradezco enormemente a Arsenii Titov por la valiosa oportunidad que tuve de trabajar y aprender de él.
Estoy particularmente agradecido a Carlos Faubel, quién fue mi hermano de investigación en cada proyecto.

Agradezco a Joannis Papavassiliou por enseñarme tanto sobre QCD no perturbativo y ayudarme a escribir esta tesis. También agradezco a Isabel Oldengott, Aurora Melis y en especial a Gabriela Barenboim, por la dedicación en un proyecto lateral. Agradezco además a Gabriel González Sprinberg por su hospitalidad en mi visita a su grupo de investigación en Uruguay.

Estaré siempre agradecido a todos mis colegas, y al mismo tiempo amigos, que llenaron mi doctorado de alegrías y buenos recuerdos. A mis amigos en los placenteros descansos de las comidas: Manuel Martínez, Michele Ronco, Pablo Arnault, Fei Gao, Isabel Oldengott, Pablo Martínez, Sergi Nadal, Andreu Masó, Pau Beltrán, Andreu Anglés, Carlos Miró y Daniel Queiroz. A los amigos de breve estancia en Valencia: Richard Dudley, Marco De Vito y Dimitrios Kranas. Agradezco en especial al grupo Garbancito: Silvia Pla y Aurora Melis. Agradezco al querido grupo de los burjassotenses: Flavio Bombacigno y Fabio Moretti. Agradecimiento a mis muy preciados compañeros de despacho: Matteo Rinaldi, Roberto Bruschini y Alberto Aparici.

Agradezco a mi familia por el amor y apoyo que me han dado en otro proyecto más en mi vida. Mis padres Ramón Coito e Inés Pereyra, mis tias Felisbina Rodríguez y Catalina Sánchez, mi hermano Nicolás Coito y mis sobrinos Santiago y Emily Coito.

Finalmente quiero expresar mi gratitud con el departamento de Física Teórica de la Universidad de Valencia por haberme incorporado tan amistosamente. Estoy muy agradecido con la Comunidad Valenciana por la oportunidad que he recibido en el programa Santiago Grisolía.

Abbreviations

The following abbreviations have been used throughout the text:

BBN	Big Bang Nucleosynthesis
BHL	Bardeen, Hill and Lindner
BSM	beyond the Standard Model
CC	compositeness condition
CHT	composite Higgs theory
CL	confidence level
CMB	cosmic microwave background
DD	direct detection
DM	dark matter
dSphs	dwarf spheroidal satellite galaxies
EFT	effective field theory
EWSB	electroweak symmetry breaking
EW	electroweak
GHP	gauge hierarchy problem
ID	indirect detection
ISS	inverse seesaw model
HK	Hill and Krog
LHC	Large Hadron Collider
NOS	neutrino oscillation

QCD	Quantum Chromodynamics
QLA	quark loop approximation
RGE	renormalization group equations
SM	Standard Model
SNO	Sudbury Neutrino Observatory
SSB	spontaneous symmetry breaking
SSM	Standard Solar Model
TC	technicolor
THEQ	thermal equilibrium
VEV	vacuum expectation value
WIMP	Weakly Interacting Massive Particles

Resumen y conclusiones en castellano

Parte I: Emergencia de masas en el Modelo Estándar

El bosón de Higgs es un campo escalar del Modelo Estándar (SM, por sus siglas en inglés) de partículas elementales que cumple dos funciones muy importantes. Por un lado permite construir una teoría renormalizable. El potencial escalar contiene un término de masa y un término cuadrático en el campo de Higgs, los cuales son ajustados en base a mediciones experimentales y haciéndolos compatible con la aparición de una ruptura espontánea de la simetría $SU(2)_L \times U(1)_Y$ del SM.

Y por otra parte ayuda a explicar la masa de todos los fermiones en el esquema de la teoría cuántica de campos, al poseer interacciones de tipo Yukawa que son ajustadas para acomodar las masas medidas en la actualidad. Esta última característica, que respeta las simetrías correspondientes al SM, es conocida como *mecanismo de Higgs* y fue propuesta en el año 1964 por R. Brout, F. Englert y P. Higgs.

Sin embargo, existen algunos aspectos que continuan sin explicación como la razón de los valores de los parametros ajustados, el origen de un escalar fundamental como el bosón de Higgs o la existencia de una ruptura espontánea de la simetría electrodébil. A partir de estas cuestiones han surgido, entre otras, teorías que asumen que el bosón de Higgs no es un campo fundamental sino un estado compuesto de fermiones, que poseen interacciones nuevas, y de gran magnitud, que son evidentes solamente a escalas de energías más altas. Este conjunto de teorías son conocidas como *modelos de Higgs compuestos*, y su principal característica radica en conectar la generación dinámica de masas con la aparición dinámica de la ruptura espontánea. De esta manera en esta tesis elegimos esta línea de investigación, y en particular, el subconjunto de modelos que asumen un estado compuesto formado por quarks top, con el objetivo de explicar las masas de este fermión y del bosón de Higgs de forma menos arbitraria, o como en física diríamos “más” natural. La razón de elegir solamente el quark top radica en que es el fermión con mayor interacción con el bosón de Higgs y por ende supondríamos, a priori, con mayor emparejamiento. Además los resultados no son fácilmente extendidos de manera análoga a los demás fermiones del SM.

Con respecto a las interacciones mencionadas entre fermiones, se podrían tomar en consideración todos los posibles operadores no renormalizables con los fermiones, de los cuales el de menor dimensión, y que debería ser más importante, implicaría la existencia de un operador con cuatro de éstos. La consideración de dicha interacción de cuatro fermiones, en una escala de energía muy alta, que podemos llamar Λ, tiene consecuencias sobre lo que constituye la teoría efectiva a bajas energías donde viven los estados compuestos, por ejemplo, el SM. En el esquema de bosonización, las consecuencias consisten en la aparición de un polo de Landau a la escala Λ sobre ciertos acoplamientos, que a su vez implicaría la predicción de los acoplamientos efectivos a partir del conocimiento de dicha escala. Estos últimos suponen en particular la predicción de las masas de las partículas.

En detalle, los acoplamientos efectivos son obtenidos tras hacerlos evolucionar a partir del polo de Landau hasta la escala electrodébil haciendo uso de las ecuaciones del grupo de renormalización adecuadas.

Resulta importante resaltar que debido a la naturaleza de las ecuaciones del grupo de renormalización de los acoplamientos, existen puntos de equilibrio que son *atractores* si la evolución es considerada desde energías altas hasta bajas. Esto constituye una característica deseable ya que haría que las predicciones finales no sean significativamente dependientes de los detalles de la teoría a la escala Λ.

Usando estos principios y metodología, se ha examinado el escenario más simple posible donde el bosón de Higgs es un estado compuesto formado solamente por la tercera generación de quarks. Los resultados en las predicciones en este caso, como lo mencionaron W.A. Bardeen, C.T. Hill y M. Lindner en 1990, son en general demasiado grandes comparadas con los valores medidos experimentalmente. Esto implica que las interacciones y contenido de partículas del modelo estándard no son suficientes; por lo que más tarde se han desarrollado en la literatura un conjunto de nuevos modelos con el fin de alcanzar la coincidencia entre las predicciones y los valores medidos en las masas.

En esta línea consideramos en este trabajo dos nuevos conjuntos de interacciones y/o partículas, y además desarrollamos una nueva implementación de las condiciones de tener la interacción de cuatro fermiones, en ausencia de escalares a altas energías. La implementación consiste en exigir la continuidad de los acoplamientos del modelo efectivo, con escalares compuestos, y los correspondientes al modelo de interacciones de cuatro fermiones, con los acoplamientos generados a un loop fermiónico. Su objetivo radica en plantear condiciones iniciales de forma restrictiva. De todas maneras, la dependencia de las predicciones en la forma de realizar la unión entre los modelos debe ser muy sutil, motivado, por ejemplo, por la falta de conocimiento de la teoría completa más allá del SM.

De esta manera, hemos considerado en primer lugar un conjunto de interacciones de cuatro fermiones con sus componentes de color contraídas de modo más complejo, lo que resulta en escalares compuestos que poseen color. Esta elección es motivada por generar contribuciones que harían disminuir las predicciones a las masas del quark top y el bosón de Higgs. De este modo hemos elegido primero las contracciones que dieran lugar a los escalares de color triplete y sextete, siendo singletes de $SU(2)_L$, y hemos anali- zado las predicciones para las masas del bosón de Higgs y quark top para cada escalar separadamente. Los resultados obtenidos consisten en valores superiores a los esperados bajo la restricción, de origen experimental, de limitar a los escalares de color a poseer masas iguales o mayores a la escala del TeV. El análisis en la masa del bosón de Higgs posee algunas dificultades en el caso del sextete de color, que son atribuídas en cierta medida a una mayor complejidad en el potencial más general posible en el escalar.

Por otro lado, hemos considerado el caso del octete de color y doblete de $SU(2)_L$, que es particularmente motivado por su característica de no generar violación del sabor entre los quarks del SM. Afortunadamente los resultados obtenidos en este escenario para la masa del quark top son muy favorables, con masas incluso menores a las esperadas y en valores de la escala Λ alejados de la escala de Planck. Mientras que, sin embargo, debido a la complejidad extra en el potencial más general posible del escalar, el análisis en la masa del bosón de Higgs tendrá que ser desarrollado en el futuro.

Además nos enfocamos en otro aspecto del SM, el cual requiere ser mejorado, y es que los neutrinos son partículas masivas. Sucede que en el SM los tres sabores de neutrinos son conjeturados como partículas no masivas y donde no existen componentes derechas, lo que significa que los neutrinos no pueden adquirir una masa gracias al mecanismo de Higgs como los demás fermiones. Sin embargo la no masividad de los neutrinos estaría en contradición con el descubrimiento de oscilaciones del sabor en los neutrinos activos, explicado solo si las masas son diferentes de cero. De este modo se requerirían nuevas interacciones y/o partículas que puedan explicar las masas de los neutrinos ligeros. En particular existen dos escenarios llamados *seesaw tipo I* e *inverse seesaw* que son capaces de proporcionar masas correctamente a los neutrinos ligeros y que son utilizados en este trabajo. En el primero se necesita la adición de neutrinos derechos, mientras que en el segundo también son necesarios nuevos fermiones estériles. Ambos escenarios se fundamentan en permitir una mezcla de los neutrinos del SM con estos fermiones extra, de modo que existan autoestados de masa suficientemente pequeña para explicar las oscilaciones observadas.

Entonces, en segundo lugar, hemos considerado un modelo que acopla el escenario de inverse seesaw al marco de composición y que es capaz de realizar predicciones correctas a las masas del quark top, el bosón de Higgs y los neutrinos ligeros al mismo tiempo. De esta manera el mismo considera una generación, a modo de simplificación, de un neutrino derecho y un fermión estéril como campos fundamentales. También se plantean dos interacciones de cuatro fermiones, por un lado entre estos fermiones extra y por otro entre el neutrino derecho y las terceras generaciones de quarks y leptones. Es así que el modelo da pie a dos estados compuestos donde uno de estos está asociado a las simetrías electrodébiles del SM y el otro solamente a una simetría global, que puede ser identificada como el número leptónico. Ambos escalares adquieren un valor esperado distinto de cero en el vacío, por lo que se produce una mezcla entre ambos y entonces generan un autoestado de masa que sería identificado como el bosón de Higgs, que es medido en el Large Hadron Collider (LHC), y en cuyo caso estaría constituido a la vez por neutrinos y quarks de la tercera generación. Siendo uno de los parámetros libres del modelo asociado a la proporción de quarks, respecto a los demás fermiones, que compone al bosón de Higgs. La escala de energía en la cual el número leptónico es roto espontáneamente será similar a los valores de las masas del escalar asociado y del fermión estéril. Los resultados parecen indicar que existe una región en el espacio de parámetros en que los dos acoplamientos de mayor importancia, el Yukawa asociado al quark top y el término cuadrático en el bosón de Higgs, reciben contribuciones significativas en su evolución por parte de los nuevos acoplamientos del modelo. Tanto es así que las predicciones finales a las masas son lo suficientemente pequeñas, en términos relativos, para alcanzar los dos valores adecuados al mismo tiempo.

Parte II: Escenarios con candidatos a Materia Oscura

La *materia oscura* (DM, por sus siglas en inglés) es el concepto en el que nuevas partícula(s) son responsables de las discrepancias entre las predicciones de la teoría de la Relatividad General, propuesta por Einstein en 1915, y algunas observaciones a la escala galáctica, de cúmulos de galaxias y cosmológica. Por lo tanto, la DM representa otra vía fuera del SM de partículas elementales, así como las ya mencionadas antes. Una de las evidencias más importantes de desacuerdo se descubrió en la medición de la distribución de velocidades de las estrellas alrededor del centro en las galaxias espirales. La medición resultó ser muy diferente a la predicción, con velocidades de rotación muy altas en regiones demasiado alejadas de la influencia gravitatoria del núcleo galáctico. Lo que en el marco de materia oscura supondría una distribución de masas bastante diferente a la que resulta tras cuantificar la materia visible dentro de las galaxias espirales. En particular se podría decir que grandes abundancias de materia no visible yacen dispersas en un halo alrededor del núcleo galáctico.

Por otro lado también llegaron otras observaciones muy importantes, como la medición de temperaturas medias más altas de lo esperado en el gas que compone a galaxias elípticas, o como la aparición del efecto de lente gravitational en que la luz proveniente de objetos lejanos es curvada en una región donde no existe suficiente materia visible. Este último fenómeno es relacionado con la observación de filamentos entre galaxias dentro de cúmulos de galaxias, y con la colisión de dos cúmulos como en el llamado Bullet Cluster en inglés.

Además de las evidencias gravitacionales que justifican la proposición de materia oscura, también fueron diseñados experimentos que han puesto a prueba si existen interacciones más allá de las gravitatorias, con resultados nulos. Así es que las nuevas partículas que compondrían la DM necesitan satisfacer ciertas condiciones o requerimientos, derivados de la fenomenología observada hasta el día de hoy y con el objetivo de explicar las discrepancias mencionadas antes. Entonces, más allá de ser partículas masivas, necesitan no tener interacciones gauge correspondientes con las simetrías del SM (por lo que son caracterizadas como singletes), y evitar además todas las detecciones directas e indirectas realizadas hasta el momento, así como también no ser producidas en los aceleradores de partículas. Asimismo deberían ser estables respecto a la edad del Universo y tener una abundancia específica, conocida como *abundancia reliquia*, que es usualmente representada por el cociente entre la densidad de energía de DM y la densidad crítica asociada a un Universo plano.

La abundancia reliquia de DM puede ser generada por un conjunto de mecanismos, de los cuales los dos más comunes son llamados en inglés *freeze-out* y *freeze-in*, siendo el primero el considerado en esta tesis. El primero se basa en asumir que en cierto momento en el Universo temprano las partículas de DM estarían en equilibrio térmico con el baño térmico de partículas del SM, mientras que en el último mecanismo se requiere lo opuesto, es decir, que la DM nunca ha llegado a dicho equilibrio y además que su abundancia temprana fue insignificante.

Este equilibrio térmico entre dos especies de partículas se sustenta en que las interacciones entre las mismas son sumamente importantes, de modo que éstas pueden alcanzar el "contacto térmico" mientras la expansión del Universo lo permita. Como consecuencia las especies comparten la misma temperatura y sus densidades siguen aquellas asociadas al equilibrio, llamadas distribuciones de Bose-Einstein en el caso de partículas escalares o de Fermi-Dirac en el de fermiones.

De este modo, se modela la evolución de las densidades de partículas como siguiendo los valores asociados al equilibrio, hasta que las interacciones se hacen progresivamente más débiles con el tiempo y la expansión de Universo deja de permitir el equilibrio térmico. Cuando esto último sucede se dice que la densidad normalizada por la expansión del Universo se ha "congelado", y a partir de entonces la densidad depende de modo diferente con la temperatura. La clave para reproducir el valor correcto de la abundancia de DM al día de hoy reside en que el congelamiento debe suceder en el momento justo.

El modelo mencionado en la primera parte de la tesis, donde se realiza la implementación del escenario de inverse seesaw en el marco de composición, implicaba la existencia de una partícula llamada *bosón de pseudo-Goldstone*, vinculada a la ruptura espontánea de una simetría global, que en su caso es asociada al número leptónico. El bóson de pseudo-Goldstone puede ser identificado como un posible candidato a DM, ya que por su naturaleza las interacciones son dependientes fuertemente con la energía. Esto conlleva ventajas a la hora de evitar haber sido ya descubierto en detecciones directas o producciones en aceleradores de partículas. Sin embargo, en el modelo analizado esta partícula tendría interacciones de tipo Yukawa a un loop con los fermiones del SM que le permitirían decaer a ellos, si su masa lo permite, lo que la podría prohibir de ser DM debido a los límites establecidos sobre la vida media de un candidato a DM. Desafortunadamente, en el esquema de composición los acoplamientos son muy grandes, derivado del polo del Landau que satisfacen a la escala Λ, incluso cuando las energías son bajas por lo que el decaimiento se hace muy grande en este escenario, que entonces excluye al bosón de pseudo-Goldstone de ser un posible candidato a DM.

De este modo pasamos a enfocarnos, en una segunda parte de la tesis, en las interacciones de cuatro fermiones que puedan dar lugar a que uno de estos sea un candidato a materia oscura, aunque fuera del esquema de composición ya analizado. Dichas interacciones serían todas aquellas formadas por los mismos fermiones que antes, aunque en una generación solamente con motivos de simplificar la fenomenología: el neutrino derecho más un nuevo fermión estéril que haría de candidato a DM. La motivación de ligar a los neutrinos con materia oscura yace en el deseo de explicar dos de los grandes misterios que existen en la física actual.

Así es que el análisis considera los siguientes conjuntos de suposiciones. En primer lugar que el candidato a materia oscura es el nuevo fermión y que éste será de Majorana siendo cargado con una simetría discreta Z_2. Y en segundo lugar que la abundancia de DM es generada en el mecanismo conocido como freeze-out, el cual resulta natural en este modelo para el espacio de parámetros considerado. La simetría discreta tiene como objetivo brindar al candidato de estabilidad y así evitar los límites ya mencionados a la vida media. Por otro lado nos enfocamos en el espacio de parámetros, de masas y acoplamientos, en que la abundancia es predominantemente producida gracias a la aniquilación de partículas de DM a neutrinos derechos, lo que principalmente conlleva a estar en la región donde el neutrino derecho es la partícula más ligera del sector oscuro. De esta manera este análisis es desarrollado de forma que el vínculo entre el SM y el sector oscuro esté predominantemente enfocado en el acoplamiento de tipo Yukawa entre el bóson de Higgs, el doblete leptónico y el neutrino derecho. Dicho escenario es conocido en la literatura de materia oscura como *Neutrino Portal*.

Luego analizamos los modelos en que las interacciones de cuatro fermiones son generadas efectivamente tras integrar un campo más pesado. Así el sector oscuro de estos modelos se formaría por los dos fermiones extras al SM y la partícula más pesada. Estos modelos son dividos según si el mediador es un campo escalar real o complejo o un campo vectorial. A su vez los casos con un campo escalar son separados dependiendo si el diagrama de Feynman, correspondiente a la aniquilación de DM a neutrinos derechos, sucede en lo que se conoce como canal-t o canal-s. Se realizó un análisis de la fenomenología en el caso de un mediador masivo tanto real como complejo en canal-t, mientras que en el canal-s solamente en el caso real. Una de las conclusiones más destacadas es que el espacio de parámetros adecuado, para el nuevo fermión como candidato a materia oscura, es en el que los valores de las masas de éste y del escalar mediador no están demasiado alejados. Siendo específicos, los valores de masas se situaron entre los 100 GeV y los 800 GeV en el caso de canal-t, mientras que en canal-s entre los 2 GeV a 100 TeV gracias a la existencia de una resonancia entre el DM y el escalar.

Además uno de los escenarios del modelo con un escalar complejo en canal-t, posee la peculiaridad de generar a un loop las masas de los neutrinos derechos. Lo que resulta satisfactorio dado que podría explicar de forma natural la pequeñez relativa en las masas de los neutrinos ligeros.

Sobre estos modelos también se examinó la variación en los resultados de la abundancia reliquia de materia oscura proveniente de realizar aproximaciones a las ecuaciones diferenciales, llamadas *ecuaciones de Boltzmann*, que rigen la evolución de la densidad de DM. La diferencia con el caso no aproximado fue solo manifiesta en regiones específicas del espacio de parámetros, mientras que en el resto se encontró que las aproximaciones proveen de resultados confiables.

Volviendo a plantear al bosón de Goldstone como candidato a DM, también hemos explorado bajo qué condiciones este campo escalar podría ser efectivamente un candidato adecuado. Por ejemplo, haciendo que los acoplamientos Yukawa con los fermiones sean muy pequeños, se podrían evitar los límites en la vida media que posee la materia oscura. De este modo hemos examinado el límite en que no existen interacciones de tipo Yukawa, ni tampoco los fermiones extra al SM mencionados antes. Entonces en el modo más simple posible, en términos del número de partículas nuevas, analizamos candidatos a materia oscura en un modelo con dos campos reales desde donde emerge la existencia de un bosón de Goldstone masivo. Con el objetivo de estabilizar al mismo se asume que existe una simetría discreta Z_2 capaz de hacerlo, proporcionando así un candidato a materia oscura, que identificaremos como el segundo escalar.

El modelo considera que los dos campos escalares reales nuevos al SM estarían cargados con una simetría $O(2)$ global que debe ser espontánea y explícitamente rota. En el caso en que la ruptura es solamente explícita, el espacio de parámetros adecuado para tener un candidato a DM es más o tan limitado como el modelo escalar más simple posible con DM (únicamente un campo real como sector oscuro). Este último se limita a que el valor de la masa de la materia oscura es aproximadamente la mitad del valor de la masa del bosón de Higgs o bien debe ser mayor o igual al TeV.

De este modo, más allá de los términos que componen el potencial sujeto a la simetría $O(2)$, se consideraron todos los posibles términos de ruptura que formarían el potencial más general posible con dos campos reales extra. Sin embargo se eligieron cuatro modelos, que llamamos *modelos mínimos*, para analizar en detalle la fenomenología, tratando de identificar las regiones que generan las condiciones favorables para tener una partícula de materia oscura, y a la vez determinar si la región de masas adecuadas posibles se extiende respecto al caso mencionado con un solo escalar real.

Los cuatro modelos se caracterizan por poseer un solo grado de libertad asociado a la ruptura de la simetría $O(2)$, llamándolos modelos lineal, cuadrático, cúbico o cuártico en función del valor del exponente total en los campos que componen el sector oscuro. De este modo también examinamos si los modelos podrían llegar a estar asociados a regiones adecuadas para contener un candidato a DM diferentes, y así poder distinguirlos si en un futuro una partícula de materia oscura es finalmente hallada. En particular, los últimos dos modelos mínimos poseerían la característica de implicar nuevas interacciones entre los escalares reales y autointeracciones de materia oscura.

El análisis mostró que en vastas regiones del espacio de parámetros las aniquilaciones de la DM son excesivamente débiles y hacen que el freeze-out suceda demasiado pronto en el tiempo, o lo que es lo mismo a temperaturas demasiado altas, lo que conlleva a obtener abundancias de DM desmedidamente grandes de forma bastante usual. Sin embargo fueron observadas excepciones en ciertas regiones de parámetros que se diferencian según la relación existente entre la masa de la materia oscura y de los demás escalares en el modelo: el bosón de Higgs y el primer escalar. Estas suceden cuando la DM se encuentra en las regiones de resonancias o cuando es ligeramente más liviano o simplemente más pesado respecto a los escalares mencionados anteriormente. Por otro lado también se encontró como región adecuada al caso en que la materia oscura posee una masa cercana o mayor a 100 GeV y teniendo un ángulo de mezcla entre el bosón de Higgs y el primer escalar relativamente más grande que en los casos anteriores.

En cada uno de los modelos seleccionados existían cuatro grados de libertad que podían ser intercambiados a cuatro variables físicas: las masas de los dos escalares extra, el ángulo de mezcla y la escala de energía a la que sucede la ruptura espontánea de la simetría. Procedimos a estudiar las diferencias en los modelos a través de examinar en qué región en las variables físicas cada uno poseía un candidato a materia oscura. Es así que se encontró que en las resonancias y en la región de masas de materia oscura mayores a 100 GeV no es posible la distinción, mientras que sí lo es en los demás casos. Es decir si el bosón de Higgs y el primer escalar tienen masas ligeramente mayores o menores que el segundo escalar, entonces es posible diferenciar los modelos en las variables físicas con claridad.

También se examinó la posible existencia de candidatos a DM con masas en la región sub-GeV. Los resultados fueron afirmativos aunque con fuertes restricciones provenientes de mediciones en el decaimiento invisible del bosón de Higgs o en el ángulo de mezcla entre los escalares u originarias de detecciones indirectas de materia oscura, entre otras.

Contents

Chapter 1

Hints beyond the Standard Model

1.1 The Standard Model

The Standard Model (SM) [5–13] is the Quantum Field Theory of elementary particles which is set in a $SU(3)_c \times SU(2)_L \times U(1)_Y$ gauge theory. The particle content consists of a number fermions and scalar fields that are described in Tab. 1.1, in addition to the respective gauge bosons: G^a_μ, W^a_μ and B_μ. In order to set the notation we briefly describe the SM interactions here. The Lagrangian is written as,

$$\begin{aligned}\mathcal{L}_{SM} = &-\frac{1}{4}\left(G^a_{\mu\nu}\right)^2 - \frac{1}{4}\left(W^a_{\mu\nu}\right)^2 - \frac{1}{4}B^2_{\mu\nu} + \mathcal{L}_{scalar} + \mathcal{L}_{Yuk} \\ &+ i\overline{L}_i\left(\slashed{\partial} - ig_2\slashed{W}^a\tau_a - ig'Y_L\slashed{B}\right)L_i + i\overline{e}^i_R\left(\slashed{\partial} - ig'Y_e\slashed{B}\right)e^i_R \\ &+ i\overline{Q}_i\left(\slashed{\partial} - ig_3\slashed{G}^a\lambda_a - ig_2\slashed{W}^a\tau_a - ig'Y_Q\slashed{B}\right)Q_i \\ &+ i\overline{u}^i_R\left(\slashed{\partial} - ig_3\slashed{G}^a\lambda_a - ig'Y_u\slashed{B}\right)u^i_R + i\overline{d}^i_R\left(\slashed{\partial} - ig_3\slashed{G}^a\lambda_a - ig'Y_d\slashed{B}\right)d^i_R\,, \end{aligned} \tag{1.1}$$

with

$$\begin{aligned} G^a_{\mu\nu} &= \partial_\mu G^a_\nu - \partial_\nu G^a_\mu + g_3 f^{abc} G^b_\mu G^c_\nu\,, \\ W^a_{\mu\nu} &= \partial_\mu W^a_\nu - \partial_\nu W^a_\mu + g_2 \epsilon^{abc} W^b_\mu W^c_\nu\,, \\ B_{\mu\nu} &= \partial_\mu B_\nu - \partial_\nu B_\mu\,, \end{aligned} \tag{1.2}$$

where f^{abc} (λ_a) and ϵ^{abc} (τ_a) are the structure constants (group generators) of the $SU(3)_c$ and $SU(2)_L$ group algebras respectively, while g_3, g_2 and g' are the $SU(3)_c$, $SU(2)_L$ and $U(1)_Y$ couplings, respectively. The subscripts μ and ν correspond to Lorenz indices.

The Yukawa-type interactions are described in $\mathcal{L}_{Yuk}$:

$$-\mathcal{L}_{Yuk} = y^d_{ij}\overline{Q}^i_L H d^j_R + y^u_{ij}\overline{Q}^i_L \tilde{H} u^j_R + y^e_{ij}\overline{L}^i_L H e^j_R + \text{H.c.} \tag{1.3}$$

with $u^i_R = (u_R, c_R, t_R)$ and so on. $\tilde{H} = i\tau_2 H^*$ and τ_2 is the corresponding Pauli matrix. The scalar sector $\mathcal{L}_{scalar}$ is given as

$$\mathcal{L}_{scalar} = +|D_\mu H|^2 - m^2_H|H|^2 - \lambda_H|H|^4\,, \tag{1.4}$$

with m_H and λ_H being identified as the mass and self-interaction terms in the Higgs boson potential. The covariant derivative is expressed as,

$$D_\mu H = \partial_\mu H - ig_2 W^a_\mu \tau_a H - \frac{1}{2} i g' B_\mu H\,. \tag{1.5}$$

The $SU(2)_L \times U(1)_Y$ symmetry is broken spontaneously to $U(1)_{EM}$ by the vacuum expectation value (VEV) acquired by the Higgs doublet, $\langle H^0\rangle^2 = v^2_h/2$, mechanism called electroweak symmetry breaking (EWSB). The calculations are usually performed in the unitary gauge, which will be the one considered along this work, and where the Higgs doublet is parameterised as

$$H = \frac{1}{\sqrt{2}}\begin{pmatrix} 0 \\ v_h + h \end{pmatrix}, \tag{1.6}$$

and the EWSB leads to three massive gauge bosons: $W^\pm_\mu = (W^1_\mu \mp i W^2_\mu)/\sqrt{2}$ and $Z_\mu = \cos\theta_w W^3_\mu - \sin\theta_w B_\mu$, with $\tan\theta_w = g'/g_2$. The physical Higgs boson is identified as h and its mass is $m^2_h = v^2_h \lambda_H$.

The Higgs boson is the necessary scalar field of the SM that helps the theory in two meaningful ways. On one side, it allows to construct a renormalizable field theory by, for example, solving the violation of unitarity at tree level of the $W^\pm$ and Z bosons. And on the other side, it leads to the generation of masses for all the massive particles known in Nature, through EWSB, in the process called *Higgs mechanism*, see Refs. [6, 7, 14].

In this manner, the Higgs sector in the SM contains the mass and quartic self-interaction terms which are adjusted to obtain a nonzero VEV for the neutral CP-even component of the Higgs field, that leads to nonzero $W^\pm$ and Z masses,

$$m_W = v_h\, g_2/2\,, \qquad m_Z = v_h\sqrt{g^2_2 + g'^2}/2\,. \tag{1.7}$$

Furthermore, when Higgs-fermion-antifermion Yukawa terms y^a_{ij}, as in Eq. (1.3), are included in the model, with adjusted couplings strengths, the nonzero VEV leads

Fields	$Q_L = \begin{pmatrix} u_L \\ d_L \end{pmatrix}$	u_R	d_R	$L_L = \begin{pmatrix} \nu_L \\ e_L \end{pmatrix}$	e_R	H
$U(1)_Y$	$+1/6$	$+2/3$	$-1/3$	$-1/2$	-1	$+1/2$
$SU(2)_L$	2	–	–	2	–	2
$SU(3)_c$	3	3	3	–	–	–

Table 1.1: Hypercharges and representations of the SM fields. Q_L and L_L are the SM quark and lepton $SU(2)_L$ doublets; u_R, d_R and e_R are the SM fermion singlets. H is the Higgs doublet. The three generations of fermions have these same quantum numbers, differing on the Yukawa couplings and masses. With regard to $SU(2)_L$ and $SU(3)_c$, 2 and 3 indicates that the field transforms in the fundamental representation respectively, while the symbol $-$ denotes that the field is a singlet.

to masses for the fermions as $m^a_{ij} = y^a_{ij} v_h / \sqrt{2}$.

1.2 The gauge hierarchy problem

We described before the essential role played by the Higgs boson in the SM; however, there are some aspects that remain unexplained, such as the values of the constants and the deeper origin of the Higgs boson, as well as the source of the spontaneous symmetry breaking (SSB). Clearly the SM must give way to a complete theory at some high-energy scale, as it is evident from its difficulty as a quantum field theory in keeping the scalar particle much lighter than the scale Λ_{max}, associated to the maximum energy scale up to which the theory remains valid.

For example consider the 1-loop contributions to the Higgs boson mass, which by dimensional analysis are quadratically divergent. Using a regularization with a momentum cut-off k, the parameters (couplings y and λ_H, and mass parameters m_H) will generally depend on k, and in this way the cut-off theory is only useful for momenta and energies smaller than k. The 1-loop diagrams are cut-off dependent and proportional to k^2, then the mass has the following dependence with two different values k' and k ($k' < k$),

$$m_H^2(k') = m_H^2(k) + k^2 \left(C_1 \lambda_H + C_2 y^2 + \dots \right) . \tag{1.8}$$

Consider that the values $y(k), \dots, m_H(k)$ are most closely related to a fundamental underlying unified theory when k is as large as possible, say of order Λ_{max}; consequently, there are no extra fields beyond the SM at least until the scale Λ_{max}.

After assuming k' as zero ($k' \approx m_Z \ll \Lambda_{max}$):

$$m_H^2(0) = m_H^2(\Lambda_{max}) + \Lambda_{max}^2 \left(C_1 \lambda_H(\Lambda_{max}) + \dots\right) . \tag{1.9}$$

We know that $m_H^2(0)$ at the EW scale is order $\mathcal{O}(10^2\,\text{GeV})$, then taking the high-energy scale as $\Lambda_{max} \sim 10^{15}\,\text{GeV}$ leads to:

$$m_H^2(0)/\Lambda_{max}^2 \sim 10^{-26} = m_H^2(\Lambda_{max})/\Lambda_{max}^2 + \left(C_1 \lambda_H(\Lambda_{max}) + \dots\right) . \tag{1.10}$$

This is an unreasonable result which requires the cancellation between the dimensionless parameter $m_H^2(\Lambda_{max})/\Lambda_{max}^2$ and the series $(C_1 \lambda_H(\Lambda_{max}) + \dots)$ to the 26 decimal places to allow for the light scale physics to be as we know. In this manner, the existence of two widely separated scales, namely the EW scale and the unification or Planck scale, is "unnatural" and called *gauge hierarchy problem* (GHP) [15].

With the belief that a complete description of particle interactions in a final theory entails the absence of quadratic divergences, the following discussion could serve as the basis for the solution of the GHP. The idea is that if a particle mass is much smaller than Λ_{max}, there should exist a symmetry, possibly approximate, under which the mass term is forbidden. We know three examples of this as Ref. [16] mentioned. For a spin-one particle like the photon, the gauge symmetry $A_\mu \to A_\mu + \partial_\mu \lambda$ forbids the occurrence of the photon mass term $m^2 A_\mu A^\mu$. Likewise, for fermionic particles there is a symmetry which protect their masses: chiral symmetry, under which the left-handed and right-handed fermionic components transform differently $\psi_L \to e^{i\alpha}\psi_L, \psi_R \to e^{i\beta}\psi_R$, $\alpha \neq \beta$, forbidding the mass term $m\psi_L\psi_R$ + H.c. Also scalar particles can be naturally light if they are Goldstone bosons of some broken global symmetry since their transformation $\phi \to \phi + a$ forbids the mass term $m^2\phi^2$. However in the case of the Higgs boson, required in the SM by the EW symmetry breaking mechanism, the procedure is very complex and in the absence of any symmetry principle we should expect $m_H^2 \sim \Lambda_{max}^2$.

This discussion leads to theories beyond the SM to solve the GHP.

1) The *Little Higgs models* attempt to reconcile the idea of dynamical EW symmetry breaking with the existence of a light Higgs particle by considering it as an approximate Goldstone boson. So there are some new strong interactions, at some higher scale, that possess an approximate global symmetry which is spontaneously broken. The SM gauge interactions necessarily break these symmetries and give rise to a potential. However accounting for the fermion masses and light Higgs boson remained to be a challenge in these scenarios.

2) In *large extra dimension models* one supposes that there are d compact extra dimensions of space (at least two), with volume l^d. The objects known as 3-branes fill

all of space and their excitations behave like particles in four dimensions, including the Higgs boson. However these models make exciting predictions as the existence of many new particles, associated with the modes of the higher dimensional fields on the compact volume (Kaluza-Klein modes) that can be produced in large numbers and have not been observed. In these models in some sense the GHP is replaced by the unexplained large size of these extra dimensions, see e.g. Ref. [17].

3) *Technicolor* (TC) offers a different solution to the GHP, based on the idea of removing all fundamental scalar particles from the theory. The mass scale which sets the EWSB is dynamically determined in a strongly interacting gauge theory with only fermionic particles (QCD-like). In this way, in the same notation as above, the corresponding gauge coupling constant depends on the cut-off as

$$\frac{dg(k)}{d\log k} = \beta(g(k)) = -\beta_0 g(k)^3 + \dots \,. \tag{1.11}$$

Then if g is chosen to be small at $k \sim \Lambda_{max}$, at a much smaller momentum scale, called λ_{TC}, it will become large,

$$\lambda_{TC} \sim \Lambda_{max} \exp\left(-\frac{1}{2\beta_0 g^2(\Lambda_{max})}\right) \tag{1.12}$$

Then this scale is associated to the appearance of composite scalar fields, as occurs in QCD with the pions.

4) *Composite Higgs theories* (CHTs) consider, as TC theories, an extension of the SM that treats it as an effective field theory (EFT) comprising a composite, non-fundamental, Higgs boson. In these scenarios the composites are achieved by strong four-fermion interactions. This is the framework we focus in this thesis and a detailed description can be found in Sec. 1.3.

5) *Supersymmetry* transforms bosons into fermions and fermions into bosons, so the symmetry insures the equality of fermion and boson masses even after quantum radiative corrections. If there is a chiral symmetry protecting the fermions from being massive then, because of supersymmetry, the boson mass will also be zero. And this is how supersymmetry protects the Higgs potential from its sensitivity to a next energy scale Λ_{max}.

1.3 Composite Higgs boson

According to the composite Higgs theories there is no fundamental scalar field, and the SM would be an effective description of low-energy physics. In particular we will study a specific subset of these theories where the Higgs boson is a composite state containing the quark top, what is known as $\bar{t}t$ condensation, see Ref. [18]. The idea is motivated by the fact that the top quark is the heaviest and therefore the most interacting fermion with the Higgs boson.

The appeal of this effective dynamical framework lies in the fact that it can connect the dynamical generation of the heavy top quark mass, and more fermions at the expense of free parameters, and the dynamical EWSB, as the quark condensates in QCD: $\langle \bar{u}u \rangle$.

In this manner the framework has the pleasant feature of addressing a reduction in the number of free parameters of the theory, compared to the SM scenario. The complexity of the SM in the fermionic and gauge structures makes it looks like an improbable fundamental theory. It contains many free parameters that correspond to important physical quantities: the three gauge coupling constants, the twelve fermion masses and the four Cabibbo-Kobayashi-Maskawa mixing parameters. These cannot be computed in the context of the model, and simplifying the SM structure and predicting its free parameters is important, so we focus here in relating the top and Higgs boson masses.

$\bar{t}t$ condensation

In this section, we are going to outline the $\bar{t}t$ condensation approach to create a composite Higgs scalar field. In doing so, we go over the assumptions on the content, particles and/or interactions, that the new physics should posses, as well as the matching conditions for being the SM an EFT at the EW scale.

The line of reasoning was clearly stated in Ref. [19] as:

> *If we assume that there is new physics beyond the standard model which becomes visible above the scale Λ, and that the degrees of freedom of the effective theory below the scale Λ are just the fermions and gauge bosons of the standard model, then we can parametrize the new physics by nonrenormalizable interactions among the fermions and gauge bosons. All of the possible nonrenormalizable interactions may be important for describing the physics at energy scales near the cutoff, but at low energies, the most important interactions are those involving operators with the lowest mass dimension. Four-fermion operators are the lowest mass dimension operators we can add to the standard model.* (M.A. Luty)

In this manner, at some high energy scale Λ, below the Planck scale, there is no fundamental scalar field but a strong enough four-fermion interaction able to induce quark-antiquark condensation. Inspired by the Nambu-Jona-Lasinio model [20, 21], Bardeen, Hill and Lindner (BHL) [18] proposed a four-quark interaction of the top quark at a high-energy scale $\mu \sim \Lambda$:[1]

$$\mathcal{L} = G\left(\overline{Q}_L t_R\right)\left(\bar{t}_R Q_L\right)\,. \tag{1.13}$$

We can introduce an auxiliary field H, a priori not related with the Higgs doublet, such that the previous interaction can be written as,

$$\mathcal{L} = -m_{0H}^2|H|^2 + \left(y_{0t}\,\overline{Q}_L t_R H + \text{H.c.}\right)\,, \tag{1.14}$$

where the couplings satisfy $G = y_{0t}^2/m_{0H}^2$.[2] Note that this field H is a complex $SU(2)_L$ doublet with $U(1)_Y$ charge $-1/2$. The renormalization will give us an EFT with extra kinetic and quartic terms:

$$\mathcal{L} = Z_H(\partial_\mu H)^\dagger(\partial^\mu H) + \left(y_{0t}\overline{Q}_L t_R H + \text{H.c.}\right) - \tilde{m}_H^2|H|^2 - \tilde{\lambda}_H|H|^4\,. \tag{1.15}$$

In the *quark loop approximation* (QLA), 1-loop order contributions from only quarks make up the EFT at low energies. In this way, loop diagrams from other particles are ignored, even the radiative corrections coming from the composite scalar itself. Then, at an energy scale μ below Λ, the 1-loop diagrams depicted in Fig. 1.1 lead to,

$$\begin{aligned} Z_H =& y_{0t}^2 L, \quad \tilde{\lambda}_H = 2y_{0t}^4 L, \quad L = \frac{N_c}{16\pi^2}\log\frac{\Lambda^2}{\mu^2}, \\ \tilde{m}_H^2 &= m_{0H}^2 - 2y_{0t}^2\frac{N_c}{16\pi^2}\left(\Lambda^2-\mu^2\right)\,, \end{aligned} \tag{1.16}$$

where N_c is the number of colors. This approximation is equivalent to a truncation of an expansion in N_c to order $1/N_c$. Notice that the QCD contributions are ignored.

Observe that if the mass $\tilde{m}_H$ has a small value compared to Λ, then $m_{0H} \sim \Lambda$. The potential for the Higgs field can have a broken phase if $\tilde{m}_H^2 < 0$, what is equivalent to $\Lambda^2(1 - y_{0t}^2 N_c/8\pi^2) < 0$, for $\mu \ll \Lambda$, and hence $y_{0t}^2 > 8\pi^2/N_c$.

Rescaling the field H to $H/\sqrt{Z_H}$, so to normalize in the usual way, we obtain

---

[1] Compared to the Nambu-Jona-Lasinio original proposal, here we are only considering four-fermion interactions made out of the top quark.

[2] The explanation of the origin of the four-fermion interaction, in terms of an UV model, is given in several models, see e.g. the review in Ref. [22]. This work does not provide an explanation for the new interaction, but deals with it as an EFT in which the SM is embedded. In this manner, we focused on the effective model at low energies and on methods of computing the dynamical generation of fermionic masses and dynamical EWSB.

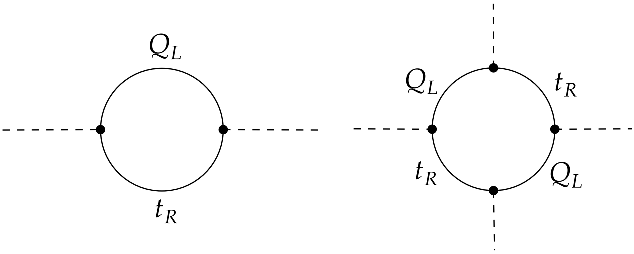

Figure 1.1: Diagrams contributing to the induced terms of composite scalars in the quark loop approximation. The full lines represent the top quark propagator and dashed lines the composite scalar field. Extracted from Ref. [22].

the SM Lagrangian:

$$\mathcal{L} = (\partial_\mu H)^\dagger (\partial^\mu H) + \left(y_t \overline{Q}_L t_R H + \text{H.c.}\right) + m_H^2 \left|H\right|^2 - \lambda_H \left|H\right|^4 \ , \tag{1.17}$$

with

$$m_H^2 = \frac{\tilde{m}_H^2}{Z_H}, \quad y_t^2 = \frac{y_{0t}^2}{Z_H} = \frac{1}{L}, \quad \lambda_H = \frac{\tilde{\lambda}_H}{Z_H^2} = \frac{2}{L} \, . \tag{1.18}$$

Notice that the couplings y_t and λ_H diverge when $\mu \equiv \Lambda$ and are proportional to each other, $\lambda_H = 2y_t^2$, which establishes the relation between the Higgs boson and top quark masses, m_h and m_t respectively, in the QLA. If the field H acquires a VEV, $v_h \neq 0$, we can parametrise H as in Eq. (1.6), in the unitary gauge, and have the following relations,

$$m_t = y_t \frac{v_h}{\sqrt{2}}, \quad m_h^2 = v_h^2 \lambda_H \, . \tag{1.19}$$

From Eqs. (1.16) and (1.19) we obtain a prediction for m_t, for a given scale Λ, at $\mu = m_t$:

$$y_t^2 = \frac{1}{L} \quad \to \quad m_t^2 = \frac{8\pi^2 v_h^2}{N_c \log\left(\Lambda^2/m_t^2\right)} \, . \tag{1.20}$$

The solution is written in terms of the Lambert function $W_{-1}(x)$:

$$m_t = \Lambda \exp\left[\frac{1}{2} W_{\text{-}1}\left(\frac{-8\pi^2 v_h^2}{N_c \Lambda^2}\right)\right] \, . \tag{1.21}$$

An important feature in this prediction of m_t is its unique dependence on one parameter: Λ. In particular, the measured top quark mass is obtained at $\Lambda \sim 10^{13}$ GeV. Unfortunately, this approximation does not take into account important radiative corrections as can be noticed in the following way. Let us consider the dependence in the scale μ of the couplings, Eq. (1.17),

$$y_t^2 = -\frac{1}{2N_c t}, \quad \lambda_H = 2y_t^2\,, \tag{1.22}$$

with $t = \ln(\mu/\Lambda)/(16\pi^2)$, and then

$$\frac{dy_t^2}{dt} = \frac{1}{2N_c t^2} = 2N_c y_t^4, \quad \frac{d\lambda_H}{dt} = 4N_c y_t^4\,. \tag{1.23}$$

In the SM's renormalization group equations (RGEs) at 1-loop level are:[3]

$$\begin{aligned} \frac{dy_t^2}{dt} &= (3+2N_c)y_t^4, \\ \frac{d\lambda_H}{dt} &= 12\lambda_H^2 + 4N_c\lambda_H y_t^2 - 4N_c y_t^4\,. \end{aligned} \tag{1.24}$$

Comparing Eqs. (1.23) and (1.24), one sees that the first one neglects the Higgs boson contributions at 1-loop level: Higgs wave function renormalization ($\propto \lambda_H y_t^2$) and pure Higgs loop ($\propto \lambda_H^2$). Furthermore, it also neglects the wave function renormalization of the top quark ($\propto y_t^4$). Due to this, Eq. (1.23) reproduces the SM's RGE in the limit of large N_c, in accordance with QLA.

The difference between Eq. (1.23) and Eq. (1.24) motivates the substitution $2N_c \to (3+2N_c)$ which leads to:

$$-\frac{1}{y_t^2(\mu)} + \frac{1}{y_t^2(\Lambda)} = (3+2N_c)t \quad \to \quad y_t^2(\mu) = -\frac{1}{(3+2N_c)t}\,, \tag{1.25}$$

where we assumed $y_t^2(\Lambda) \gg 0$. Once again the resulting value of the top quark mass only depends on the scale Λ:

$$m_t = \Lambda \exp\left[\frac{1}{2}W_{\text{-}1}\left(\frac{-16\pi^2 v_h^2}{(3+2N_c)\Lambda^2}\right)\right]\,. \tag{1.26}$$

Finally, Fig. 1.2 shows that the QLA-improvement of Eq. (1.26) depicted in blue gives better predictions for m_t than the ones obtained using Eq. (1.21), and depicted in red. Moreover, we also plot in orange the full 1-loop SM computation for m_t as a function of the scale Λ, which will be explained below. In this case, the inclusion of QCD corrections worsen the results.

---

[3] For the moment we neglect gauge interactions.

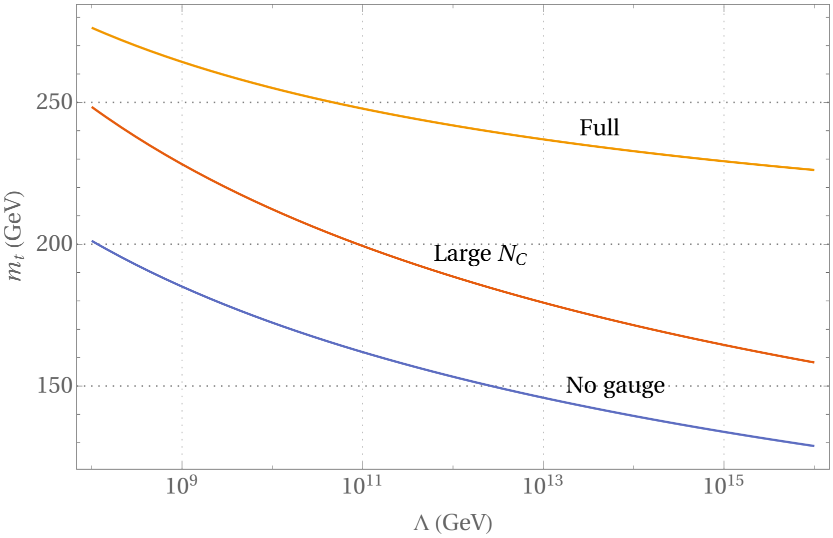

Figure 1.2: Predictions for the mass of the quark top m_t as a function of the energy scale Λ in different approaches: QLA as in Eq. (1.21) (red line), QLA-improvement as in Eq. (1.26) (blue line) and full 1-loop SM computation [RGE approach] (orange line).

Compositeness condition in the RGEs

Let us consider the assumptions of the CHT: at some high energy scale Λ there are strong four-fermion interactions and no fundamental scalar fields. Consequently at Λ the Lagrangian is given in Eq. (1.14), which matches Eq. (1.15) in the limit in which Z_H and $\tilde{\lambda}_H$ go to zero. Therefore the EFT could be described by the Lagrangian in Eq. (1.15) with the matching conditions set on $Z_H, \tilde{\lambda}_H \to 0$ in the limit $\mu \to \Lambda$, while y_{0t} and $\tilde{m}_{0H}^2$ stay finite. We will dub these as *compositeness condition* (CC), which translates into, after normalizing as H to $H/\sqrt{Z_H}$, at $\mu \to \Lambda$,

$$y_t^2\,(\mu) \to \infty, \quad \lambda_H(\mu) \to \infty\,, \tag{1.27}$$

as it is suggested from Eq. (1.18). Then we can use the SM RGEs to find solutions that satisfy the above boundary conditions at the scale Λ, and provide predictions for m_t and m_H at the EW scale. The RGEs are:[4]

---

[4] Using the $SU(5)$ convention $3g_1^2 = 5g'^2$.

$$
\begin{aligned}
(16\pi^2)\beta_{y_t} =& \left(N_c + \frac{3}{2}\right) y_t^3 - 3\frac{\left(N_c^2-1\right)}{N_c} g_3^2 y_t - \frac{9}{4} g_2^2 y_t - \frac{17}{12} g_1^2 y_t \, , \\
(16\pi^2)\beta_{\lambda_H} =& - 4N_c\, y_t^4 + 4N_c \lambda_H y_t^2 + 12\lambda_H^2 - \left(9g_2^2 + 3g_1^2\right) \lambda_H \\
& + \frac{9}{4} g_2^4 + \frac{3}{2} g_2^2\, g_1^2 + \frac{3}{4} g_1^4 \, , \\
(16\pi^2)\beta_{g_i} =& - C_i g_i^3 \, ,
\end{aligned}
\tag{1.28}
$$

with $\beta_\epsilon = d\epsilon/d\ln(\mu)$ and

$$
C_1 = -\frac{1}{6} - \frac{10}{9} n_q \, , \qquad C_2 = \frac{43}{6} - \frac{2}{3} n_q \, , \qquad C_3 = \frac{1}{3}\left(11N_c - 2n_q\right) \, . \tag{1.29}
$$

The parameter n_q corresponds to the number of effective quark flavors, where for energies above the quark top mass is $n_q = 6$. Notice that in this RGE approach we are taking into account all the radiative corrections to the theory, compared to Eq. (1.24). The orange line in Fig. 1.2 is obtained in this way.

1.4 Neutrino physics

We will incorporate light neutrino masses in the BHL mechanism in Ch. 4 and consider neutrinos as portals between the visible and dark sectors in Ch. 5, therefore in this section we review the relevant aspects of neutrino physics.

1.4.1 Neutrino oscillations

In the SM, neutrinos are massless, colorless and electrically neutral fermionic particles that only interact with the weak force, making them very difficult to detect. Measurements show there are three flavors of neutrinos, one for each charge lepton, the corresponding to the electron (ν_e) [23, 24], muon (ν_μ) [25], and tau (ν_τ) [26].

There were experiments searching for an upper limit on the number of neutrino flavors. They were done by analyzing the Z resonance measured by the Large Electron-Positron collider (LEP) experiments. There was better agreement for the Z line-shape prediction with the number of neutrinos being three, see Fig. 1.3. There were also other experiments on the Z decay that showed similar results.[5]

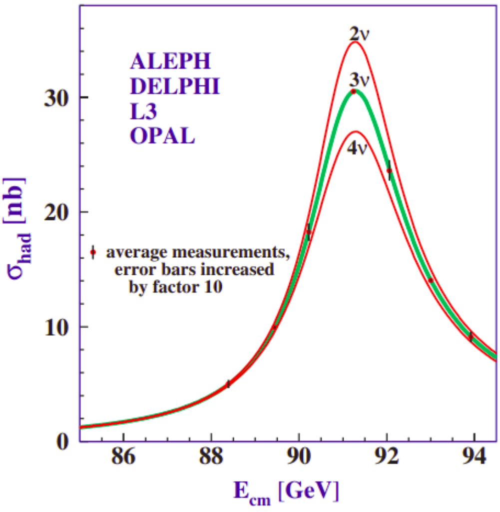

Figure 1.3: Hadronic production cross section measurements around the Z resonance by the LEP experiments. The curves are the predicted cross sections for the different number of neutrinos with SM couplings and negligible mass as a function of the center-of-mass energy E_{cm}. Details are present in Ref. [28].

---

[5] See for instance Ref. [27].

Beyond the SM, one of the first hints for massive neutrinos happened when Raymond Davis Jr. and his colleagues [29, 30] observed a significant deficit in the solar electron neutrino flux, compared to the predictions given by J. Bahcall, N. Bahcall, and G. Shaviv [31] in a model known as Standard Solar Model (SSM). This deficit was known as the *solar neutrino problem.* After that, the Sudbury Neutrino Observatory (SNO) experiment measured also the neutral solar neutrino-induced interactions, being sensitive to other neutrino flavors, finding that the net sum of all flavors agreed with the flux predicted by the SSM.

Furthermore, Kamiokande-II found interesting results from atmospheric neutrinos [32] measuring the ratio of fluxes

$$\frac{\phi_{\nu_\mu} + \phi_{\bar{\nu}_\mu}}{\phi_{\nu_e} + \phi_{\bar{\nu}_e}} \approx 1\,, \tag{1.30}$$

when it was supposed to be near 2.[6]

The measurements from SNO and Kamiokande-II can be explained by neutrino oscillating in flavor space, phenomena called or known as *neutrino oscillations* (NOSs) [33, 34]. Later, other measurements supported the NOS's theory, as the improvement in the SuperKamiokande experiment in 1998, which achieved to observe a zenith angle dependence for the ν_μ atmospheric neutrino flux and suggested the vanishing of ν_μ when they cross the Earth [35, 36].

In this way, it was found a new hierarchy of masses associated with the neutrino masses being so small, $\approx 10^{-2}\,$eV, compared to the rest of the fermions in the SM.

Formalism of neutrino oscillations

The NOSs are described in a model of neutrinos where the flavors mix by a unitary matrix U as

$$|\nu_\alpha\rangle = \sum_i U^*_{\alpha i}\,|\nu_i\rangle\ , \tag{1.31}$$

where ν_α and ν_i correspond to the neutrinos in flavor and mass eigenstate, respectively; therefore, neutrinos are produced as flavor eigenstates and then propagate as

---

[6] Atmospheric neutrinos are the resulting neutrinos coming from the cosmic rays interacting with the atmosphere. First pions are produced, which decay to neutrinos and muons. And then the muons decay to electrons and neutrinos:

$$\pi^+ \to \mu^+ + \nu_\mu \to e^+ + \nu_e + \bar{\nu_\mu} + \nu_\mu$$
$$\pi^- \to \mu^- + \bar{\nu_\mu} \to e^- + \bar{\nu_e} + \nu_\mu + \bar{\nu_\mu}$$

mass eigenstates. This means that there is a non-zero probability that the neutrinos are found, after propagation, as another flavor state when interacting with the detector. We will sketch a scheme for estimating the probability of changing the flavor from a state α to a state β in the vacuum. Let us start by stating the definition of a mass state as an eigenstate of the Hamiltonian operator $\mathcal{H}$:

$$\mathcal{H}\left|\nu_i\right\rangle = E_i\left|\nu_i\right\rangle , \tag{1.32}$$

with energy eigenvalue E_i. Consider the Schrodinger equation to obtain the time evolution of a flavor state in vacuum:

$$\left|\nu_\alpha(t)\right\rangle = \sum_i U^*_{\alpha i} e^{-iE_i t}\left|\nu_i\right\rangle . \tag{1.33}$$

Using the reverse transformation, because U is a unitary matrix,

$$\left|\nu_i\right\rangle = \sum_\alpha U_{\alpha i}\left|\nu_\alpha\right\rangle . \tag{1.34}$$

Then the time evolution of the state α can be expressed in terms of other flavor states:

$$\left|\nu_\alpha(t)\right\rangle = \sum_\beta \left(\sum_i U^*_{\alpha i} e^{-iE_i t} U_{\beta i}\right)\left|\nu_\beta\right\rangle . \tag{1.35}$$

In this formalism the probability for a state α to become a state β is then

$$\begin{aligned} P(\nu_\alpha \to \nu_\beta) &= \left|\left\langle \nu_\beta | \nu_\alpha(t)\right\rangle\right|^2 \\ &= \sum_{i,k} U^*_{\alpha i} U_{\beta i} U_{\alpha k} U^*_{\beta k} e^{-i(E_i - E_k)t} , \end{aligned} \tag{1.36}$$

which can be non-zero thanks to the matrix U.

1.4.2 Theoretical description of neutrino masses

NOS consequences are two-fold: neutrinos are massive particles and there is lepton mixing among the different flavors. These led to the necessity of introducing a mass term and a mixing matrix for the neutrinos, which are not included in the formulation of the SM. However, there is a problem: how can we introduce masses beyond the SM? Since there are no right-handed neutrino fields in the SM, N_R, we can not add a Dirac mass term as for the other SM fermions.

From the SM matter content we can only construct a Majorana mass term after the EWSB, like $m_\nu^{\alpha\beta}\overline{\nu}_{L\alpha}\nu^c_{L\beta}$, because there is no renormalizable invariant term that accounts for an interaction between the $SU(2)_L$ doublets $\overline{L}_L L_L^c$. The lowest order non-renormalizable operator, which generates Majorana neutrino masses after SSB, is the $D = 5$ Weinberg operator [37, 38], see Fig. 1.4, expressed as,

$$\begin{aligned} \mathcal{L}_{NonRen} &= -\frac{c_{\alpha\beta}}{\Lambda} \left(\overline{L}_{L\alpha}\tilde{H}\right) C \left(\overline{L}_{L\beta}\tilde{H}\right)^T + \text{H.c.} \\ &\xrightarrow{\text{SSB}} -\frac{1}{2} m_\nu^{\alpha\beta} \overline{\nu}_{L\alpha} \nu_{L\beta}^c + \text{H.c.} + ... \end{aligned} \tag{1.37}$$

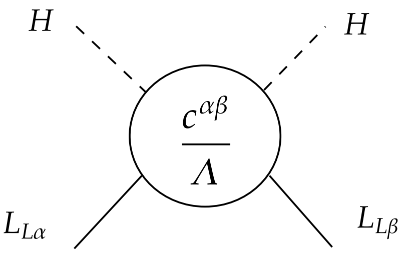

Figure 1.4: Feynman diagram for the $D = 5$ Weinberg operator. The diagram is supposed to be interpreted as a four-point interaction, see Ref. [39].

Here $c_{\alpha\beta}$ are complex constants, Λ is the scale of new physics and C is the charge-conjugate matrix in Dirac space: $C\gamma^\mu C^{-1} = -{\gamma^\mu}^T$, $C^\dagger = C^{-1}$, $C^T = -C$. For three generations of neutrinos there is a mismatch between the interaction and mass eigenstates parametrized as in Eq. (1.31).

On the other hand, unfortunately, the addition of a singlet right-handed neutrino, N_R, to generate Dirac masses through a new Yukawa couplings y_ν, like in the rest of the SM fermions, does not solve completely the problem. The drawback is the extremely small value acquired by the coupling, $y_\nu \sim \mathcal{O}(10^{-11})$, to explain the tiny light neutrino masses.

In this line of thought, we will comment on some of the most widely used extensions of the SM that lead to the Weinberg operator effectively at low energies.

The most appealing theoretical scheme to explain the neutrino masses is the *seesaw mechanism* [40–45], which comes in three forms: type I, II and III, depending on the extra particles that are added to the SM. In the types II and III, the additions are color-singlet $SU(2)_L$-triplet scalars and $SU(2)_L$-triplet fermions respectively, while in the seesaw type I, the one we focus in this thesis, the addition is of SM-singlet fermions, N_R.

In the seesaw type I, the tree-level exchange of heavy Majorana right-handed neutrinos, as depicted in Fig. 1.5, generate the Weinberg operator without breaking the SM gauge group. Because these heavy particles can have arbitrarily large masses, they can explain the smallness of neutrino masses in a very simple way. In detail, the SM plus n heavy right-handed neutrinos N_R has the Lagrangian:

$$\mathcal{L} = \mathcal{L}_{SM} + \overline{N}_{Ri} i\partial\!\!\!/ N_{Ri} - \left[y_\nu^{\alpha i} \overline{L}_{L\alpha} \tilde{H} N_{Ri} + \frac{1}{2} d_R^{ij} \overline{N}^c_{Ri} N_{Rj} + \text{H.c.} \right] , \tag{1.38}$$

where we consider the Majorana mass matrix: $d_R = diag(M_1, ..., M_n)$. The effective Weinberg couplings are given as

$$\frac{c^{\alpha\beta}}{\Lambda} \propto y_\nu^{\alpha i} \frac{1}{p\!\!\!/ - M_i} y_\nu^{\beta i} . \tag{1.39}$$

Bearing in mind that we are considering heavy neutrinos, i.e. $M_i^2 \gg p^2$, then

$$\frac{c^{\alpha\beta}}{\Lambda} \propto -y_\nu^{\alpha i} \frac{1}{M_i} y_\nu^{\beta i} = y_\nu^{\alpha i} \left(d_R^{ii} \right)^{-1} y_\nu^{\beta i} . \tag{1.40}$$

The light neutrinos would have the effective mass,

$$m_\nu \approx v_h^2 \left(y_\nu \, d_R^{-1} y_\nu^T \right) = m_D \, d_R^{-1} \, m_D^T , \tag{1.41}$$

where $m_D = v_h y_\nu$, would be the Dirac mass matrix. If the right-handed neutrinos are not diagonal in the Majorana mass matrix: $d_R \neq diag(M_1, .., M_n)$, the expression for m_ν in Eq. (1.41) still holds.

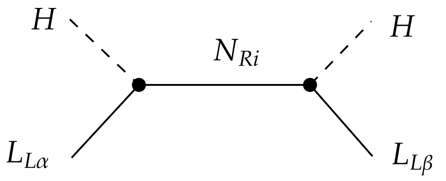

Figure 1.5: Diagramatic exchange interaction produced by integrating out the heavy particle N_{Ri}.

Block diagonalization

In this subsection, we cover the topic of block diagonalization applied to the seesaw mechanism in type I. This is a particular method for diagonalizing a mass matrix which is useful when considering the generalization of the seesaw mechanism to more generations of neutrino fields, see Ref. [46].

The mass matrix is:

$$M = \begin{pmatrix} 0 & m_D^T \\ m_D & M_R \end{pmatrix} , \tag{1.42}$$

expressed in the basis (ν_L^c, N_R). We assume that the Majorana mass matrix M_R is in general non-diagonal, symmetric and invertible, and m_D is an invertible matrix. The unitary transformation is carried with a unitary matrix U as:

$$U^T M U = \begin{pmatrix} \tilde{m}_\nu & 0 \\ 0 & \tilde{M}_R \end{pmatrix} . \tag{1.43}$$

The matrix U can be expressed as

$$U = \begin{pmatrix} \sqrt{1 - BB^\dagger} & B \\ -B^\dagger & \sqrt{1 - B^\dagger B} \end{pmatrix}, \qquad U^\dagger = \begin{pmatrix} \sqrt{1 - BB^\dagger} & -B \\ B^\dagger & \sqrt{1 - B^\dagger B} \end{pmatrix} , \tag{1.44}$$

where B is a complex matrix and its square root is understood as

$$\sqrt{1 - BB^\dagger} = 1 - \frac{1}{2} BB^\dagger - \frac{1}{8} BB^\dagger BB^\dagger ... - \frac{\Gamma\left(-1/2 + n\right)}{n!\Gamma(-1/2)} \left(BB^\dagger\right)^n . \tag{1.45}$$

Being U unitary order by order in $BB^\dagger$. Using Eq. (1.43) we obtain the following system:

$$\begin{cases} 0 & = \sqrt{1 - B^* B^T} m_D^T \sqrt{1 - B^\dagger B} - B^* m_D B - B^* M_R \sqrt{1 - B^\dagger B} \\ \tilde{m}_\nu & = -B^* m_D \sqrt{1 - BB^\dagger} - \sqrt{1 - B^* B^T} m_D^T B^\dagger + B^* M_R B^\dagger \\ \tilde{M}_R & = \sqrt{1 - B^T B^*} m_D B + B^T m_D^T \sqrt{1 - B^\dagger B} + \sqrt{1 - B^T B^*} M_R \sqrt{1 - B^\dagger B} . \end{cases} \tag{1.46}$$

Considering the limit: “$M_R \gg m_D$”; we can expand in terms of $1/M_R$, in which $B = B_1 + B_2 + ...$,

$$\sqrt{1 - B^\dagger B} \simeq 1 - \frac{1}{2} B_1^\dagger B_1 - \frac{1}{2} \left(B_1^\dagger B_2 + B_2^\dagger B_1\right) - ... . \tag{1.47}$$

Then solving Eq. (1.46) recursively,[7] we find for B_1 the relation:

$$B_1^* = m_D^T M_R^{-1}\,, \tag{1.48}$$

being $B_i \sim O(1/M_R^i)$. At order M_R^{-3} we have:

$$\begin{cases} \tilde{m}_\nu &= -m_D^T M_R^{-1} m_D + \frac{1}{2} m_D^T M_R^{-1}\left[m_D m_D^\dagger (M_R)^{-1} + (M_R^*)^{-1} m_D^* m_D^T\right] M_R^{-1} m_D \\ \tilde{M}_R &= M_R + \frac{1}{2}\left[m_D m_D^\dagger (M_R)^{-1} + (M_R)^{-1} m_D^* m_D^T\right]\,. \end{cases} \tag{1.49}$$

Notice that the first order terms are:

$$\tilde{m}_\nu = -m_D^T M_R^{-1} m_D\,, \qquad \tilde{M}_R = M_R\,, \tag{1.50}$$

to compare them with Eq. (1.41). In general, the $(n+1)$th term in the sum of the light neutrino mass has the same order of magnitude as the (n)th term in the sum of the heavy neutrino. From Eq. (1.50) it is possible to have small active neutrino masses, $\approx \mathcal{O}(10^{-2})\,$eV, if M_R is $\approx \mathcal{O}(10^{10})\,$GeV. The main disadvantage is related to the need for M_R to be so large, suggesting that the new physics is far away from the EW scale, which can be avoided in the *inverse seesaw model* discussed below.

Inverse seesaw model

In the inverse seesaw model (ISS) [48–52] it is introduced, in addition to three right-handed neutrinos N_R, three new singlet fermions χ_L with a Lagrangian as:

$$-\mathcal{L}_{\rm iss} = \overline{L}_L y_\nu N_R H + \overline{N}_R M_{\nu\chi} \chi_L + \frac{1}{2}\overline{\chi_L^c}\mu_\chi \chi_L + \text{H.c.}\,, \tag{1.51}$$

where y_ν, $M_{\nu\chi}$ and μ_χ are 3×3 matrices. Notice that if $\mu_\chi = 0$ then lepton number can be assigned in such a way that it is a conserved symmetry. After SSB the Lagrangian in Eq. (1.51) leads to the following Majorana mass matrix

$$\mathcal{L}_{\rm iss} = -\frac{1}{2}\begin{pmatrix}\overline{\nu_L^c} & \overline{N_R} & \overline{\chi_L^c}\end{pmatrix}\begin{pmatrix} 0 & y_\nu^*\langle H\rangle & 0 \\ y_\nu^\dagger\langle H\rangle & 0 & M_{\nu\chi} \\ 0 & M_{\nu\chi}^T & \mu_\chi \end{pmatrix}\begin{pmatrix}\nu_L \\ N_R^c \\ \chi_L\end{pmatrix} + \text{H.c.}\,. \tag{1.52}$$

If $\mu_\chi = 0$, it can be diagonalized exactly and leads to three Dirac neutrinos, whose masses squared are the eigenvalues of the matrix $M_{\nu_H}^2 = y_\nu^* y_\nu\,\langle H\rangle^2 + M_{\nu\chi}^\dagger M_{\nu\chi}$, and three exactly massless Weyl neutrinos. If $\mu_\chi \neq 0$, the would-be massless neutri-

---

[7] In Ref. [47] a formalism is given to evaluate the corrections to these expressions to arbitrary order.

nos acquire a mass matrix given by (in the limit "$M_{\nu\chi} \gg y_\nu \langle H \rangle$")

$$m_\nu \simeq -y_\nu^* \frac{\langle H \rangle}{M_{\nu\chi}^T} \mu_\chi \frac{\langle H \rangle}{M_{\nu\chi}} y_\nu^\dagger \,, \tag{1.53}$$

so that if μ_χ is small, m_ν can be smaller than $\mathcal{O}(1\,\mathrm{eV})$ even if y_ν and $M_{\nu\chi}$ are of orders $\mathcal{O}(1)$ and $\mathcal{O}(1\,\mathrm{TeV})$, respectively.

An interesting variation consists in taking $\mu_\chi = 0$ and adding a Majorana mass term for right-handed neutrinos, $\overline{N_R^c} \mu_\nu N_R$. In that case, active neutrino masses are not generated at tree level (the determinant of the mass matrix remains zero), but are generated at 1-loop level, see e.g. Ref. [53].

1.5 Introduction to dark matter

The Dark Matter (DM) is the scheme where new particle(s) can account for discrepancies between the theory of General Relativity's predictions and some observations at galactic, galaxy-cluster and cosmological scales. It constitutes a window to physics Beyond Standard Model (BSM), that will be addressed in this section.

In Sec. 1.5.1 we describe the evidence for DM, which would suggest they are massive particles, while also commenting on the non-gravitational experiments that set some of the DM properties. Finally, in Sec. 1.5.2, we consider the generation of the relic abundance of DM through the freeze-out mechanism.

1.5.1 Evidence of dark matter

Some of the observations that evidence disagreement between the estimates from General Relativity (GR)[8] and the content of visible matter are the following (based on Ref. [55]):

- *Rotation curves in spiral galaxies.* The orbital velocities of the stars, belonging to spiral galaxies, do not fall as Kepler's third law predicts as a function of the distance from the center, but rather at a much slower pace. The explanation could come from the existence of large concentrations of halos of DM surrounding these galaxies.

- *Temperature of the gas in elliptic galaxies.* The gas emitting X-rays is substantially hotter than the expected from the kinetic temperature of the visible stars, which could indicate that dark halos have a different velocity distribution. The same behavior happens at the level of galaxy-clusters.

- *Weak gravitational lensing of DM.* Light is bent or distorted on its path near massive objects that are not seen on telescopes. This sometimes completely modifies the line of sight of visible astronomical sources, phenomena called *lensing.*

- *Filaments in galaxy clusters.* From weak lensing it is possible to infer the distribution of matter in galaxy-clusters, which suggests the existence of filaments of DM among the constituent galaxies.

- *Bullet Cluster.* Two galaxy clusters are collisioning and make possible to distinguish separately the galaxies and gas or dust from the would be collisionless DM.

---

[8] For an introduction see e.g. Ref. [54].

Some of these phenomena can also be understood by a set of theories dubbed *Modified Gravity* [56, 57], which explore possible modifications of GR by introducing different gravitational field equations that could account for the observations. Although they have some difficulties to explain the Bullet Cluster. For a review see for instance Ref. [58].

Back to the DM scheme, for particles to explain the above observations they need to satisfy some phenomenologically motivated conditions, starting by being made of gauge singlet particles under all the symmetries of the SM in order to evade current detections. Furthermore, they should be stable or long lived and reproduce the measured DM abundance in the Universe.[9] The details are described in what follows.

Non-gravitational experimental constraints

Current detections are usually separated as Direct Detection (DD), Indirect Detection (DD) and production in accelerators, depending on the particles that appear in the initial/final states, see Fig. 1.6.[10]

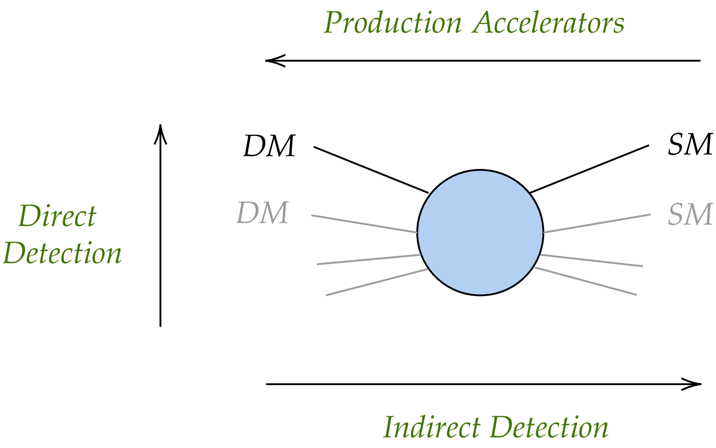

Figure 1.6: Schematic representation of the possible sources of detection of dark matter.

---

[9] The hypothesis of the formation of black holes in the early Universe suggested the possibility that they could account for at least part of the dark matter, see e.g. Refs. [59, 60].

[10] There are also other detection mechanisms of dark matter which go beyond this simplification, for example in beam dump experiments. Furthermore, in nuclear reactors the DM interacts with SM particles produced from fissions, decays of fission products, capture processes in the fuel material, among others, see e.g. Refs. [61–63].

Thereby, DD [64] are measurements of the possible elastic scattering between the DM and SM particles, in particular atomic nuclei.[11] In many cases the strongest bounds of DD come from the Spin Independent (SI) cross section, which corresponds to a magnitude that is independent of the spin of the DM particle and the angular momentum of the nucleus. Correspondingly, the DM particle coherently interacts with the entire nuclei rather than with a single unpaired nucleon.

So far no experiment observed a statistically significant excess in measurements above the background expectation values, and therefore any model with DM should satisfy the detection bounds summarized in Fig. 1.7, where some of the most relevant results in DD are shown.[12] As can be noticed, above $m_{DM} \approx 5\,\mathrm{GeV}/c^2$ the experiment with the highest sensitivity to DM particles is XENON1T (based on liquid xenon), while in the range $1.8\,\mathrm{GeV}/c^2 < m_{\mathrm{DM}} < 5\,\mathrm{GeV}/c^2$ it is the DarkSide-50 (based on liquid argon). Later, we will define WIMPs but for the time being consider them as a synonym of dark matter.

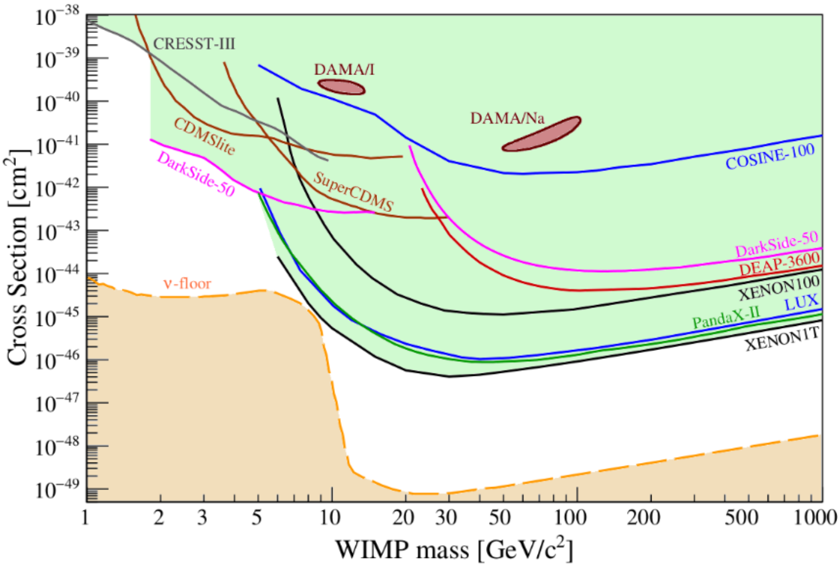

Figure 1.7: Review of current experimental parameter space for spin-independent WIMP-nucleon cross sections. The region above the lines is excluded at a 90% CL. Results extracted from Ref. [64]. Some more recent reviews/experiments can be found in Refs. [71–74].

On the other hand, ID measurements are sensitive to the decay or annihilation

---

[11] For searches on new physics signals from neutrino-nucleus scattering see e.g. Refs. [65, 66].

[12] There is an exception to the null results that comes from the DAMA/LIBRA collaboration [67–70], although there is a strong tension with the other measurements.

products from DM to SM particles. Some of the possible constraints come from different sources: the Planck cosmic microwave background (CMB) measurements, Fermi observations of gamma rays from the Galactic center and from dwarf spheroidal galaxies, AMS-02 observations of antiprotons and neutrino experiments [75–80]. The first one is associated to the state of DM particles at various epochs of the Universe while the others with DM only in the current state. We will focus on the first two experiments.

The *Planck* CMB measurements set bounds on the rate of annihilation of dark matter to SM particles, as the production of extra SM particles can be absorbed by the surrounding gas, causing the gas to heat and ionize. These scatter the CMB photons that would later come to us, modifying the CMB power spectra by a partial homogenization of the CMB temperature relative to the standard predictions in ΛCDM models. Furthermore, it would cause the alteration of the free electron fraction (the abundance ratio of free electrons to hydrogen atoms), which in turn affects the ionization history of the Universe. In this manner the precise measurements of the CMB can place important bounds on the dark matter masses and properties.

The Fermi-LAT observations of dwarf spheroidal satellite galaxies (dSphs) of the Milky Way provide limits on the annihilation of DM that lead to an excess in the gamma-ray flux above the astrophysical backgrounds in the 500 MeV–500 GeV range of photon-energy. The dSphs are excellent targets to search for γ-rays, resulted from DM annihilation, due to: their proximity, their large DM density (having mass to light ratios in the 10–2000 range) and the absence of observational evidence for non-thermal astrophysical processes that produce γ-rays. Consequently, they are very clean sources with a large signal-to-background ratio compared to ID observations focused on the Galatic center. The advantage of this type of ID searches is that if a line is measured in the photon spectrum, the mass of the DM candidate would be identified.

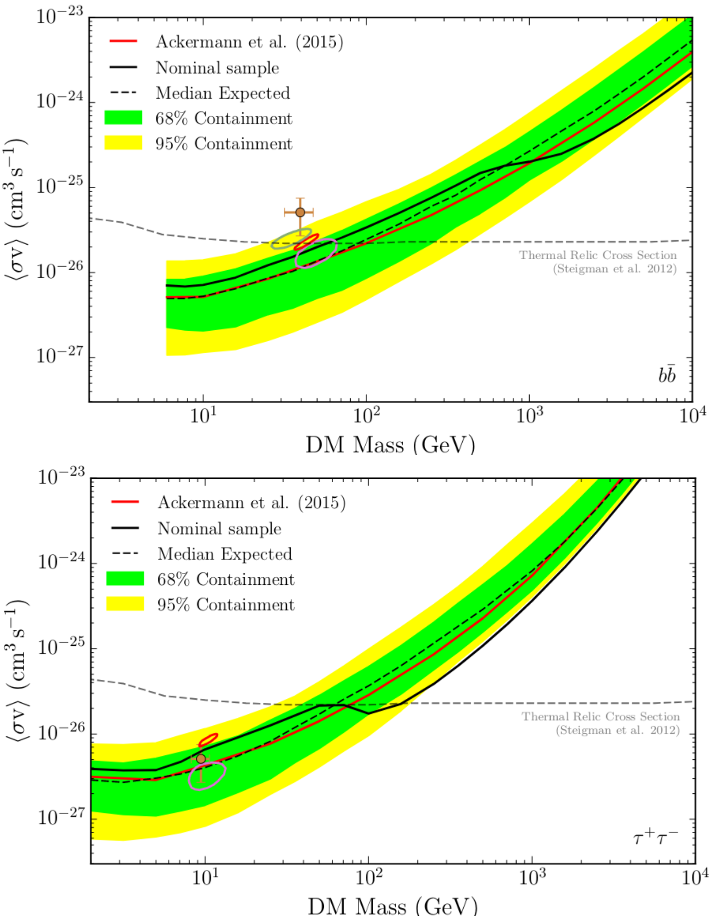

Figure 1.8: Upper limits of Ref. [81] in 95% CL on the DM annihilation cross section derived from a combined analysis of the nominal target sample for the $b\bar{b}$ (top) and $\tau^+\tau^-$ (bottom) channels. The dashed line shows the median expected sensitivity while the bands represent the 95% and 68% quantiles. The red and black lines and closed contours are described in Ref. [81]. More recent results can be found in e.g. Refs. [82–84].

However, the measurements found no statistically significant ($> 3\sigma$) γ-ray excesses in the experiments; the upper limits on the annihilation cross sections for the $b\bar{b}$ and $\tau^+\tau^-$ channels can be seen in Fig. 1.8.

Finally, collider searches look for the missing energy and momentum carried away by stable DM particles that were produced in the collisions, but escape the detector volume without interacting. Because stable DM particles are not seen in the detectors, most searches at colliders do not measure directly the cross section to produce the DM particles, $\sigma_{SM\,SM \to DM\,DM}$, but rather the cross section leading to heavier exotic particles that later decay to stable DM final states, before achieving the detectors, $\sigma_{SM\to exotic}$, see e.g. Ref. [85]. Collider searches also constrain models through precision studies of the visible decays of the Z and Higgs bosons, see e.g. Ref. [86], as these particles are light compared to the LHC energy and so can be produced on-shell. These include the so called invisible decaying Higgs and Z bosons searches.

Dark matter portals

Given the overwhelming evidence of DM having, if any, tiny non-gravitational interactions with the SM particles, it is reasonable to consider that these interactions do not take place directly but through a mediator particle.

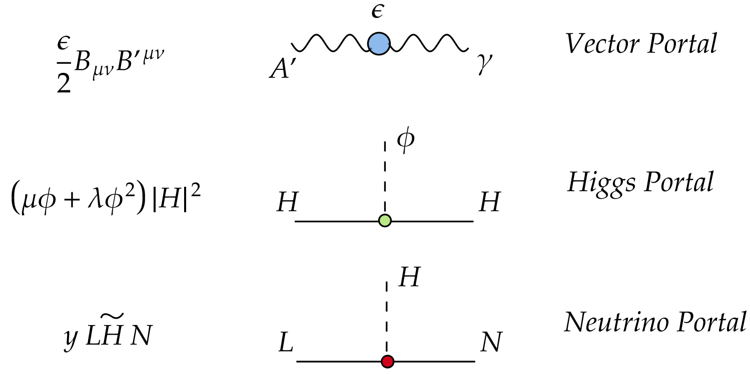

Figure 1.9: Schematic representation of DM portals. The fields N, ϕ and B'_μ correspond to the right-handed neutrino, scalar and vector bosons respectively.

This mediator would play the role of portal between the two sectors. At the renormalizable level, such interactions can proceed through the following three SM operators: $B_{\mu\nu}$, $|H|^2$, and $\tilde{H}L$, known as the *vector* [87, 88], *Higgs* [89, 90], and *neutrino portals* [91, 92] respectively, see Fig. 1.9. These portal operators will be important for Chs. 5 and 6.

1.5.2 The relic abundance and freeze-out mechanism

The dark matter relic abundance in the Universe is expressed in terms of the cosmological density parameter $\Omega_{DM}h^2 = \rho_{DM}/\rho_c$, where h is the normalised Hubble parameter and ρ_c and ρ_{DM} are the critical density to recover a flat Universe and the

DM energy density, respectively. The value measured by the Planck Collaboration [53] is $\Omega h^2 = 0.120 \pm 0.001$.

There are a number of possible mechanisms to reproduce the abundance of DM, however the main two are the *freeze-out* and *freeze-in* schemes. The former relies on the assumption that at some point in the early Universe the DM is in *thermal equilibrium* with the SM particles; while the latter requires the thermal equilibrium to never occur and the number density early on to be negligible compared to the SM particles. In this thesis, we will only consider the freeze-out scheme and a detailed explanation of its principles will be developed in the following.

The thermal equilibrium (THEQ) of a species with the thermal bath happens when it is in kinetic and chemical equilibrium at the same time. Kinetic equilibrium between two particle species, e.g. η and ψ, occurs when their rate of elastic scattering is large enough compared to the expansion of the Universe. This leads the species to acquire a common temperature. An usual rough criteria to see whether η is in kinetic equilibrium with ψ at a given temperature T consists in the rate of scattering $\eta\,\psi \leftrightarrow \eta\,\psi$ being larger than the Hubble parameter $H(T)$ (defined in App. E):

$$\Gamma_{\eta\,\psi\leftrightarrow\eta\,\psi}(T) > H(T)\,, \tag{1.54}$$

with notation $\Gamma_i = n_\eta \langle \sigma v\rangle_i$, σ_i is the cross section of process i and v is the "relative velocity" [93].

On the other side, chemical equilibrium between two particle species happens when those interactions changing the total number of the species are large enough compared to the expansion of the Universe. Such an interaction could be the annihilation $\eta\,\eta \leftrightarrow \psi\,\psi$ and leads to a relation between the chemical potentials: $\mu_\eta = \mu_\psi$. In the same manner, the criteria for η to be in chemical equilibrium with ψ is:

$$\Gamma_{\eta\,\eta\leftrightarrow\psi\,\psi}(T) > H(T)\,. \tag{1.55}$$

In this thesis we will consider THEQ for the dark matter particles and therefore focus on the freeze-out mechanism. The quantity to trace with regard to the DM abundance is the number density of particles n, define as

$$n = \frac{g}{(2\pi)^3}\int f(p)\, d^3p\,, \tag{1.56}$$

where $f(p)$ is the distribution function in momentum space and g the number of degrees of freedom of the species. The consequence of the kinetic equilibrium for $f(p)$ is that it should follow the Bose-Einstein/Fermi-Dirac distribution for bosons/fermions, known as equilibrium distribution:

$$f(p) = \frac{1}{\exp[(E-\mu)/T] \pm 1}\,, \tag{1.57}$$

where E is the energy and μ the chemical potential. For relativistic and non-relativistic particles the number density can be approximated, respectively, by[13]

$$n_{eq}^{rel}(T) = \frac{g_{eff}}{\pi^2}\zeta(3)T^3, \quad n_{eq}^{non\text{-}rel}(T) = g\left(\frac{mT}{2\pi}\right)^{3/2} e^{-m/T}\,, \tag{1.58}$$

where ζ is the Riemann zeta function and $g_{eff} = g\,[3g/4]$ for bosons [fermions]. For convenience, the number density is normalized with the volume of the Universe, through the total entropy density s, to a new variable we call yield: $Y = n/s$. If we consider the Universe with total energy ρ and pressure p densities well approximated by those of the SM, and it is isotropic and homogeneous, the total entropy S is

$$s = \frac{S}{V} = \frac{\rho + p}{T} \quad \rightarrow \quad s\,(T) = \frac{2\pi^2}{45} g_{*s} T^3\,, \tag{1.59}$$

where g_{*s} is the number of relativistic degrees of freedom of the SM in entropy, see Fig. 1.10, and V is the volume of the Universe. Then the corresponding approximate yields are

$$Y_{eq}^{rel} = \frac{45}{2\pi^4}\zeta(3)\frac{g_{eff}}{g_{*s}}, \quad Y_{eq}^{non\text{-}rel} = \frac{45}{2\pi^4}\left(\frac{\pi}{8}\right)^{1/2}\frac{g}{g_{*s}}\left(\frac{m}{T}\right)^{3/2} e^{-m/T}\,. \tag{1.60}$$

Notice that if the particles follow the equilibrium all along the evolution of the Universe then their number densities will be very close to zero at the present temperature, as the exponential suppression in Eq. (1.60) or the dashed-line of Fig. 1.11 suggests. Due to this, the particles need to leave the equilibrium early enough to account for the present value of the relic abundance.

We develop now in detail the evolution of the number density of DM, which we identify with particle 1, that results from the equality between the Liouville ($\hat{L}[f_1]$) and collisional ($C[f_1]$) operators. The first is defined as

$$\hat{L} = p_\mu \frac{\partial}{\partial x^\mu} - \Gamma^\mu_{\sigma\rho} p^\sigma p^\rho \frac{\partial}{\partial p^\mu}\,. \tag{1.61}$$

The second operator takes into account all the processes that change the number

---

[13] For simplicity, it is customary to assume zero chemical potential when the species is in chemical equilibrium with the heat bath, see Ref. [94].

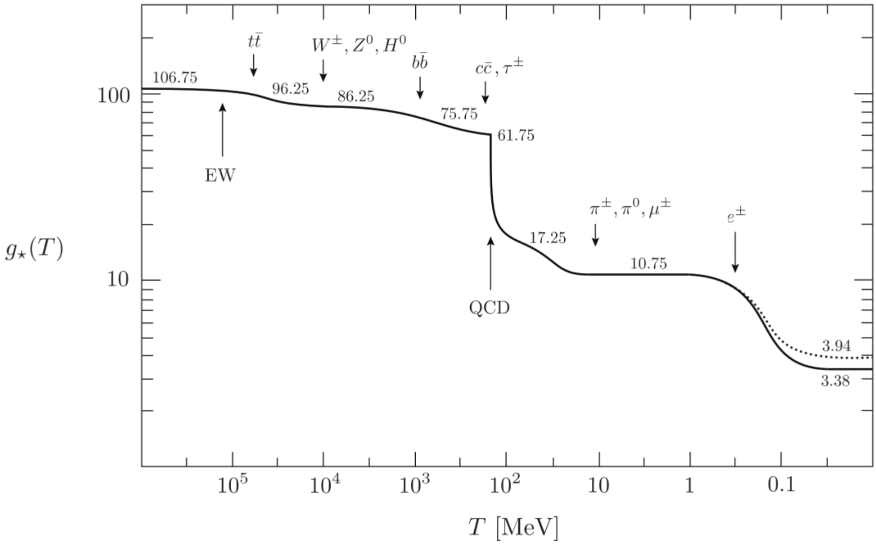

Figure 1.10: Relativistic degrees of freedom $g_*(T)$ of SM content as a function of the temperature. The dotted line corresponds to the number of effective degrees of freedom in entropy $g_{*s}(T)$. Extracted from Refs. [95, 96].

of DM particles (e.g. 2 ↔ 2 annihilations). The integration of the equality over the momentum space leads to an expression in terms of the number density:

$$\frac{dn_1}{dt} + 3Hn_1 = \frac{g_1}{(2\pi)^3} \int \frac{C[f_1]}{E_1} d^3p_1 \,, \tag{1.62}$$

and in case of an annihilation process, see Fig. 1.12, the collisional operator is

$$\begin{aligned} \frac{g_1}{(2\pi)^3} \int \frac{C[f_1]}{E_1} d^3p_1 = - \int d\Pi_1 d\Pi_2 d\Pi_3 d\Pi_4 (2\pi)^4 \delta^4 \left(p_1 + p_2 - p_3 - p_4\right) \\ \left[|M_{1,2\to3,4}|^2 f_1 f_2 (1 \pm f_3)(1 \pm f_4) - |M_{3,4\to1,2}|^2 f_3 f_4 (1 \pm f_1)(1 \pm f_2)\right] \,, \end{aligned} \tag{1.63}$$

with $d\Pi_i = (g_i/2\pi^3) dp_i^3/2E_i$ and (+) applies to bosons and (−) to fermions.

We consider the annihilation process to be CP and T invariant, so $|M_{1,2\to3,4}|^2 \equiv |M_{3,4\to1,2}|^2$. Moreover, we will make the following assumptions: (i) the approximation $1 \pm f_i \sim 1$ holds, (ii) detailed balance among the equilibrium distributions $f_1^{eq} f_2^{eq} = f_3^{eq} f_4^{eq}$ and (iii) particles 3 and 4 are in thermal equilibrium with the thermal bath: $f_3 = f_3^{eq}$ and $f_4 = f_4^{eq}$.[14]

---

[14] It is necessary to assume that the final state particles go into equilibrium with the thermal bath as soon as they are created, which is safe to consider when they are strongly-interacting SM particles.

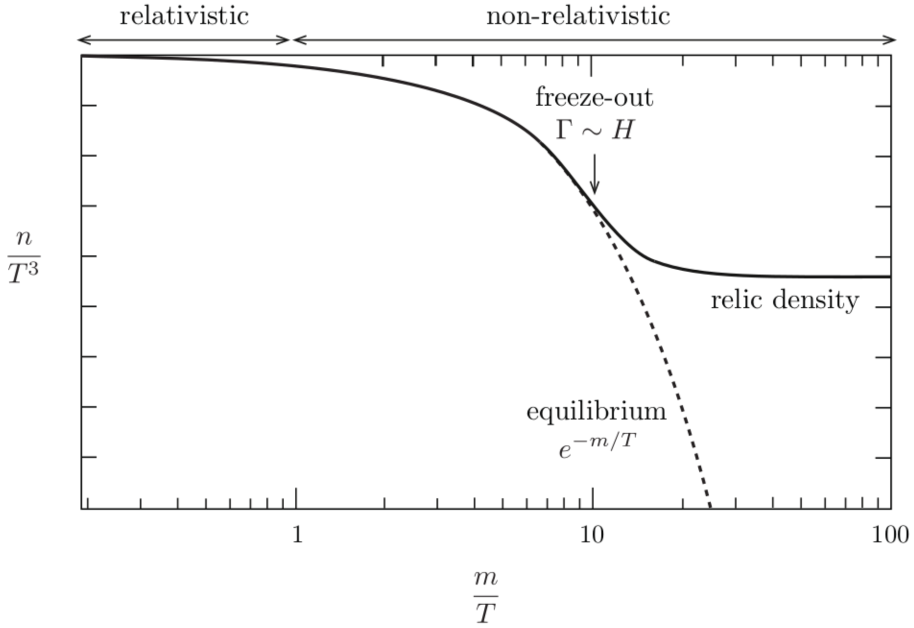

Figure 1.11: Schematic representation of particles freeze-out, where at high temperatures the equilibrium values are traced and at low temperatures the particles are freeze-out, maintaining a density that is much larger than the equilibrium values. m corresponds to the dark matter mass. Extracted from Ref. [96].

The relation in (ii) can be motivated by energy conservation,

$$f_1^{eq} f_2^{eq} \propto \exp\left(-(E_1+E_2)/T\right) = \exp\left(-(E_3+E_4)/T\right) \propto f_3^{eq} f_4^{eq} \,. \tag{1.64}$$

The phase space can be reduced as

$$\int (2\pi)^4 \delta^4 (p_1+p_2-p_3-p_4) \frac{d^3p_3}{(2\pi)^3 2E_3} \frac{d^3p_4}{(2\pi)^3 2E_4} = \int d\Omega \frac{\sqrt{\lambda\left(s, m_3^2, m_4^2\right)}}{32\pi^2 s} \,, \tag{1.65}$$

with the Mandelstam variable $s = (p_1+p_2)^2$. So

$$\begin{aligned} \frac{g_1}{(2\pi)^3} \int \frac{C[f_1]}{E_1} d^3p_1 = - \int |M_{1,2\to 3,4}|^2 \left[f_1 f_2 - f_1^{eq} f_2^{eq}\right] \frac{d^3p_1}{(2\pi)^3 2E_1} \\ \frac{d^3p_2}{(2\pi)^3 2E_2} d\Omega \frac{\sqrt{\lambda\left(s, m_3^2, m_4^2\right)}}{32\pi^2 s} \,, \end{aligned} \tag{1.66}$$

The distributions in kinetic and chemical equilibrium are proportional to each

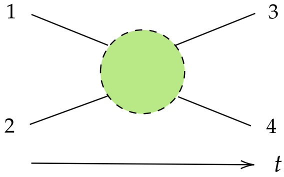

Figure 1.12: Schematic representation of particle annihilations 1, 2 → 3, 4.

other, with a proportionality factor that is independent on the momentum, see Refs. [93, 97]. So we can make the following trick for any momentum dependent function $h(p)$:

$$\int f_1(p_1)h(p_1)\frac{d^3p_1}{(2\pi)^3} = \int f_1^{eq}(p_1)h(p_1)\frac{d^3p_1}{(2\pi)^3}\frac{n_1}{n_{1,eq}} \,. \tag{1.67}$$

This leads to an expression of the collisional operator in terms of the thermal-averaged annihilation cross section $\langle\sigma v\rangle$:

$$\frac{g_1}{(2\pi)^3}\int\frac{C[f_1]}{E_1}d^3p_1 = -\langle\sigma v\rangle\left(n_1n_2 - n_{1,eq}n_{2,eq}\right) \,, \tag{1.68}$$

with

$$\langle\sigma v\rangle = \int |M_{1,2\to3,4}|^2 f_1^{eq} f_2^{eq}\frac{d^3p_1}{(2\pi)^3\,2E_1}\frac{d^3p_2}{(2\pi)^3\,2E_2}d\Omega\frac{\sqrt{\lambda\left(s,m_3^2,m_4^2\right)}}{32\pi^2 s} \,. \tag{1.69}$$

Finally we obtain the so-called *Boltzmann equation*:

$$\frac{dn}{dt} + 3Hn = -\langle\sigma v\rangle\left(n^2 - n_{eq}^2\right) \,, \tag{1.70}$$

where we have considered that particles 1 and 2 are identical: $n = n_1 = n_2$.[15] It is important to mention that the Boltzmann equation is explicitly covariant; however, when the particle distributions have been fixed a frame is singled out, the *comoving frame*, and the covariance is broken.

The evolution on the yield ($Y = n/s$) in terms of $x = m_{DM}/T$ is

$$\boxed{\frac{dY(x)}{dx} = -\frac{s\langle\sigma v\rangle}{xH}\left(Y^2 - Y_{eq}^2\right)} \,, \tag{1.71}$$

---

[15] For non-identical particles see Ref. [94]

which can be expressed as in Eq. (5.26) of Ref. [94],

$$\frac{x}{Y_{eq}}\frac{dY}{dx} = -\frac{sY_{eq}\langle\sigma v\rangle}{H}\left(\left(\frac{Y}{Y_{eq}}\right)^2 - 1\right) . \tag{1.72}$$

From Eq. (1.72), one sees that the typical behavior of the solution $Y(x)$ is to follow the equilibrium $Y_{eq}(x)$ until the function $sY_{eq}\langle\sigma v\rangle(x)$ is smaller than the expansion of the Universe, which is quantified by the Hubble rate $H(x)$, see Fig. 1.11. The instant when this occurs is called *freeze-out* and it is defined as the moment when $Y - Y_{eq} \equiv c_f Y_{eq}$ for some typical values of c_f between 1.5 and 2.5.[16]

Freeze-out approximation and WIMPs

In the following, we will make some approximations to estimate the values of the yield Y and the thermal-average annihilation cross section $\langle\sigma v\rangle$, that reproduce or correspond to the correct relic abundance. To estimate the freeze-out moment, x_f, let us assume that it occurs when $\Delta = c_f Y_{eq}$ and $d\Delta/dx = 0$ for $\Delta \equiv Y - Y_{eq}$, so from Eq. (1.71) we arrive at:

$$\Delta = -\frac{dY_{eq}/dx}{Y_{eq}}\frac{x^2}{2\lambda\langle\sigma v\rangle} , \quad \text{with } \lambda = \frac{s\,x}{H} , \tag{1.73}$$

from which x_f can be obtained. After freeze-out we could assume $Y(x) \gg Y_{eq}(x)$ and so Eq. (1.71) is simplified to

$$\frac{dY}{dx} = -\frac{\lambda\langle\sigma v\rangle}{x^2}Y^2 , \tag{1.74}$$

This equation can be integrated from the freeze-out at x_f till present at x_0. On another hand, the thermal-averaged cross section $\langle\sigma v\rangle$ can be expanded in powers of x^{-1}, which is usually truncated at the second power, i.e. $\langle\sigma v\rangle = a + b/x$:

$$\int_{Y_f}^{Y_0}\frac{dY}{Y^2} = -\int_{x_f}^{x_0}\frac{\lambda\langle\sigma v\rangle}{x^2}dx \quad \rightarrow \quad \frac{1}{Y_0} = \frac{1}{Y_f} + \frac{\lambda}{x_f}\left(a + \frac{b}{2x_f}\right) , \tag{1.75}$$

with the simplification $x_0 \gg x_f$ and Y_f corresponds to the yield at freeze-out, $Y_f \approx (c_f + 1)Y_{eq}(x_f)$. Now let us assume, for the sake of making some estimates, that we can ignore $1/Y_f$, and then finally we have the approximation:

$$\Omega h^2 = \frac{m_\chi Y_0 s_0 h^2}{\rho_c} \approx 5 \times 10^{-12}\,\text{GeV}^{-2}\frac{x_f}{a + b/(2x_f)} , \tag{1.76}$$

---

[16] For example, `micrOMEGAs` considers $c_f = 2.5$, see Refs. [98, 99].

with s_0 being the total entropy density today. This expression shows the inverse relation between the value of relic abundance and the annihilation cross section. We call this approximation to compute the relic abundance as the *analytical approach*, which will be employed in later sections.

The *Weakly Interacting Massive Particles* (WIMP) is referred to a generic class of DM candidates with masses in the range 1 to $10^5\,\mathrm{GeV}/c^2$, so the cross sections go from 10^{-41} to $10^{-51}\,cm^2$, as Eq. (1.76) would suggest [64]. The scenario arises naturally in many BSM models, e.g. as the neutralino in supersymmetric theories or as the lightest Kaluza-Klein particle in theories with extra spacetime dimensions.

Chapter 2

Alternatives to the standard scenario

In this chapter, we review a selection of models in CHT scenarios that employ the RGEs approach (described in Sec. 1.3) with the aim of predicting the measured values of masses: $m_h \approx 125\,\text{GeV}$ and $m_t \approx 173\,\text{GeV}$. We also discuss the effects of the infrared fixed point features of the corresponding RGEs in the final results for $m_{t,h}$ and in the consistency of the framework.

2.1 Infrared fixed points in standard scenario

The coupled RGEs from the BHL Lagrangian in Eq. (1.17) are,

$$\begin{cases} 16\pi^2\beta_{y_t} = 9y_t^3/2 - 8g_3^2\, y_t\,, \\ 16\pi^2\beta_{\lambda_H} = 12\lambda_H^2 + 12\lambda_H\, y_t^2 - 12y_t^4\,. \end{cases} \tag{2.1}$$

The solutions of the differential equations can be analyzed by looking at the collection of equilibrium points, and their properties, which sets the behavior in general. In doing so, vector fields are plotted in the top panel of Fig. 2.1, corresponding to the variables λ_H and y_t in Eq. (2.1), for a fixed and schematic value of g_3 evaluated at $\mu = 173\,\text{GeV}$ and neglecting electroweak couplings. There is an equilibrium point in red that is an *attractor point*, and clearly reveals how complicated it is to reach the correct values of the couplings, which are represented by the black dot. This red point is called *infrared fixed point* because solutions with very different initial conditions at Λ converge together.

From that plot, we can naively look for the region of parameter space in y_t

and λ_H where the evolution with the SM RGEs leads to closer predictions to the measured values of $m_{t,h}$ (approaching the black dot) at $\mu \to m_Z$. This region is likely to be the area confined by the dashed curve; therefore, it can also be considered as the region of parameter space where new physics appears at some larger energy scale Λ_{max} (i.e. a new massive particle decouples at $\mu < \Lambda_{max}$)[1]. However, although useful, the vector field in the plot does not provide information on the pace of the evolution.

In Ref. [100], it is plotted the simultaneous evolution of the couplings λ_H and y_t for arbitrary initial values, see Fig. 2.2a. One can see that the spectrum of initial conditions, from large to small values, finishes on the dashed curve of Fig. 2.2a. The latter curve shows the relation between the predicted masses m_H and m_t in the SM, portrayed in the curve of Fig. 2.2b.

2.2 Composite scalars with neutrinos

In the light of BHL's results being unsatisfying, S.P. Martin [101] considered some radical modifications by adding neutrinos to the picture; therefore, they can "share the burden", as he wrote, with the top quark t to form the Higgs bound state.

Other SM particles are not considered in the same way because the composite scheme relies on Yukawa couplings of order $\mathcal{O}(1)$, which spoil their mass predictions after EWSB for being too large. Conversely, the trick is to add a right-handed neutrino N_R and work within the seesaw mechanism, explained in Sec. 1.4.2. Martin's four-fermion interaction is:

$$\mathcal{L}_\Lambda = +(\kappa_t \overline{Q}_L t_R + \kappa_\nu \overline{L}_L N_R)\left(\kappa_t \bar{t}_R Q_L + \kappa_\nu \overline{N}_R L_L\right) , \tag{2.2}$$

and so there is only one extra degree of freedom, κ_ν/κ_t. After bosonization we get the Yukawa-type interaction (and include by hand a Majorana mass M),

$$\mathcal{L} = \mathcal{L}_{SM} + \left(y_\nu \overline{L}\tilde{H} N_R + \frac{M}{2} \overline{N}_R^c N_R + \text{H.c.} \right) . \tag{2.3}$$

Because the light neutrino masses are known to be of order 0.05 eV, there is only one extra free parameter compared to BHL, which is set to be the additional Majorana mass M, serving as a new scale in between the EW and Planck's. The corresponding CC in the RGE approach are

$$y_t,\, y_\nu(\mu) \to \infty\,, \quad \text{for } \mu \to \Lambda\,. \tag{2.4}$$

---

[1] The scale Λ_{max} is identified as the maximum scale at which the SM is valid, see Sec. 1.2.

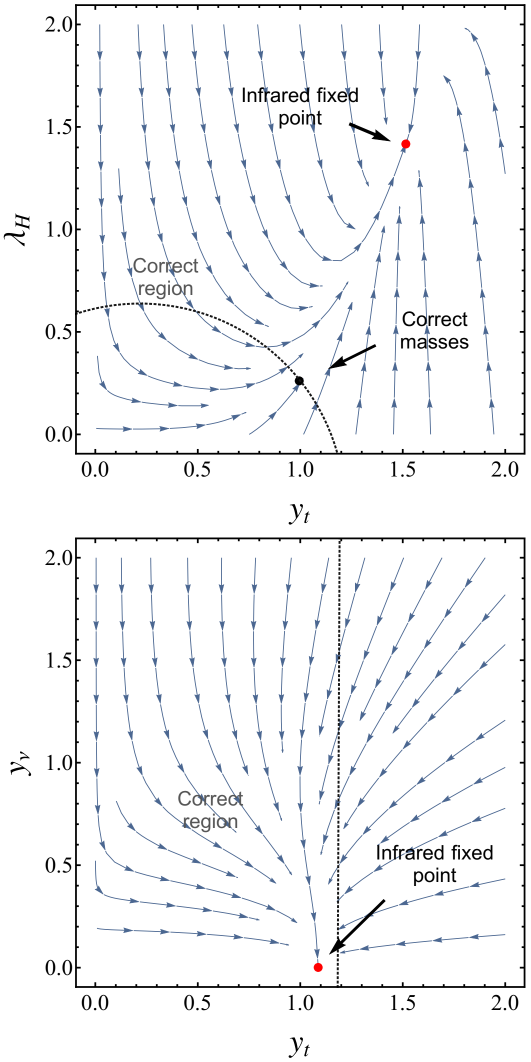

Figure 2.1: Vector fields in the variables y_t and λ_H using the SM RGEs (BHL model) in the top panel. Vector fields in y_t and y_ν for Martin's model in the bottom panel. The directions of the vector fields correspond to the evolution of the couplings from large to small energies. The red and black points correspond to the infrared fixed point and experimental values, respectively. The dashed curves define the region in the parameters y_t and λ_H for the correct predictions of $m_{t,h}$, see text. The gauge coupling g_3 is evaluated at the scale $\mu = 173\,(M_\omega)\,\text{GeV}$ in the top (bottom) panel, with the illustrative value $M_\omega = 10^6\,\text{GeV}$.

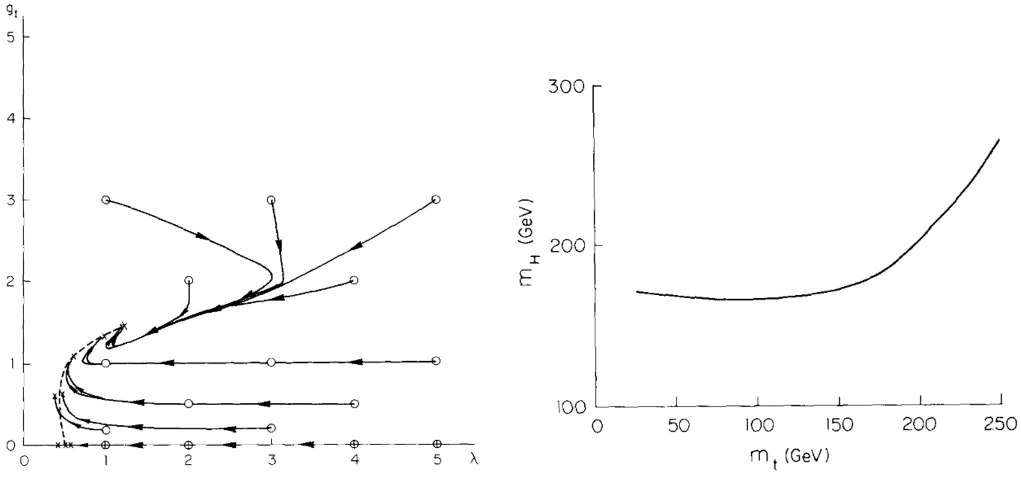

(a) (b)

Figure 2.2: The left panel shows the flow of the couplings λ_H and g_t for arbitrary initial conditions for the BHL model. The coupling g_t corresponds to y_t in this thesis. The dashed curve indicates the end of the different trayectories, which gives a relation between the masses of the Higgs boson and the top quark as it is shown in the right panel. Extracted from Ref. [100].

Unfortunately, Martin concluded that his model is unable to achieve the correct predictions, although it is an improvement with respect to BHL.[2] This is due to a drawback that the model faced, where the energy scale of the Majorana mass has to be, at least, $M \approx 10^{13}\,\text{GeV}$ in the see-saw type I scheme. This strongly constraints the span where the running of the couplings take place, and then the correct lower values of $m_{t,h}$ are not reached. This can be schematically understood from the vector field analysis, see bottom panel of Fig. 2.1, as the RGE-solutions should be very close to the equilibrium point at the EW scale, the red dot; required in order to be near the black dot in the top panel of Fig. 2.1.

Afterwards, Hill and Krog (HK) [103] proposed a new model that is able to achieve the correct masses of both particles at the same time. They considered three families of neutrinos, with identical couplings, which can widen the range of values that the couplings access along the evolution of the RGEs (reaching the red dot in the bottom panel of Fig. 2.1). For example, considering n_f generations of neutrinos, the RGE for the top's Yukawa coupling, before the neutrinos decouple at the same

---

[2] An interesting work has been presented in Ref. [102] using the seesaw mechanism. In contrast with Ref. [101], they considered two Higgs doublets made out of quarks and leptons (neutrinos included) condensates separately.

scale M, is given as:

$$16\pi^2\beta_{y_t} = y_t\left(\frac{9}{2}y_t^2 + n_f y_\nu^2 + \dots\right), \tag{2.5}$$

where the dots represent the SM gauge contributions. Then, naturally, an increase in the parameter n_f results in the desirable larger decrease in y_t from its value at Λ.

Furthermore, HK introduced a fundamental neutral scalar singlet, S, at the EW scale, which develops a VEV, $\langle S\rangle \neq 0$. Therefore this scalar mixes with the CP-even component of the doublet H, leading to propose that the lighter mass eigenstate is the observed Higgs boson h. If it is assumed $\langle S\rangle \gg \langle H\rangle$,

$$m_h^2 \simeq 2\left(\lambda_H - \frac{\lambda_{HS}^2}{\lambda_S}\right)\langle H\rangle^2, \tag{2.6}$$

where λ_H, λ_S and λ_{HS} are the quartic couplings of H, S and H-S respectively (see Eq. (14) in Ref. [103]). From Eq. (2.6), it is evident that m_h can be small even if all the quartic couplings are of order $\mathcal{O}(1)$. Note that in the HK setup only λ_H is fixed by the CC, coming from Eq. (2.4), while λ_{HS} and λ_S are completely free parameters; this reduces the predictability of HK's model. Unfortunately, this scenario naturally leads us to question why the two scalars are not composite states.

2.3 Accommodating light quark masses with a colored scalar

In this section we comment on a different scenario to improve BHL, compared to Martin and HK models, where instead of adding an extra fermion to the SM, one includes another four-fermion interaction which incorporates a different color structure. Consequently, there are new scalars that are charged under $SU(3)_c$ and dubbed *colored scalars*. Furthermore, the scenario incorporates the necessary interactions of the colored scalars to induce a mass for the b quark at 1-loop level out of the top, explaining the hierarchy $m_b \ll m_t$.

The scenario is proposed by Babu and Mohapatra (BM) [104], where new four-fermion interactions at the composite scale Λ generate two color-triplet scalars, $\omega_{1,2}$, at low energy scales. BM considered the following Lagrangian involving Q_L, t_R and

b_R,

$$\begin{aligned}\mathcal{L}_\Lambda =& G_t\, \bar{Q}_{Li} t^i_R \bar{t}_{Rj} Q^j_L + G_1\, Q^{iT}_L C^{-1} i\tau_2 Q^j_L Q^\dagger_{Lk} i\tau_2 C^{-1} Q^*_{Ll} \epsilon_{ijm} \epsilon^{klm} \\ &+ G_2\, t^{iT}_R C^{-1} b^j_R b^\dagger_{Rk} C^{-1} t^*_{Rl} \epsilon_{ijm} \epsilon^{klm} \\ &+ G_3 \left(Q^{iT}_L C^{-1} i\tau_2 Q^j_L b^\dagger_{Rk} C^{-1} t^*_{Rl} \epsilon_{ijm} \epsilon^{klm} + \text{H.c.} \right) ,\end{aligned} \tag{2.7}$$

with $SU(3)_c$ indexes and C is the charge-conjugate matrix. The couplings G_i should not be overly large to induce spontaneous symmetry breaking of $SU(3)_c$ as $\langle Q^{iT}_L C^{-1} i\tau_2 Q^j_L \rangle \neq 0$ or $\langle t^{iT}_R C^{-1} t^j_R \rangle \neq 0$. The EFT Lagrangian at the EW scale is given as $\mathcal{L}_{EFT} = \mathcal{L}_{Yuk} + V_{EFT}$,[3]

$$\begin{aligned}\mathcal{L}_{Yuk} =& y_t\, \bar{Q}_L H t_R + f_1\, Q^{iT}_L C^{-1} i\tau_2 Q^j_L \omega^k_1 \epsilon_{ijk} \\ &+ f_2\, t^{iT}_R C^{-1} b^j_R \omega^k_2 \epsilon_{ijk} + \text{H.c.} ,\end{aligned} \tag{2.8}$$

and

$$\begin{aligned}V_{EFT} =& \mu^2_\phi H^\dagger H + \mu^2_1 \omega^\dagger_1 \omega_1 + \mu^2_2 \omega^\dagger_2 \omega_2 - \mu^2_3 \left(\omega^\dagger_1 \omega_2 + \text{H.c.} \right) + \lambda_H (H^\dagger H)^2/2 \\ &+ \lambda_2 (\omega^\dagger_1 \omega_1)^2/2 + \lambda_3 (\omega^\dagger_2 \omega_2)^2/2 + \lambda_4 (H^\dagger H)(\omega^\dagger_1 \omega_1) \\ &+ \lambda_5 (H^\dagger H)(\omega^\dagger_2 \omega_2) + \lambda_6 (\omega^\dagger_1 \omega_1)(\omega^\dagger_2 \omega_2) + \lambda_7 (\omega^\dagger_1 \omega_2)(\omega^\dagger_2 \omega_1) ,\end{aligned} \tag{2.9}$$

with the same notation as the original work. BM establish the following CC:

$$y_t,\ f_1,\ f_2,\ \lambda_i(\mu) \to \infty , \quad \text{for}\ \mu \to \Lambda . \tag{2.10}$$

As BM mentioned, the aim of these new interactions is to reduce the predicted values for m_t and m_h, as they give positive contributions to $y_t(\mu)$ and $\lambda_H(\mu)$. They obtained the correct values, at their time of writing, of $m_h \sim m_t = 176\,\text{GeV}$ for $\Lambda = 10^{15}\,\text{GeV}$. BM pointed out that the reason for not including the term $\bar{Q}_{Li} b^i_R \bar{b}_{Rj} Q^j_L$ in Eq. (2.7) is because it would generate a Yukawa-type interaction like

$$\mathcal{L}_{EFT} \supset \bar{Q}_{Li} b^i_R \tilde{H} + \text{H.c.} , \tag{2.11}$$

which leads to a tree-level mass for the quark bottom, instead of being at 1-loop level and providing the desire natural hierarchy $m_b/m_t \ll 1$, see Fig. 2.3. In this manner two composite scalar, $\omega_{1,2}$, are needed in this set up for $m_b \neq 0$. The argument for not including the interaction in Eq. (2.11) is based on a Peccei-Quinn-type symmetry that is only softly violated by μ^2_3 in Eq. (2.9).

---

[3] Through out this thesis the Yukawa couplings will be named y or f.

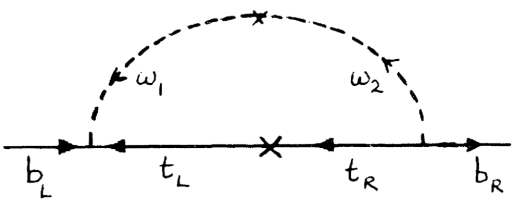

Figure 2.3: Diagram generating mass for the quark b at 1-loop level out of the top quark. Extracted from Ref. [104].

2.4 Infrared behaviour of the RGEs

The low-energy predictions for m_t and m_H may not depend on the details of the actual condensation mechanism at Λ, which is due to the infrared fixed point behavior of the RGEs. In this respect, when the scale Λ is larger than some minimal value $\Lambda_{inf\text{-}ref}$, predictions for the final masses are not sensitive to the following changes: (i) if the values of the Yukawa couplings $y_i(\Lambda)$ are varied in between some minimum number, y_{min}, and infinity or (ii) if the energy scale Λ is changed one order of magnitude. For example, in the BHL model, $\Lambda_{inf\text{-}ref} \approx 10^8\,\text{GeV}$ and the coupling $y_t^2(\Lambda)/4\pi$ can be freely varied in the range: $[1, \infty)$.

These features in the infrared fixed point behavior help the framework to overcome two theoretical subtleties. The first one was pointed out by Ref. [105] and is related to the use of the MS scheme for the RGEs, which is mass-independent. This would be reflected, for example in the BHL model, by the fact that in the limit $\mu \to \Lambda$ the ratio $m_H^2(\mu)/y_t^2(\mu) \neq 0$; whereas it is supposed to be zero given the non-dynamical nature of H. However, it has been emphasized that other schemes, which lack this difficulty, lead to minimal differences in the final predictions for $\Lambda > \Lambda_{inf\text{-}ref}$, in the case of BHL, see Ref. [22].

The second subtlety is related to the predictability of the framework being compromised if higher than $D = 6$ operators appear in the Lagrangian, at the scale Λ, see Refs. [106–109]. However, Refs. [110, 111] discussed the fact that the higher dimensional operators would have little impact in the low-energy theory, because of the suppression for large values of the scale Λ.

Chapter 3

Colored scalar composites

With the purpose of improving the BHL predictions on the top quark and Higgs boson masses (described in Sec. 1.3), and at the same time considering the simplest scenarios, we are driven to incorporate new colored scalar particles to the SM in the composite Higgs framework [1]. These scalars are considered as composite states of quarks with four-fermion interactions, which are different from the one in BHL (with non-trivial color structures). In Ch. 2 it is suggested that the predictions for m_t and m_h are sensitive to new physics at some higher energy scale, and that they tend to be larger than expected at the EW scale due to the compositeness conditions (defined in Sec. 1.3). In particular, the contributions from colored scalars to the RGEs act in favor of reducing the relevant couplings at lower energies, and therefore we analyze here their final effects. The election of the colored scalars is further motivated in Sec. 3.1 and a description of the implemented model takes place in Sec. 3.2. Results for m_t and m_h are shown in Sec. 3.3 and Sec. 3.4, respectively.

3.1 Colored bilinears in SM

The addition of a new particle to the SM is motivated by the fact that the SM alone is unable to reproduce the correct values of m_H and m_t in the BHL scheme as presented in Secs. 1.3 and 2.1. The simplest scenario could be a scalar field with the right interactions that lower the BHL predictions. Consequently we search for all the scalars that, in general, are able to couple to the SM fermions with the quantum numbers displayed in Tab. 1.1. In this manner, the following bilinears are possible out of the SM fermions, with charges ($SU(3)_c$,$SU(2)_L$,$U(1)_Y$), which would couple to the possible scalar fields:

$$\begin{aligned}
\overline{Q}u &\sim (1,2,1/2),\ (8,2,1/2)\\
\overline{Q}d &\sim (1,2,-1/2),(8,2,-1/2)\\
Q^cQ^c &\sim (3_a,1_a,-1/3),(3_a,3_s,-1/3),\\
& (\overline{6}_s,1_a,-1/3),(\overline{6}_s,3_s,-1/3)\\
u^cu^c &\sim (3_a,1,-4/3),(\overline{6}_s,1,-4/3)\\
d^cd^c &\sim (3_a,1,2/3),(\overline{6}_s,1,2/3)\\
u^cd^c &\sim (3_a,1,-1/3),(\overline{6}_s,1,-1/3)\\
\overline{Q}e &\sim (\overline{3},2,-7/6)\\
Q^cL^c &\sim (\overline{3},1,1/3),(\overline{3},3,1/3)\\
u^ce^c &\sim (\overline{3},1,1/3)\\
d^ce^c &\sim (\overline{3},1,4/3)\\
e^ce^c &\sim (1,1,2)\\
L^cL^c &\sim (1,1_a,1),(1,3_s,1)\,. \qquad (3.1)
\end{aligned}$$

These are all the possible scalars, in the composite framework, that can be included interacting with the SM through new Yukawa couplings.[1] From these bilinears, we will keep only those containing the top quark, in order to make sure the top Yukawa coupling is affected and the prediction for m_t is closer to the measured value. Hence the following bilinears are excluded: d^cd^c, d^ce^c, e^ce^c and L^cL^c; as well as the bilinears $\overline{Q}e$, u^ce^c and Q^cL^c because of their contributions to proton decay. Furthermore, the interactions which are anti-symmetric (e.g. one of the SU(3) or SU(2) anti-symmetric and the other symmetric) require at least two generations and could be addressed as the next simplest scenario. Ultimately, avoiding leptoquark interactions[2] for simplicity, we are left with:

$$\begin{aligned}
\overline{Q}u &\sim (1,2,1/2),(8,2,1/2)\\
\overline{Q}d &\sim (1,2,-1/2),(8,2,-1/2)\\
Q^cQ^c &\sim (3_a,1_a,-1/3),(\bar{6}_s,3_s,-1/3)\\
u^cu^c &\sim (\bar{6}_s,1,-4/3)\\
u^cd^c &\sim (3_a,1,-1/3),(\bar{6}_s,1,-1/3)\,. \qquad (3.2)
\end{aligned}$$

The scalar $(1,2,1/2)$ is the Higgs doublet. Notice that the field with quantum

---

[1] This set of bilinears can also be extended with vector couplings, although it is beyond the scope of this work.

[2] Mohapatra and Babu in Ref. [112] considered them in order to generate tau-lepton masses.

numbers $(3, 1, -1/3)$ (or its conjugate) can couple to a variety of bilinears: $Q^c Q^c$, $u^c d^c$, $Q^c L^c$ and $u^c e^c$.

For the sake of simplicity, in this chapter we finally consider as scalar fields, in addition to the SM Higgs boson: the colored triplet $\omega_t \sim (3, 1, -1/3)$, the colored sextet $\omega_s \sim (\bar{6}, 1, -4/3)$ and the colored octet fields $\omega_o \sim (8, 2, 1/2)$. The phenomenology associated to these colored scalar fields is analyzed in Sec. 3.3.

3.2 Bosonization of the colored triplet

In this section we illustrate the bosonization in the case of the colored triplet scalar from the four-fermion interaction:

$$\mathcal{L}_\Lambda = G\,\overline{Q}_{Li} t^i_R \bar{t}_{Rj} Q^j_L + G_t\,\overline{Q^c}_{iL} i\tau_2 Q_{jL}\left(\overline{Q^c}_{lL} i\tau_2 Q_{kL}\right)^\dagger \epsilon_{ijm}\epsilon^{klm}\,, \tag{3.3}$$

from which follows the Lagrangian:

$$\mathcal{L}_\Lambda = -m^2_{0H}|H|^2 - m^2_{0\omega}|\omega_t|^2 - \left(y_{0t}\overline{Q}_L t_R \tilde{H} + f_{0t}\overline{Q^c}_{iL} i\tau_2 Q_{jL}\,\omega_{t,k}\epsilon^{ijk} + \text{H.c.}\right)\,. \tag{3.4}$$

The equivalence of Eqs. (3.3) and (3.4) is easily checked by using the equations of motion and remove the scalar fields H and ω_t, giving $G = y^2_{0t}/m^2_{0H}$ and $G_t = f^2_{0t}/m^2_{0\omega}$. Renormalization leads to (at scales $\mu < \Lambda$), see Fig. 3.1:

$$\begin{aligned}\mathcal{L}_{EFT} = & Z_H|\partial H|^2 - \tilde{m}^2_H|H|^2 - \frac{1}{2}\tilde{\lambda}_H|H|^4 - \left(y_{0t}\overline{Q}_L t_R H + f_{0t}\overline{Q^c}_{iL} i\tau_2 Q_{jL}\omega_{t,k}\epsilon^{ijk} + \text{H.c.}\right) \\ & + Z_\omega|\partial\omega_t|^2 - \tilde{m}^2_\omega|\omega_t|^2 - \tilde{\lambda}_2|H|^2|\omega_t|^2 - \frac{1}{2}\tilde{\lambda}_3|\omega_t|^4\,,\end{aligned} \tag{3.5}$$

and in the QLA approach we obtain:

$$\begin{gathered} Z_\omega = \frac{8}{N_c} f^2_{0t} L\,, \quad \tilde{\lambda}_2 = \frac{16}{N_c} f^2_{0t} y^2_{0t} L, \quad \tilde{\lambda}_3 = \frac{8^2}{N_c} f^4_{0t} L\,, \\ \tilde{m}^2_\omega = m^2_{0\omega} - 2 f^2_{0t}\frac{8}{16\pi^2}\left(\Lambda^2 - \mu^2\right)\,, \quad L = N_c \log\bigl(\Lambda^2/\mu^2\bigr)/(16\pi^2)\,. \end{gathered} \tag{3.6}$$

After making the redefinitions $H \to H/\sqrt{Z_H}$ and $\omega_t \to \omega_t/\sqrt{Z_\omega}$, we get

$$\begin{aligned}\mathcal{L}_{EFT} = {} & |\partial H|^2 - m^2_H|H|^2 - \frac{1}{2}\lambda_H|H|^4 - \left(y_t\overline{Q}_L t_R H + f_t t^{\bar{c}}_R t_R \omega_t + \text{H.c.}\right) \\ & + |\partial\omega_t|^2 - m'^2_\omega|\omega_t|^2 - \lambda_2|H|^2|\omega_t|^2 - \frac{1}{2}\lambda_3|\omega_t|^4\,,\end{aligned} \tag{3.7}$$

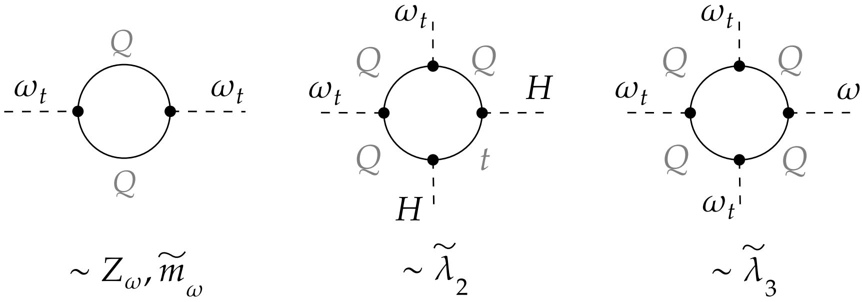

Figure 3.1: Diagrams contributing to the induced terms, Z_ω, $\tilde{m}_\omega$, $\tilde{\lambda}_2$ and $\tilde{\lambda}_3$, of the composite triplet scalar in the quark loop approximation.

so m_H^2, y_t^2 and λ_H are as in Sec. 1.3 and

$$m_\omega'^2 = \tilde{m}_\omega^2/Z_\omega\ , \quad f_t^2 = f_{0t}^2/Z_\omega = \frac{3}{8L}\ ,$$
$$\lambda_2 = \tilde{\lambda}_2/(Z_H Z_\omega) = \frac{2}{L} = 2y_t^2\ , \quad \lambda_3 = \tilde{\lambda}_3/Z_\omega^2 = \frac{3}{L} = 3y_t^2\ . \tag{3.8}$$

When the Higgs field gets its VEV, the coupling λ_2 gives a contribution to the physical colored scalar mass (we require $\langle\omega_t\rangle = 0$ so $SU(3)_c$ is preserved):

$$\begin{aligned} m_\omega^2 &= m_\omega'^2 + \lambda_2 \frac{1}{2} v_h^2 = m_\omega'^2 + y_t^2 v_h^2 = m_\omega'^2 + 2m_t^2 \\ &= 2m_t^2 + \left(\frac{2\pi^2 m_{0\omega}^2}{f_{0t}^2} - 2\Lambda^2\right) \frac{1}{\log\left(\Lambda^2/m_t^2\right)}\ , \end{aligned} \tag{3.9}$$

where in the last equality we took $\mu^2 = m_t^2 \ll \Lambda^2$, and substituted $m_\omega'^2$ from Eq. (3.8). As mentioned in Sec. 1.3, all the couplings are proportional to $1/L$ and therefore can be expressed in terms of the top quark mass. Moreover, it is clear that so far the predictions for m_t and m_h are exactly the same as in the BHL scenario, so the complete calculations are essential in the RGE approach, as we develop in the following.

3.3 The top quark mass

As discussed in Sec. 1.3, the precise prediction for m_t is obtained by considering the most general EFT, containing the new colored fields, and requiring to meet compositeness conditions at some high energy scale Λ. These requirements are the matching conditions across the threshold to the model of four-fermion interactions with no dynamical scalar fields.

In this chapter, we consider the same CCs as in Sec. 1.3; but with some modifications as follows. We require a continuous transition of the couplings from the EFT to the fermionic 1-loop scenario (as in the quark loop approximation scheme) at the scale $\Lambda_\kappa = \Lambda/\kappa$ (i.e. $\kappa > 1$). Examples of fermionic 1-loop couplings are shown in Eqs. (1.16), (1.17) and (1.18) of Sec. 1.3 for the BHL model and in Eq. (3.8) for the colored triplet scalar. In summary, we set as initial conditions the corresponding CCs of the fermionic 1-loop diagrams, and evolve the RGEs backwards from the scale Λ_κ, see e.g. Fig. 3.2. We will consider one colored scalar at a time, in order to account for their influence on the prediction for m_t independently. The new Yukawa-type interactions are:

$$\begin{aligned}
\mathcal{L}_Y^{tri} &= -f_t\, \overline{Q^c}_{iL} i\tau_2 Q_{jL}\omega_{t,k}\,\epsilon^{ijk} + \text{H.c.}\,, \\
\mathcal{L}_Y^{sxt} &= -f_s\, \overline{t^c_{Ri}} t_{Rj}\omega_s^{ij} + \text{H.c.}\,, \\
\mathcal{L}_Y^{oct} &= -f_o\, \overline{Q}_{Li} t_{Rj}\omega_o^{ij} + \text{H.c.}\,, \qquad (3.10)
\end{aligned}$$

where ω_t is the colored triplet $\sim (3, 1, -1/3)$, ω_s is the colored sextet $\sim (\bar{6}, 1, -4/3)$ and ω_o the colored octet $\sim (8, 2, 1/2)$. For simplicity, we have assumed only one generation of fermions, so the Yukawa couplings f_i can be made real in general, after the correct redefinition of the fields. The RGEs expressed in terms of the variables,

$$x = y_t^2\,, \quad y = f_i^2\,, \quad z = g_3^2\,, \quad t = \frac{1}{16\pi^2}\ln\frac{\mu}{m_Z}\,, \qquad (3.11)$$

are (without electroweak couplings)[3]

$$\begin{aligned}
\dot{x} &= x(a_{11}x + a_{12}y - c_1 z)\,, \qquad (3.12) \\
\dot{y} &= y(a_{21}x + a_{22}y - c_2 z)\,, \\
\dot{z} &= -bz^2\,,
\end{aligned}$$

with the coefficients a_{ij}, c_i and b for each scalar case shown in Tab. 3.1.

The final results for the top quark mass m_t are shown in Figs. 3.3 and 3.4, for each colored scalar separately, with a representative value of $\kappa = 2$. The CC employed here can be found in Tab. 3.2. The masses of the scalars are generally noted as M_ω, and their effect in the plots is the expected: a small M_ω allow for the top Yukawa coupling to evolve into smaller values. As is well known, the available data from the LHC allows for extensions in the SM scalar sector at the TeV scale, so this scale was taken as the lower bound on the colored scalar masses, $M_\omega \geq 1\,\text{TeV}$.

---

[3] Note that these equations are the full set of RGEs of the model considered before the decoupling of the colored scalar, taking place for energies above their masses M_ω.

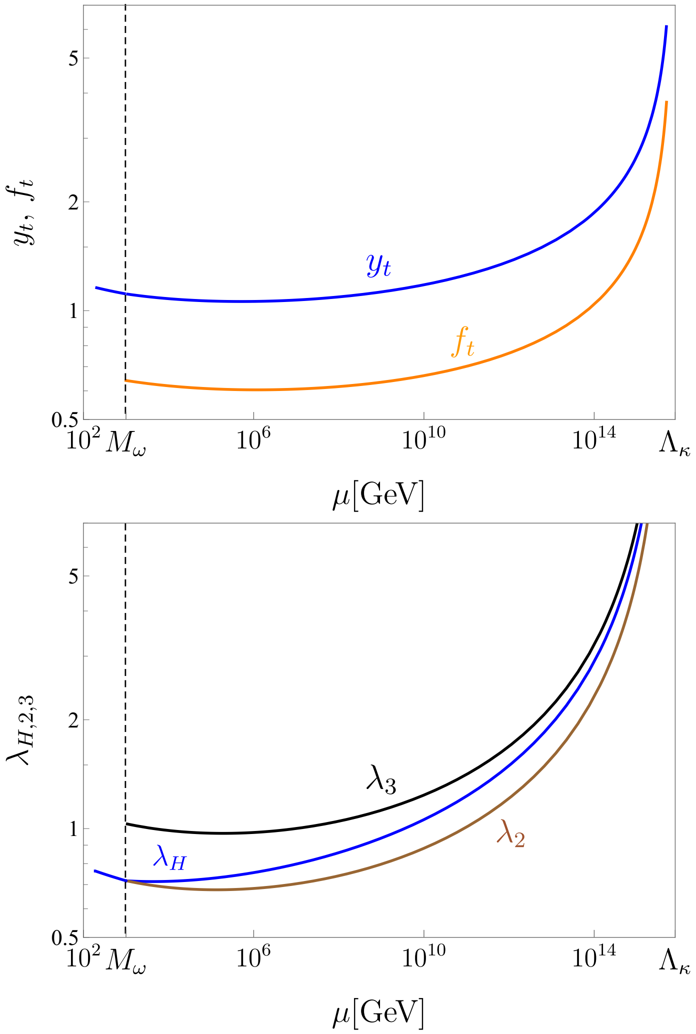

Figure 3.2: Evolution of the Yukawa (top panel) and quartic (bottom panel) couplings for an example value of $\Lambda = 10^{16}\,\text{GeV}$, $M_\omega = 10^3\,\text{GeV}$ and $\kappa = 2$ in the model with a colored triplet scalar. The blue and orange lines in the top panel correspond to the couplings y_t and f_t, respectively. The blue, brown and black lines in the bottom panel correspond to the couplings λ_H, λ_2 and λ_3, respectively.

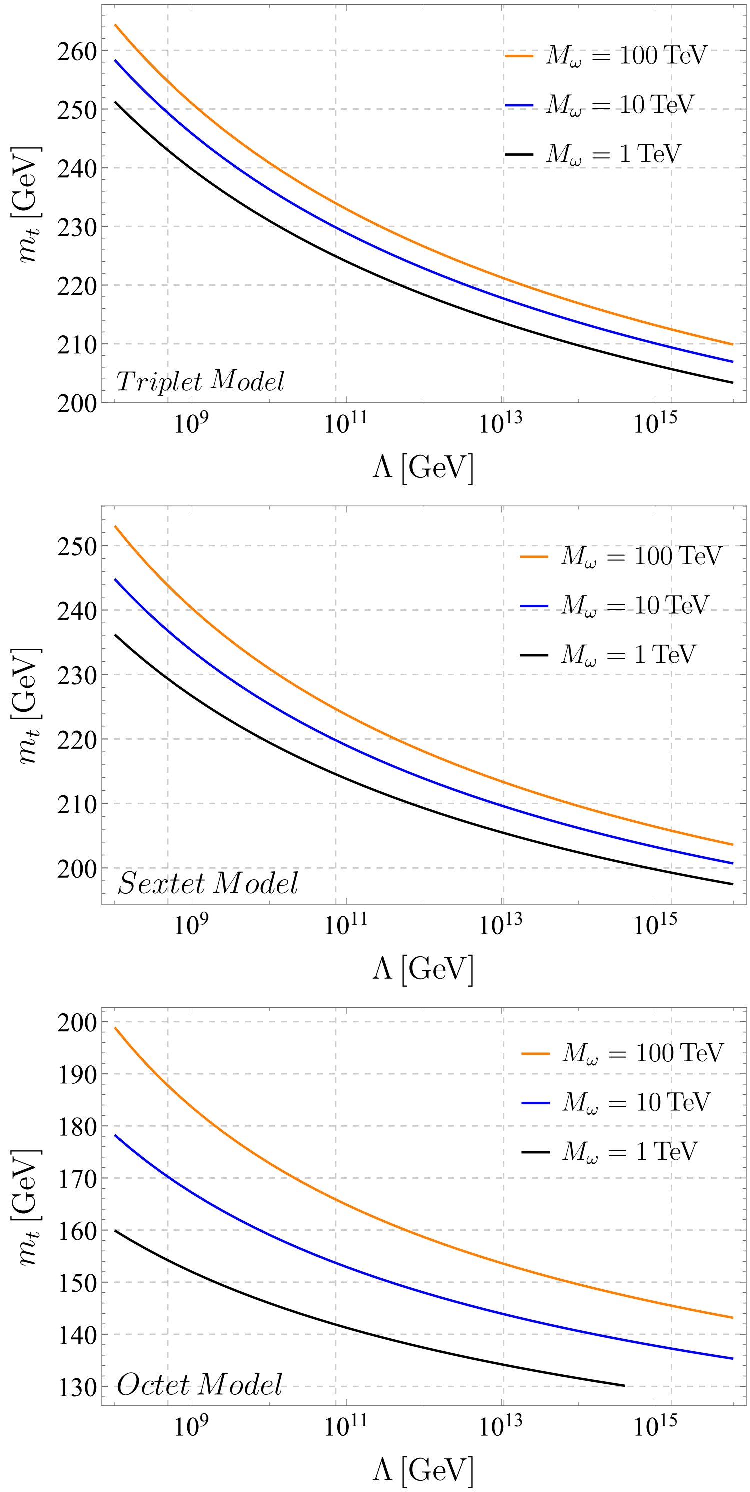

Figure 3.3: Results for the predictions of m_t from each scalar as a function of the scale Λ, with different values for the scalar masses M_ω and at fixed rate of $\Lambda/\Lambda_\kappa = 2$. The values of m_t were computed using Eq. (3.13), after evolving the Yukawa coupling untill the scale $\mu \equiv m_t$. The triplet, sextet and octet cases are shown from top to bottom.

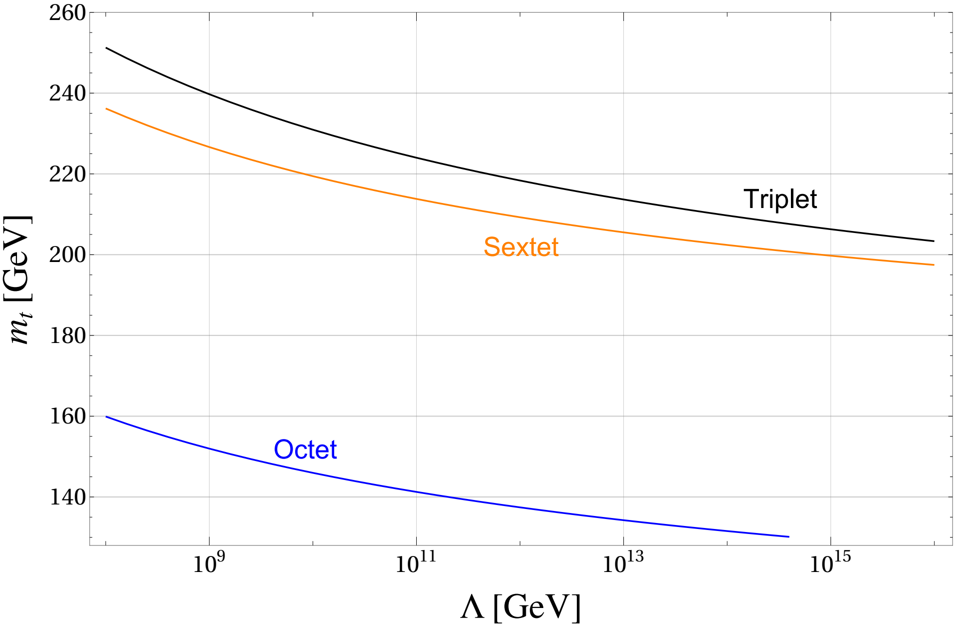

Figure 3.4: Comparative predictions of m_t from the three colored scalar fields as a function of the scale Λ. These results are obtained for a scalar mass $M_\omega = 1\,\text{TeV}$ and $\kappa = 2$. The values of m_t were computed using Eq. (3.13), after evolving the Yukawa coupling backwords untill the scale $\mu \equiv m_t$.

	a_{11}	a_{12}	a_{21}	a_{22}	c_1	c_2	b
SM	9	-	-	-	16	-	7
triplet	9	8	2	32	16	16	41/3
sextet	9	8	4	20	16	16	37/3
octet	9	8	3	10	16	16	10

Table 3.1: RGE coefficients of the Yukawa couplings, see Eq. (3.12), for the colored scalars considered.

	y_t^{-2}	f_i^{-2}	λ_H^{-1}	λ_2^{-1}	λ_3^{-1}	λ_4^{-1}
Triplet	L	$8L/N_c$	$L/2$	$L/2$	L/N_c	$-$
Sextet	L	$2L/N_c$	$L/2$	$L/4$	∞	$L/(2N_c)$

Table 3.2: Coupling values at the scale Λ_κ considered as CCs in the triplet and sextet scalar cases. They are obtained from the corresponding fermionic 1-loop diagrams.

The top quark Yukawa coupling $y_t(\mu)$ is evolved with the SM RGEs from the scale M_ω to $\mu = m_t$ (see Fig. 3.2), where m_t is defined by satisfying the SM relation:

$$y_t(m_t) = \sqrt{2}\frac{m_t}{v}\left(1+\delta_t\right) , \quad \text{with}\, \delta_t \approx -0.059 . \tag{3.13}$$

The SM corrections from the relation between the top quark pole mass and the Yukawa coupling [113, 114] is captured in δ_t, together with QCD and some small electroweak corrections.[4]

Regarding the comparison among the three scalars, the following points can be made. For the cases of the triplet and sextet scalars, the predictions are far larger than the expected value of $m_t = 172.76 \pm 0.30\,\text{GeV}$ [115], even when $\Lambda \approx 10^{19}\,\text{GeV}$, but still better than those of BHL. On the other hand, the colored octet yield results for m_t smaller than the observed value, even at the choice of $\Lambda = 10^7\,\text{GeV}$ at $M_\omega = 1\,\text{TeV}$.

The contrasts in the results obtained for m_t can be traced to the values of the parameter a_{22} in Eq. (3.12). For larger values of a_{22}, as for the triplet and sextet cases, the Yukawa coupling f_i decrease faster leaving y_t larger. Furthermore, the same hierarchy in m_t is foreseen from the differences in the infrared fixed points, obtained from Eq. (3.12) by setting $\dot{x} = \dot{y} = 0$ and fixing g_3 to the value at m_Z:

$$\left(a_{21} - a_{11}\frac{a_{22}}{a_{12}}\right) y_t^2 = \left(c_2 - c_1\frac{a_{22}}{a_{12}}\right) g_3^2 . \tag{3.14}$$

---

[4] When the values $m_t \approx 173\,\text{GeV}$ and $m_h \approx 125\,\text{GeV}$ are considered, δ_t can be well approximated by -0.059.

In this manner, in the SM the equilibrium point, at the EW scale, is at

$$y_t^2 = \frac{16}{9} g_3^2 \quad \rightarrow \quad m_t \approx 280\,\mathrm{GeV}\,. \tag{3.15}$$

While for the colored scalars they are at:

- Triplet:
$$y_t^2 = \frac{24}{17} g_3^2 \quad \rightarrow \quad m_t \approx 250\,\mathrm{GeV}\,, \tag{3.16}$$
- Sextet:
$$y_t^2 = \frac{48}{37} g_3^2 \quad \rightarrow \quad m_t \approx 240\,\mathrm{GeV}\,, \tag{3.17}$$
- Octet:
$$y_t^2 = \frac{16}{33} g_3^2 \quad \rightarrow \quad m_t \approx 150\,\mathrm{GeV}\,. \tag{3.18}$$

Colored octet: constraints

The colored octet $SU(2)_L$-doublet represents an interesting colored scalar field from the phenomenological point of view. In particular, it implements the principle of minimal flavor violation, leading to a natural suppression of flavor-changing neutral-currents, see Ref. [116].

Furthermore, it can modify the Higgs boson production, electroweak precision observables and the anomalous magnetic and electric dipole moments of quarks (for a review see Refs. [117, 118]), which makes it a promising candidate to be measured in the future.

With regard to its color nature, Miralles et al in Ref. [117] set bounds on the mass of the colored octet from its possible production, and subsequent decay to heavy quarks, at the LHC for $\sqrt{s} = 13\,\mathrm{TeV}$. The processes studied were $pp \to S^0 \to \bar{t}t$, $pp \to S^0\,\bar{t}t \to \bar{t}t\,t\bar{t}$ and $pp \to S^+\,\bar{t}b \to \bar{t}b\,\bar{t}b$, where S^0 and S^+ correspond to the neutral and charged components of ω_o, and p is the proton. Their results, in the charged case, the most stringent one, constrain the scalar masses to $M_\omega \geq 1\,\mathrm{TeV}$. This limit can be applied to the other colored scalars, which in principle should be heavier or more constrained.

3.4 The Higgs boson mass

In general, the RGE for the Higgs quartic coupling λ_H can be written as (i.e. omitting gauge couplings):

$$\frac{d\lambda_H}{dt} = 12\left(\lambda_H^2 + \lambda_H y_t^2 - y_t^4 + c_k \lambda_k^2\right) , \tag{3.19}$$

where λ_k are the couplings of operators having two Higgs bosons and two colored scalars. From Eq. (3.19), the evolution of $\lambda_H(\mu)$ depends on that of $\lambda_k(\mu)$, which is a function of all the possible quartic couplings in the EFT model; consequently, the evolution of $\lambda_H(\mu)$ is directly or indirectly connected to all of quartic coupling's evolution. Due to this, determining all the quartic couplings possible at each scenario is desirable. In the colored triplet ω_t, which is the easiest case, there is one single invariant of the forms $H^2\omega_t^2$ and ω_t^4 (as in Eq. (3.5)):

$$V_t = \frac{1}{2}\lambda_H|H|^4 + \lambda_2|H|^2|\omega_t|^2 + \frac{1}{2}\lambda_3|\omega_t|^4 . \tag{3.20}$$

However, we have a more complex scenario in the sextet with two independent quartic couplings in ω_s:

$$V_s = \frac{1}{2}\lambda_H|H|^4 + \lambda_2|H|^2 Tr\left[\omega_s^\dagger\omega_s\right] + \frac{1}{2}\lambda_3\left(Tr\left[\omega_s^\dagger\omega_s\right]\right)^2 + \frac{1}{2}\lambda_4 Tr\left[\left(\omega_s^\dagger\omega_s\right)^2\right] \tag{3.21}$$

Furthermore, in the colored octet the number of independent quartic couplings raises to twelve:

$$\begin{aligned} V_o =& \frac{1}{2}\lambda_H\left(H^{\dagger i}H_i\right)^2 + \lambda_1\left(H^{\dagger i}H_i\right) Tr\left[\omega_o^{\dagger j}\omega_{oj}\right] + \lambda_2\left(H^{\dagger i}H_j\right) Tr\left[\omega_o^{\dagger j}\omega_{oi}\right] \\ &+ \left(\lambda_3\left(H^{\dagger i}H^{\dagger j}\right) Tr\left[\omega_{oi}\omega_{oj}\right] + \lambda_4 H^{\dagger i} Tr\left[\omega_o^{\dagger j}\omega_{oj}\omega_{oi}\right] + \lambda_5 H^{\dagger i} Tr\left[\omega_o^{\dagger j}\omega_{oi}\omega_{oj}\right] + \text{H.c.}\right) \\ &+ \frac{1}{2}\lambda_6 Tr\left[\omega_o^{\dagger i}\omega_{oi}\omega_o^{\dagger j}\omega_{oj}\right] + \frac{1}{2}\lambda_7 Tr\left[\omega_o^{\dagger i}\omega_{oj}\omega_o^{\dagger j}\omega_{oi}\right] + \frac{1}{2}\lambda_8 Tr\left[\omega_o^{\dagger i}\omega_{oi}\right] Tr\left[\omega_o^{\dagger j}\omega_{oj}\right] \\ &+ \frac{1}{2}\lambda_9 Tr\left[\omega_o^{\dagger i}\omega_{oj}\right] Tr\left[\omega_o^{\dagger j}\omega_{oi}\right] + \frac{1}{2}\lambda_{10} Tr\left[\omega_{oi}\omega_{oj}\omega_o^{\dagger i}\omega_o^{\dagger j}\right] + \frac{1}{2}\lambda_{11} Tr\left[\omega_{oi}\omega_{oj}\omega_o^{\dagger j}\omega_o^{\dagger i}\right] , \end{aligned} \tag{3.22}$$

where i and j are $SU(2)_L$ indices and the trace is taken over $SU(3)_c$ indices.

The increase in the number of couplings in the potential for the sextet and octet cases, leads to a more complex scenario with the following obstacle. Some of the quartic couplings, say λ_i, are not generated with fermionic 1-loop diagrams, resulting in the matching: $\lambda_i(\Lambda_\kappa) \equiv 0$. Furthermore their corresponding RGEs will lack the contributions in the form f_i^4, y_t^4 or $f_i^2 y_t^2$ which, because of carrying minus sign, help the λ_i not to become negative; and as a result the stability of the potential is not compromised.[5] For example, the coupling λ_3 in the colored sextet case displays this mentioned character, see Tab. 3.2

The prediction of m_h is obtained from $\lambda_H(m_t)$ through the following expression:

$$m_h^2 = \frac{\lambda_H(m_t) v_h^2}{1+\delta_h}\,, \quad \delta_h \sim -0.011\,, \tag{3.23}$$

The connection between m_h and $\lambda_H(m_t)$ is obtained by taking into account the well known 1-loop SM corrections at the scale m_t [120], δ_h. The value $\delta_h = -0.011$ is a good approximation for current measured values of m_t and m_h, even though it depends on the masses of the other SM particles too.

The measured value of $m_h = 125.25 \pm 0.17\,\text{GeV}$ [115] was not obtained in the colored triplet case, giving as results $m_h = c\,m_t$, with $c \in [1.05, 1.10]$ in the best possible scenario of $\Lambda = 10^{16}\,\text{GeV}$. In order to obtain predictions of m_h with the colored sextet, with some $\lambda_i(\Lambda_\kappa) = 0$, we opt to decouple the colored scalar just before the stability is jeopardized. In this manner, the results for the sextet are shown in Fig. 3.5, and unfortunately the values of M_ω had to be extremely enhanced, leading to $m_{t,h}$ too large. The predictions for m_h in the octet scenario are developed elsewhere.

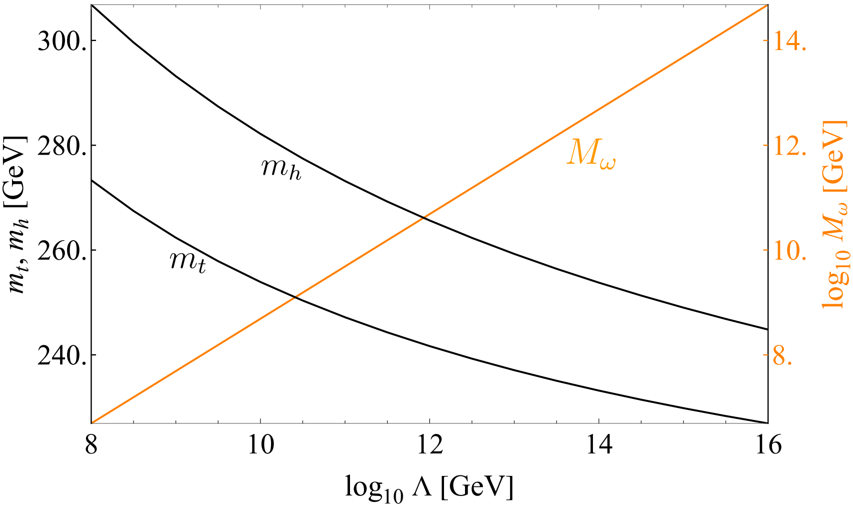

Figure 3.5: Results for the predictions of $m_{t,h}$ (left axis) as a function of Λ and at a fixed rate $\Lambda/\Lambda_\kappa = 10$, considered with the SM plus a colored sextet. The right axis displays the minimum values taken for M_ω leading to an effective potential bounded from below.

---

[5] Conditions on the quartic couplings allowing stability of the vacuum were taken from Refs. [119] and [118] for ω_s and ω_o, respectively.

Vector field analysis

Here, we present a vector field analysis in the colored triplet, neglecting the effect of electroweak contributions. The RGEs for the Yukawa couplings y_t and f_t with the colored triplet are

$$\begin{cases} 16\pi^2\beta_{y_t} = (9/2)y_t^3 + 4y_t f_t^2 - 8g_3^2 y_t \\ 16\pi^2\beta_{f_t} = 16 f_t^3 + f_t y_t^2 - 8g_3^2 f_t \,. \end{cases}$$

Considering $g_3 = 0$, the only equilibrium point is the origin, $(0,0)$ in notation (y_t, f_t), and it is an attractor point in the infrared, see Fig. 3.6 (top panel). However, when $g_3 \neq 0$ there are other equilibrium points, from which only one has $y_t \neq 0$ and $f_t \neq 0$ and it is the only attractor point, see Fig 3.6 (bottom panel). This explains the infrared behavior of $y_t(\mu)$, see Sec. 2.1 and 2.4, as from a huge range of initial conditions the final values are all close to a number larger than 1, resulting in an undesirably large prediction for m_t.

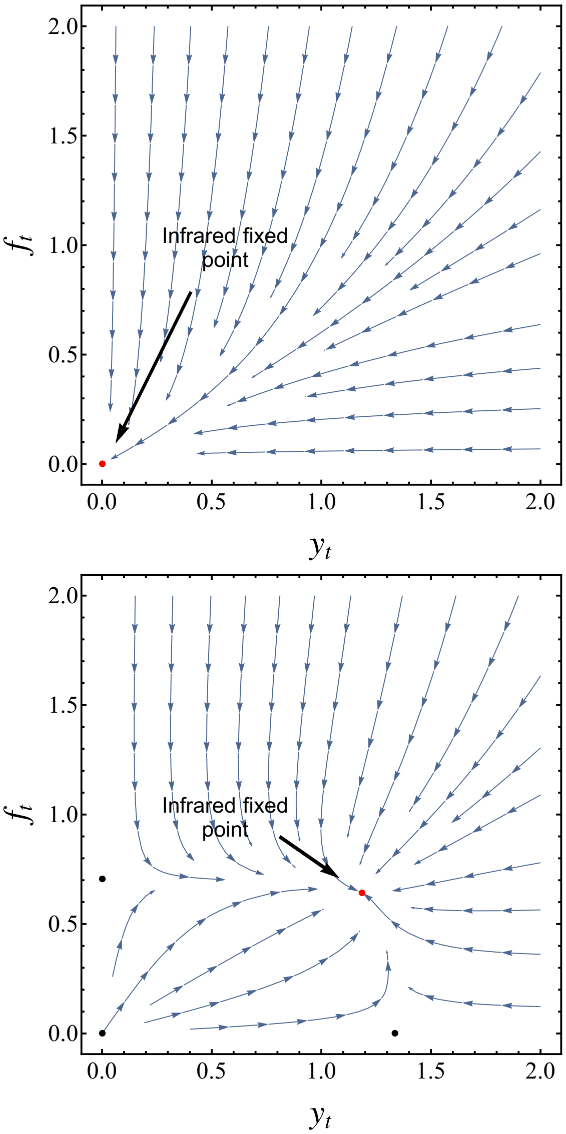

Figure 3.6: Vector fields of the model with a colored triplet scalar. The black dots are the equilibrium points, except for the attractor points being in color red, and the arrows are the flux lines for the Yukawa couplings y_t and f_t, with fixed $g_3 = 0$ (top panel) and $g_3 = 1$ (bottom panel).

Chapter 4

The inverse seesaw with composite scalars

In this chapter, we consider a scenario in the composite Higgs theory framework, see Sec. 1.3, where we assume the non-existence of fundamental scalars in Nature and four-fermion interactions able to generate composite states as in the BHL model. Among the appealing features of this framework are the binding of the dynamical generation of the top quark mass and the dynamical EWSB.

The models reviewed in Ch. 2 are not satisfying in many aspects. Some of them do not predict correctly the top quark and Higgs boson masses at the same time (like BHL or Martin's); while the best scenario, HK, has an important theoretical issue that we address below.

Here we propose an improvement of Martin's model, see Sec. 2.2, having the following differences with the HK model, see Ref. [2]. First, instead of increasing the number of neutrino families in the seesaw type I, we will lower the possible right-handed neutrino Majorana mass by implementing, naturally, the composite scheme within the ISS mechanism[1]. Second, in order to obtain the correct Higgs boson mass, we will include a new scalar singlet that, unlike in HK model, is a composite state made of the new fermions required in the ISS.

In Sec. 4.1, we introduce the model implementing the ISS mechanism in the composite framework, and, in Sec. 4.2, we describe the details in the computation of

---

[1] In Ref. [121], there is a implementation of the type of low-scale seesaw models to explain small neutrino masses in a composite scalar setting. However, the Higgs boson doublet is considered to be a fundamental field and no attempt was made in order to understand the observed masses of the Higgs boson and top quark. Other models of right-handed neutrino condensates can be found in Refs. [122–124]. On the other hand, in Ref. [125] it was shown that the ISS mechanism is the most natural way to implement neutrino masses in the Littlest Higgs model with T-parity.

m_t and m_h, including the CCs considered, and present their final predictions.

4.1 Merging the ISS in the composite scheme

In this section, we are embedding the ISS mechanism, Sec. 1.4.2, into the composite scheme. Specifically the ISS mechanism is going to be generated through the SSB of an extra composite singlet scalar at some low energy scale. The associated VEV, together with a Higgs portal type of interaction, will be responsible for the mechanism to account for the Higgs boson mass. Moreover, the masses of the new neutral heavy fermions could be naturally closer to the EW scale. This is an advantage in this model, where the new next physical scale does not need to be far from the EW scale.

The simplest implementation of the ISS mechanism is obtained by the addition to the SM of two chiral fermion singlets: N_R and χ_L. The Lagrangian at the scale Λ with four-fermion interactions and Majorana mass terms, μ_ν and μ_χ, is [2]

$$\begin{aligned}\mathcal{L} = \mathcal{L}_{SM\not{H}} &+ \frac{h_N^2}{m_{0H}^2}\left(\overline{L}_L N_R\right)\left(\overline{N}_R L_L\right) + \frac{h_s^2}{m_{0H}^2}\left(\overline{\chi}_L N_R\right)\left(\overline{N}_R \chi_L\right) \\ &+ \left(\frac{h_{t\nu}^2}{m_{0H}^2}\left(\overline{L}_L N_R\right)\left(\overline{t}_R Q_L\right) - \frac{1}{2}\overline{\chi_L^c}\mu_\chi \chi_L - \frac{1}{2}\overline{N_R^c}\mu_\nu N_R - \overline{\chi}_L M_{\chi\nu} N_R + \text{H.c.}\right). \qquad (4.1)\end{aligned}$$

Notice that the Lagrangian has two global phase symmetries if $\mu_\chi = \mu_\nu = M_{\chi\nu} = 0$. These phase symmetries could be defined as

- ∘ $U(1)_L:\ N_R \to e^{i\alpha} N_R\,,\ L_L \to e^{i\alpha} L_L\,,$
- ∘ $U(1)_\chi:\ \chi_L \to e^{i\beta} \chi_L\,,$

where the first would be the *lepton number symmetry.* When μ_χ and/or μ_ν are made different from zero, while $M_{\chi\nu} = 0$, there is one of the following symmetry breaking patterns: $\mu_\chi \neq 0$ and/or $\mu_\nu \neq 0$ then $U(1)_\chi$ and/or $U(1)_L$ are/is broken. However, if only $M_{\chi\nu} \neq 0$, there is a remaining global $U(1)$ symmetry defined by setting $\alpha = \beta$. In the analysis developed in this chapter we will set $\mu_\nu = M_{\chi\nu} = 0$ and focus on the explicit symmetry breaking of the $U(1)_\chi$ symmetry, $\mu_\chi \neq 0$, and on the SSB of $U(1)_L$. The reason will be clear in the following.

After bosonization, the Lagrangian can be expressed (in the limit in which $h_N \gg$

---

[2] For simplicity we assume only one generation of N_R and χ_L, but the mechanism can be generalized easily to three generations a la HK. Moreover, the generation of other quarks and leptons masses needs additional four-fermion interactions, which are neglected here.

$h_{t\nu}$) as,

$$\begin{aligned}\mathcal{L}_\Lambda =& \mathcal{L}_{SM\not{H}} - m_{0H}^2 H^\dagger H - y_{0t}\overline{Q}_L t_R \tilde{H} - y_{0\nu}\overline{L}_L N_R \tilde{H}\,,\\ &- m_{0S}^2 S^\dagger S + y_{0s} S\overline{N}_R \chi_L - \frac{1}{2}\overline{\chi_L^c}\mu_\chi \chi_L + \text{H.c.}\,,\end{aligned} \tag{4.2}$$

where S is the extra singlet scalar field, which is interpreted as a $\bar{\chi}_L N_R$ bound state, while H is a composite state of $\bar{L}_L N_R$ and $\overline{Q}_L t_R$. Fermion loops will induce a scalar potential and kinetic terms as in BHL, Sec. 2.1,

$$\begin{aligned}\mathcal{L}_{EFT} =& Z_H(\mu)|D_\mu H|^2 - \tilde{m}_H^2(\mu)|H|^2 + Z_S(\mu)|\partial_\mu S|^2 - \tilde{m}_S^2(\mu)|S|^2\\ &- \frac{1}{2}\tilde{\lambda}_H(\mu)|H|^4 - \frac{1}{2}\tilde{\lambda}_S(\mu)|S|^4 - \frac{1}{2}\tilde{\lambda}_{HS}(\mu)|H|^2|S|^2\\ &- \left(\tilde{y}_t(\mu)\overline{Q}_L t_R H + \tilde{y}_\nu(\mu)\overline{L}_L N_R H + \tilde{y}_s(\mu) S\overline{N}_R \chi_L + \frac{1}{2}\overline{\chi_L^c}\mu_\chi \chi_L + \text{H.c.}\right)\,.\end{aligned} \tag{4.3}$$

Calculation of the corresponding fermion loops and the CCs gives,

$$\begin{gathered}Z_H(\Lambda) = Z_S(\Lambda) = 0\,, \quad \tilde{\lambda}_H(\Lambda) = \tilde{\lambda}_S(\Lambda) = \tilde{\lambda}_{HS}(\Lambda) = 0\,,\\ \tilde{m}_H^2(\Lambda) = m_{0H}^2\,,\ \tilde{m}_S^2(\Lambda) = m_{0S}^2\,,\ \tilde{y}_t(\Lambda) = y_{0t}\,,\ \tilde{y}_\nu(\Lambda) = y_{0\nu}\,,\ \tilde{y}_s(\Lambda) = y_{0s}\,,\end{gathered} \tag{4.4}$$

and

$$\begin{gathered}Z_H(\mu) = \left(y_{0\nu}^2 + N_c y_{0t}^2\right) L(\mu)\,, \quad Z_S(\mu) = y_{0s}^2 L(\mu)\,,\\ \tilde{\lambda}_H(\mu) = \left(2y_{0\nu}^4 + 2N_c y_{0t}^4\right) L(\mu)\,, \quad \tilde{\lambda}_S(\mu) = 2y_{0s}^4 L(\mu)\,, \quad \tilde{\lambda}_{HS}(\mu) = 2y_{0\nu}^2 y_{0s}^2 L(\mu)\,,\\ \tilde{m}_H^2(\mu) = m_{0H}^2 - \left(2y_{0\nu}^2 + 2N_c y_{0t}^2\right)\frac{1}{16\pi^2}\left(\Lambda^2 - \mu^2\right)\,, \quad \tilde{m}_S^2(\mu) = m_{0S}^2 - \frac{y_{0s}^2}{8\pi^2}\left(\Lambda^2 - \mu^2\right)\\ L = \log\!\left(\Lambda^2/\mu^2\right)/(16\pi^2)\,.\end{gathered} \tag{4.5}$$

Rescaling the scalar fields as $H \to H/\sqrt{Z_H(\mu)}$ and $S \to S/\sqrt{Z_S(\mu)}$ we obtain

$$\begin{aligned}\mathcal{L}_{EFT} =& |D_\mu H|^2 - m_H^2(\mu)|H|^2 + |\partial_\mu S|^2 - m_S^2(\mu)|S|^2\\ &- \frac{1}{2}\lambda_H(\mu)|H|^4 - \frac{1}{2}\lambda_S(\mu)|S|^4 - \frac{1}{2}\lambda_{HS}(\mu)|H|^2|S|^2 +\\ &- \left(y_t(\mu)\overline{Q}_L t_R H + y_\nu(\mu)\overline{L}_L N_R H + y_s(\mu) S\overline{N}_R \chi_L + \frac{1}{2}\overline{\chi_L^c}\mu_\chi \chi_L + \text{H.c.}\right)\,,\end{aligned} \tag{4.6}$$

with

$$m_H^2(\mu) = \tilde{m}_H^2(\mu)/Z_H(\mu)\,, \quad m_S^2(\mu) = \tilde{m}_S^2(\mu)/Z_S(\mu)\,, \quad y_s^2(\mu) = y_{0s}^2/Z_S(\mu) = \frac{1}{L(\mu)}\,,$$

$$y_t^2(\mu) = y_{0t}^2/Z_H(\mu) = \frac{p^2}{(1+N_c p^2)\,L(\mu)}\,,\, y_\nu^2(\mu) = y_{0\nu}^2/Z_H(\mu) = \frac{1}{(1+N_c p^2)\,L(\mu)}\,,$$

$$\lambda_H(\mu) = \tilde{\lambda}_H(\mu)/Z_H^2(\mu) = \frac{2\left(1+N_c p^4\right)}{(1+N_c p^2)^2\,L(\mu)}\,,\, \lambda_S(\mu) = \tilde{\lambda}_S(\mu)/Z_S^2(\mu) = \frac{2}{L(\mu)}\,,$$

$$\lambda_{HS}(\mu) = \tilde{\lambda}_{HS}(\mu)/(Z_H(\mu)Z_S(\mu)) = \frac{2}{(1+N_c p^2)\,L(\mu)}\,, \tag{4.7}$$

where we define $p \equiv y_{0t}/y_{0\nu}$, which characterizes the relative strength of the top quark to neutrino interactions, and must be small, in order for H to be mostly a quark composite.

As mentioned before, when the two scalar fields develop VEVs,[3] the model in Eq. (4.6) implements the ISS mechanism, see Sec. 1.4.2, with the mass matrix $M_{\chi N}^{ij} = y_s^{ij}\,\langle S\rangle$. If the hierarchy $\mu_\chi \ll \langle H\rangle \ll \langle S\rangle$ is chosen the small neutrino masses can be explained. The following hierarchy of particle masses is given: $m_\nu \approx \mu_\chi\langle H\rangle^2/\langle S\rangle^2 \ll m_t, m_h \propto \langle H\rangle \ll M \approx m_s,\, m_{N_H} \propto \langle S\rangle \ll \Lambda$. The parameter M refers to the approximate scale of new particles: the masses of the scalar m_s and the neutral heavy lepton m_{N_H}.

On the other hand, the VEVs also allow for a mixing between the CP-even scalar components. Hence, the effective low-energy Higgs quartic coupling, λ, will be small even if the quartic couplings in the complete theory are large (i.e. what usually happens in the composite scenarios).

Notice that since the Lagrangian has an extra global symmetry, $U(1)_L$, broken spontaneously, the low energy spectrum contains a Goldstone boson coupled mainly to the neutral particles. This Goldstone boson would be a kind of singlet Majoron[4], see Ref. [128]. The phenomenological effects related to this special scalar are of large importance for the modification of the Higgs physics (e.g. Higgs boson invisible decay). These effects will be addressed in detail in Ch. 6.

For the rest of this chapter we will focus only on obtaining the top quark and Higgs boson masses in this composite scenario.

---

[3] We assumed the parameters of the model are such that both scalars develop VEVs, i.e. $m_H^2(M) < 0$ and $m_S^2(M) < 0$.

[4] Doublet and triplet Majorons [126, 127] are considered to be excluded because of constraints in the invisible decay width of the Z boson.

4.2 Predictions for top quark and Higgs boson masses

As mentioned, the theory at the scale Λ should match the EFT at low energy scales, with composite scalar fields, where the predictions for the masses m_t and m_h take place. Specifically, the matching occurs at a slightly lower scale than Λ, defined through a new parameter $\kappa > 1$:

$$\Lambda_\kappa = \frac{\Lambda}{\kappa} \,. \tag{4.8}$$

The compositeness conditions can be seen from Eq. (4.7), and for example in y_t and λ_H read:

$$y_t^2(\Lambda_\kappa) = \frac{p^2}{1+N_c p^2}\frac{16\pi^2}{\log(\kappa)} \,, \quad \lambda_H(\Lambda_\kappa) = \frac{2(1+N_c p^4)}{(1+N_c p^2)^2}\frac{16\pi^2}{\log(\kappa)} \,. \tag{4.9}$$

The compositeness conditions give us the values of all the Yukawa couplings, y_t, y_ν and y_s, and quartic couplings λ_H, λ_S and λ_{HS}, as functions of κ and p at the scale Λ_κ. Along this line, we then evolve the couplings with the RGEs of the complete model, see App. A, down to the scale M, which is fixed at some value above the EW scale. When $\langle S\rangle \neq 0$ the fermions N_R and χ_L combine to form a Dirac fermion (if $\mu_\chi = 0$, if $\mu_\chi \neq 0$ a pseudo-Dirac fermion) of mass $m_{N_H} \approx y_s(M)\langle S\rangle \approx M$. In this manner, at an approximate energy M, both heavy new particles decouple and the subsequent evolution occurs with the SM particles alone.

Therefore the top quark Yukawa coupling $y_t(\mu)$ is evolved with the SM RGEs from the scale M to $\mu = m_t$, where m_t is defined as in Eq. (3.13).[5]

In Fig. 4.1 we show an example of evolution of all Yukawa couplings for the values $p = 0.1$, $\Lambda = 10^{17}\,\text{GeV}$, $\kappa = 2$ and $M = 10\,\text{TeV}$, selected to reproduce the correct value of $m_t \approx 173\,\text{GeV}$. The function $y_t(\mu)$ is represented with the dashed or solid blue lines, depending on whether the new heavy particles are decoupled or not, respectively. Above the scale Λ_κ, all Yukawa couplings evolve only with the fermion loops (dotted line), diverging in the Landau pole at $\mu = \Lambda$. Moreover, notice that the Yukawa couplings y_ν and y_s drag y_t towards the Landau pole.

Previous to the calculation of the Higgs boson mass, it is necessary to analyze the consequences for the two scalars to obtain VEVs. We can parametrize them as

$$H^{(0)} = \frac{1}{\sqrt{2}}\left(v_h + h + i\omega^{(0)}\right) \,, \quad S = \frac{1}{\sqrt{2}}\left(u + s + i\theta\right) \,. \tag{4.10}$$

---

[5] The evolution of the gauge couplings is computed with the 1-loop SM RGEs, taking as initial conditions at m_Z their well known values. The new particles, being gauge singlets, do not affect the RGEs at 1-loop level.

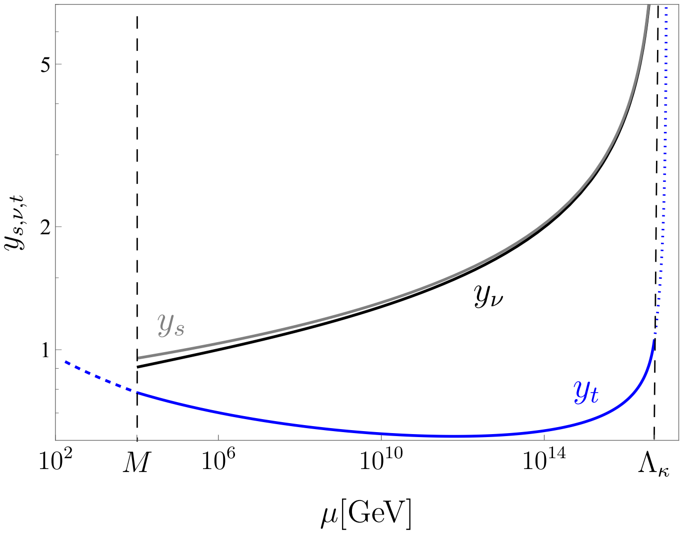

Figure 4.1: Evolution of the Yukawa couplings, as explained in the text, for $p = 0.1$, $\Lambda = 10^{17}\,\mathrm{GeV}$ and $\kappa = 2$. The new heavy particles are assumed to have a mass $M = 10\,\mathrm{TeV}$, scale at which they decouple. From M to the EW scale, the top Yukawa coupling y_t is evolved according to the SM RGE. For the chosen parameters, the prediction is $m_t = 173\,\mathrm{GeV}$.

The already mentioned appearance of the Goldstone boson at low energies (below $\mu = M$), is represented by the imaginary part of S, θ. While the real part mixes with the CP-even component of the Higgs field h, with a mass matrix squared given as

$$M^2_{\text{scalars}} = \begin{pmatrix} \lambda_H v_h^2 & \lambda_{HS}\, v_h u \\ \lambda_{HS}\, v_h u & \lambda_S u^2 \end{pmatrix} , \quad v_h \equiv \sqrt{2}\,\langle H \rangle \ , \quad u \equiv \sqrt{2}\,\langle S \rangle \ , \tag{4.11}$$

in the (h, s) basis. We identify the observed Higgs boson with the mass eigenstate having the smallest eigenvalue, m_h^2, while the largest, m_s^2, is assigned for a new scalar (for $u \gg v_h$, $m_s^2 \sim \lambda_S u^2$). In the limit $m_s \gg v_h$ the Higgs boson mass is:

$$\begin{aligned} m_h^2 &= v_h^2 \left(\lambda_H - \frac{\lambda_{HS}^2}{\lambda_S} \right) \frac{1 - \lambda_H v_h^2 / m_s^2}{1 - \left(\lambda_H - \lambda_{HS}^2/\lambda_S \right) v_h^2/m_s^2} \xrightarrow{m_s \gg v_h} \\ &\xrightarrow{m_s \gg v_h} v_h^2 \left(\lambda_H - \frac{\lambda_{HS}^2}{\lambda_S} \right) \left(1 - \frac{\lambda_{HS}^2}{\lambda_S} \frac{v_h^2}{m_s^2} + \cdots \right) . \end{aligned} \tag{4.12}$$

In this manner an important feature occurs when $m_s \gg v_h$: the effective SM quartic coupling, λ, is a redefinition of the quartic couplings of the complete theory,[6]

$$\lambda(M) = \left(\lambda_H(M) - \frac{\lambda_{HS}^2(M)}{\lambda_S(M)}\right) . \tag{4.13}$$

It is worth noticing that from the CC of Eq. (4.7), a cancellation naturally takes place in Eq. (4.13) for $p \ll 1$, which helps making the effective quartic coupling λ small, even if the composite scheme requires large values of quartic couplings. This quality is the expected in order to reconcile the results for the Higgs boson mass with the observed value. The prediction for m_h is obtained from $\lambda(m_t)$ through the expression

$$m_h^2 = \lambda(m_t) v_h^2 \frac{1+\delta_{hs}}{1+\delta_h} , \quad \delta_h \sim -0.011 . \tag{4.14}$$

The connection between m_h and $\lambda(m_t)$ is carried by taking into account the well known 1-loop SM corrections at the scale m_t, see δ_h in Eq. (4.14), and the tree-level correction, δ_{hs}, estimated for $m_s \ll v_h$ from comparing the first line in Eq. (4.12) with Eq. (4.14) when 1-loop corrections are taken to zero (i.e. $\delta_h = 0$ and $\lambda(m_t) = \lambda(M)$),

$$\delta_{hs} \simeq -\frac{\lambda_{HS}^2(M)}{\lambda_S(M)} \frac{v_h^2}{m_s^2} \left(1 - \left(\lambda_H(M) - \frac{\lambda_{HS}^2(M)}{\lambda_S(M)}\right) \frac{v_h^2}{m_s^2}\right)^{-1} . \tag{4.15}$$

The previous expressions depend on the values taken by $\lambda_{H,S,HS}$ at the scale M and λ at m_t. These are obtained by evolving the corresponding RGEs, see App. A. In Fig. 4.2 there is an example with the same values of p, M, Λ and κ as in Fig. 4.1. From M until the EW scale, the evolution is given by the SM RGEs with the effective coupling λ. This procedure yielded, for the already mentioned parameters, $m_h = 125\,\text{GeV}$.

We repeated the procedures mentioned before for different values of (p,Λ) [and (κ,M)] and verified whether they are able to reproduce the expected values of $m_t \approx 173\,\text{GeV}$ and $m_h \approx 125\,\text{GeV}$. In Fig. 4.3 we depict the region of (p, Λ) that can reproduce the values of m_t (band with green-pink colors) and m_h (gray band) in an interval of 1 GeV around the measured values. We have considered at each plot two values of κ, while $M = 1\,\text{TeV}$ on the r.h.s. and $M = 10^3\,\text{TeV}$ on the l.h.s. Finally, there is, fortunately, an overlapping region where both masses are reproduced. For $M = 1\,\text{TeV}$ this is found around $\Lambda \sim 10^{19}\,\text{GeV}$, while for $M = 10^3\,\text{TeV}$ around

---

[6] We perform the matching at a scale M, approximating it to be of the same order as the masses of the heavy new fermion and scalar. Since for $u \gg v_h$, $m_{N_H} \sim y_s u/\sqrt{2}$ and $m_s^2 \sim \lambda_S u^2$, one needs λ_S and y_s^2 to be of the same order. This is motivated by the compositeness conditions. Specifically, we have simplified the computations by considering $M = m_s$.

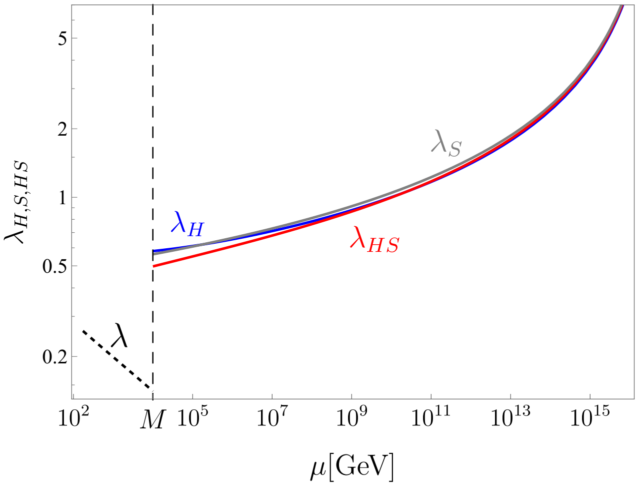

Figure 4.2: Evolution of the scalar quartic couplings, as explained in the text, for the same values as in Fig. 4.1. At the scale $M = 10\,\text{TeV}$ the new particles decouple, leaving a SM quartic coupling, as in Eq. (4.13), which runs down to the EW scale according to the SM RGE. For these parameters the correct mass $m_h = 125\,\text{GeV}$ was obtained.

$\Lambda \sim 10^{12}\,\text{GeV}$. Larger values of M lead to lower desirable values of Λ, however at $M \gtrsim 10^8\,\text{GeV}$ there are no solutions for both masses at the same time.

With regard to the dependence of the results on the parameters κ and M, the following was found. A change in the parameter κ, which parametrizes the matching between the four-fermion model and the EFT (with scalar fields), was found to be correlated with a change in the value of p. The range of values for p were always small, as consistency requires. On the other hand, values of M were constrained to be orders of magnitude below Λ, so the results were not dominated by the CCs. This is a welcome feature because otherwise the full knowledge of the interactions would be required. Still, it is worth pointing out that once the correct values of m_t and m_h are obtained, all the couplings and scales are quite constrained.

The Majorana mass terms of the new fermions, μ_ν and μ_χ, are completely free parameters that are adjusted in order to obtain the light neutrino masses, $m_\nu = 0.05\,\text{eV}$, in the ISS mechanism, Eq. (1.53). However the complete analysis of neutrino masses requires more than one generation of new fermions, although given the freedom in the Majorana mass terms, there should be no problem for adjusting light neutrino masses and mixings. Alternatively, it is also possible to generate the Majorana mass terms by using composite scalars breaking lepton number, see Ref. [129].

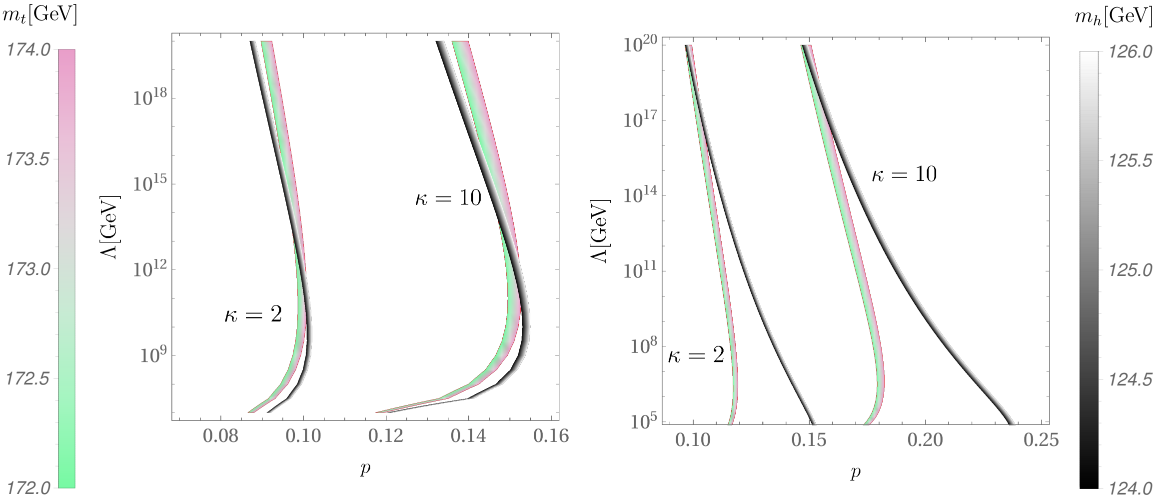

Figure 4.3: Region of p, Λ that can reproduce values of m_t in a region of 1 GeV around $m_t = 173$ GeV (band with green-pink colors) and m_h in a region of 1 GeV around $m_h = 125$ GeV (gray band). On the left for $M = 10^3$ TeV and on the right for $M = 1$ TeV. In each plot we present results for two different values of κ.

Majoron as a DM candidate

As mentioned before, our model leads to a Goldstone boson after SSB of the lepton number symmetry $U(1)_L$. This particle has purely derivative couplings and therefore the scattering amplitudes vanish at zero momenta. This special property makes the Goldstone boson able to evade the DD constrains as a particle of DM.[7] For this reason we would like to know whether the Goldstone boson could be a good DM candidate. Thereby we need to consider the addition of a soft explicit symmetry breaking term in the Lagrangian, for example $\mu_S^2 S^2 + \text{H.c}$, to make the Goldstone boson a massive particle. In this case, the pseudo-Goldstone boson is called *Majoron* because it is associated with $U(1)_L$, see e.g. Refs. [127, 130–135].

However, the model implemented here leads to a 1-loop interaction among the SM fermions, f, and the Majoron: $y_f \theta \overline{f} f$; which could produce the decay of the Majoron if it is kinematically allowed, see Fig. 4.4. The 1-loop coupling is proportional to:

$$y_f \propto \frac{y_\nu^2}{16\pi^2} \frac{m_f}{u} \,, \tag{4.16}$$

where m_f is the fermion mass.

Unfortunately, the Yukawa couplings in the composite scheme are closed to

---

[7] Details on the Goldstone boson's interactions are discussed in Ch. 6.

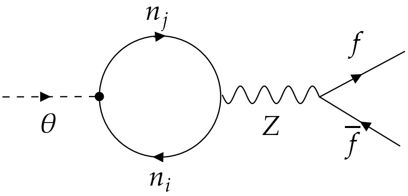

Figure 4.4: Diagramatic representation of the Majoron decay at 1-loop level to SM fermions f, with Majorana neutrino mass eigenstates $n_{i,j}$ running in the loop.

1 ($y_\nu \sim 1$) and so y_f would make the decay widths to be large, compromising the stability as a DM particle, at least in the range of values of u used in this chapter. Constraints in the lifetime of DM set a lower limit of ten times the age of the Universe.[8] Therefore, the Majoron generated in this model is not a good DM candidate in the composite scenario.[9]

---

[8] These lower limits depend on the mass of the DM particle and decay channels, for details see e.g. Refs. [136–144]

[9] The exclusion could also be due to indirect detection constraints, as the fermions could generate photons in the final states.

Chapter 5

Sterile neutrino portal

As mentioned in Ch. 4, the four-fermion interaction between the right-handed neutrino N_R and a new fermion χ_L generated a composite complex scalar at low-energy scales, which unfortunately could not lead to a good DM candidate in the composite scheme. In this chapter, we aim at finding a suitable DM candidate within the models that lead to an effective four-fermion interaction between the same fermions at low-energy scales, and exploring the possibility for the DM to be the fermion χ_L [4]. That is, the four-fermion operators are the result of integrating out some heavy scalar field (outside of the composite scheme) and we focus on models with t-channel contributions to the process $\chi\,\chi \to N\,N$. The DM phenomenology is analyzed in a dark sector (DS) composed of the two fermions and a scalar (mediator).

This link between the DM particle and neutrinos is an appealing option for solving simultaneously two of the main open problems in physics, see Secs. 1.4 and 1.5[1]. Furthermore, the stringent constraints on the interactions between the visible and dark sectors lead to consider N_R as the portal to DM, as N_R can have, for example, a Yukawa coupling with the $SU(2)$ doublets L and H (see e.g. Ref. [149]). This is the idea of sterile neutrino portal to DM.

In this analysis we assume the following: (i) the DM candidate is the Majorana fermion χ_L charged under a Z_2 symmetry which enforces its stability and (ii) the DM abundance is obtained in the freeze-out mechanism, which is natural in the set of parameters we will consider. We focus on the regimes where the DM abundance is generated by the annihilation $\chi\,\chi \to N\,N$, and in the cases when N is lighter than χ.

In Sec. 5.1 we present all the potential four-fermion operators suitable in this scenario and introduce their tree-level UV completions. Later, in Sec. 5.2, we analyze

---

[1] Examples can be found in Refs. [145–148].

the DM phenomenology of the scalar mediator in t-channel and, in Secs. 5.3 and 5.4, we consider a more detailed treatment of the generation of the relic abundance and the evolution of the dark sector temperature. Finally in Sec. 5.5, we briefly analyze the DM phenomenology of the scalar mediator in s-channel.

5.1 Portal operators and tree-level UV completions

The model contains, in addition to the SM particles, two chiral fermions, N_R and χ_L, that are singlets under the SM gauge group. The most general renormalizable Lagrangian with a discrete Z_2 symmetry for χ_L reads:

$$\begin{aligned}\mathcal{L}_4 =&\mathcal{L}_{\rm SM} + \overline{N_R} i\partial\!\!\!/ N_R + \overline{\chi_L} i\partial\!\!\!/ \chi_L + \mathcal{L}_6 \\ &- \left[\frac{1}{2} m_N \overline{N_R^c} N_R + \frac{1}{2} m_\chi \overline{\chi_L} \chi_L^c + y_\nu \overline{L} \tilde{H} N_R + \text{H.c.}\right] ,\end{aligned} \tag{5.1}$$

where $\mathcal{L}_{\rm SM}$ is the SM Lagrangian and in $\mathcal{L}_6$ we include the four-fermion effective operators that connect χ with N. There are only three possible operators of this type, which we refer as *portal operators* [150]:

$$\mathcal{L}_6 = \frac{c_1}{\Lambda^2}\,\mathcal{O}_1 + \left[\frac{c_2}{\Lambda^2}\,\mathcal{O}_2 + \frac{c_3}{\Lambda^2}\,\mathcal{O}_3 + \text{H.c.}\right] , \tag{5.2}$$

with

$$\begin{aligned}\mathcal{O}_1 &= (\overline{N_R}\chi_L)(\overline{\chi_L}N_R) = -\frac{1}{2}(\overline{N_R}\gamma_\mu N_R)(\overline{\chi_L}\gamma^\mu \chi_L) \,, \\ \mathcal{O}_2 &= (\overline{N_R}\chi_L)(\overline{N_R}\chi_L) = -\frac{1}{2}(\overline{N_R}N_R^c)(\overline{\chi_L^c}\chi_L) \,, \\ \mathcal{O}_3 &= (\overline{N_R^c}N_R)(\overline{\chi_L^c}\chi_L) = -\frac{1}{2}(\overline{N_R^c}\gamma_\mu \chi_L)(\overline{\chi_L^c}\gamma^\mu N_R) \,.\end{aligned} \tag{5.3}$$

Fierz identities have been used in the second equalities above, where the non-inclusion of $+1/2(\overline{N_R}\sigma_{\mu\nu}N_R^c)(\overline{\chi_L^c}\sigma^{\mu\nu}\chi_L)$ is due to the fact that for one generation of N or χ it vanishes. The Wilson coefficient c_1 is real, whereas c_2 and c_3 can be complex in general and Λ is the scale of the new physics, with $m_\chi, m_N < \Lambda$.

After EWSB the Higgs field takes a VEV and if m_N is not zero, the active neutrino acquires a mass from the seesaw mechanism, see Sec. 1.4.2, so that for $m_N \gg m_{\rm D}$,

$$\begin{aligned} m_{\rm light} &\simeq \frac{m_{\rm D}^2}{m_N} \,, &\qquad \nu_{\rm light} &\simeq \nu_L \,, \\ m_{\rm heavy} &\simeq m_N \,, &\qquad \nu_{\rm heavy} &\simeq N_R \,. \end{aligned} \tag{5.4}$$

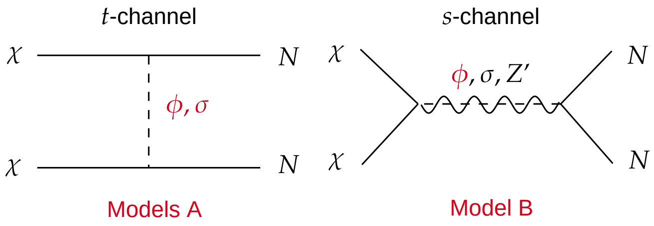

Figure 5.1: Feynman diagrams for DM annihilation into sterile neutrinos in the three possible mediator cases at tree level. ϕ and σ stand for a real and complex scalar singlets, respectively, whereas Z' is a vector mediator. In red color are displayed the mediators ϕ and σ, which we focus for the DM phenomenology in this chapter.

Model	AI	AII	AIII	B
c_1/Λ^2	$\dfrac{f^2}{m_\sigma^2}$	$\dfrac{f^2}{m_\sigma^2}$	$\dfrac{f^2}{m_\sigma^2}$	✗
c_2/Λ^2	$-\dfrac{f^2\mu_\sigma^2}{2m_\sigma^4}$	✗	$-\dfrac{f^2\mu_\sigma^2}{2m_\sigma^4}$	$-\dfrac{2f^*y}{m_\phi^2}$
c_3/Λ^2	✗	✗	✗	$\dfrac{fy}{m_\phi^2}$

Table 5.1: Matching conditions for the Wilson coefficients of the four-fermion operators dubbed portal operators, defined in Eq. (5.2).

The mass eigenstates are approximately equal to the weak eigenstates due to the neutrino mixing with the heavy states being very small: $\mathcal{O}\left(\sqrt{m_{\text{light}}/m_{\text{heavy}}}\right)$; i.e. smaller than 10^{-5} for $m_N \approx 1\text{GeV}$.

We have considered the *tree-level UV completions* of the neutrino portal operators of Eq. (5.3), interpreted as the models that generate the mentioned operators after integrating out at tree-level a heavy mediator field. They can be separated based on the mediator being a real/complex heavy scalar field, split in either t-channel or s-channel, or a heavy vector field. We called the scenarios in t-channel and s-channel as Models A and B, respectively, see Figs. 5.1 and 5.2.

We assume the interactions of the DS particles with the Higgs boson to be small in order for the annihilation $\chi\,\chi \to N\,N$ to dominate the freeze-out, although large enough to ensure early kinetic and chemical equilibrium between the two sectors, as we will discuss in Sec. 5.4.

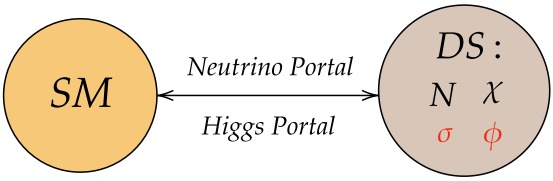

Figure 5.2: Schematic diagram of the analyzed set-up, in which the DS is composed of the sterile neutrino N, the DM χ and the heavy mediator σ or ϕ.

5.2 Model A: scalar mediator in t-channel

The mediator in this model is a complex scalar field $\sigma = (\rho + i\,\theta)/\sqrt{2}$, charged under the same Z_2 symmetry as χ_L. The Lagrangian reads[2]

$$\mathcal{L}_{\rm A} = \mathcal{L}_4 + (\partial_\mu \sigma)^* (\partial^\mu \sigma) - V_L(\sigma, H) - V_{\not{L}}(\sigma, H) - \left[f \overline{N_R} \chi_L \sigma + \text{H.c.} \right] , \tag{5.5}$$

and $V_L(\sigma, H)$ $[V_{\not{L}}(\sigma, H)]$ is the most general scalar potential that preserves [violates] lepton number symmetry $U(1)_L$, set as: $L(\chi_L) = 0$, $L(\sigma) = 1$ and $L(N_R) = 1$,

$$\begin{cases} V_L(\sigma, H) = & m_\sigma^2 \left|\sigma\right|^2 + \lambda_{\sigma H} \left|\sigma\right|^2 \left|H\right|^2 + \lambda_\sigma \left|\sigma\right|^4 \, , \\ V_{\not{L}}(\sigma, H) = & \frac{1}{2} \mu_\sigma^2 \, \sigma^2 + \lambda_2 \sigma^2 \left|H\right|^2 + \lambda_3 \sigma^2 \left|\sigma\right|^2 + \lambda_4 \sigma^4 + \text{ H.c.} \, . \end{cases} \tag{5.6}$$

In general, the fields N_R and χ_L can be re-phased so their masses are real and positive, while the complex field σ can be re-phased in order to make one of the terms in $V_{\not{L}}$ real. Due to this, the Yukawa coupling f should, in principle, be taken as a complex number; however, in some cases it can be made real in full generality. For f to be considered real it is necessary to assume a lepton conserving Lagrangian or to be in one of the following cases: (I) assume $m_N = 0$ or (II) set $V_{\not{L}} = 0$. The first scenario is motivated by lepton number conservation as it can be argued that there is only one explicit soft symmetry breaking term in $V_{\not{L}}$, and in particular, μ_σ^2 would be the softest possible breaking. We will study these cases separately as models AI and AII, with AI having only $\mu_\sigma^2 \neq 0$ in $V_{\not{L}}$.

Notice that with the lepton charges mentioned before, the portal operator $\mathcal{O}_1$ conserves $U(1)_L$, whereas $\mathcal{O}_2$ and $\mathcal{O}_3$ do not, see Eq. (5.3). This will shed some light on the operators generated from the UV completions.

In the following we will study the phenomenology of the models AI and AII, together with a hybrid case that we will dub AIII. The motivation for the last case

---

[2] In Eq. (5.5), $\mathcal{L}_4$ only contains the renormalizable operators, i.e. $\mathcal{L}_6 = 0$.

will become evident in what follows. Some comments on the cases studied:[3]

- **AI.** The Lagrangian is:

$$\mathcal{L}_{\mathrm{AI}} = \mathcal{L}_{\mathrm{A}}|_{m_N=0,\lambda_{2,3,4}=0}. \tag{5.7}$$

This set up is interesting because it predicts a finite mass m_N at 1-loop level,[4] see Fig. 5.3. In the completely general case of n_N and n_χ generations of N_R and χ_L respectively, the result is, like in the Scotogenic model,

$$(m_N)_{ij} = \sum_{k=1}^{n_\chi} \frac{f^*_{ik} f^*_{jk} m_{\chi_k}}{32\pi^2} F(m_\rho^2, m_\theta^2, m_{\chi_k}^2), \tag{5.8}$$

for a basis in which the matrix m_χ is diagonal with real and positive entries m_{χ_k}; m_ρ and m_θ are the masses of the scalars ρ and θ, respectively. The loop function F is,

$$F(x,y,z) = \frac{x}{x-z}\log\left(\frac{x}{z}\right) - \frac{y}{y-z}\log\left(\frac{y}{z}\right). \tag{5.9}$$

When σ is integrated out, a $U(1)_L$ conserving (violating) operator is generated: $\mathcal{O}_1$ ($\mathcal{O}_2$); with the matching conditions given in Tab. 5.1. No other non-renormalizable operators of $D \leq 6$ are generated, and, as was expected, the Wilson coefficient c_2 is proportional to the soft breaking parameter μ_σ^2. On the other hand, if the integration is taken separately for the real, ρ, and imaginary, θ, components, we have the following matching relations:

$$\frac{c_1}{\Lambda^2} = \frac{f^2}{2}\left(\frac{1}{m_\rho^2} + \frac{1}{m_\theta^2}\right), \qquad \frac{c_2}{\Lambda^2} = \frac{f^2}{4}\left(\frac{1}{m_\rho^2} - \frac{1}{m_\theta^2}\right), \tag{5.10}$$

where

$$m_\rho^2 = m_\sigma^2 + \mu_\sigma^2, \qquad m_\theta^2 = m_\sigma^2 - \mu_\sigma^2. \tag{5.11}$$

For $\mu_\sigma^2/m_\sigma^2 \ll 1$, the matching conditions reduce to those of Tab. 5.1.

- **AII.** The absence of lepton number violation in the interactions of the Lagrangian is reflected in the lepton conserving operator generated after integrating out σ, see Tab. 5.1. The relic abundance obtained via the freeze-in mechanism in this model was studied in Refs. [157–159].

---

[3] Bear in mind that the hierarchy of masses $m_{\theta,\rho} > m_\chi > m_N$ is always considered here.

[4] Ref. [151] considered a similar mechanism for light (mostly-active) neutrinos to acquire masses at 1-loop level, which, in fact, is analogous to that of the scotogenic model [152] and its generalisations [153–155]. For a review see Ref. [156].

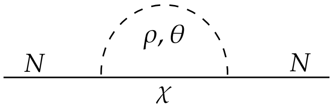

Figure 5.3: Radiative generation of m_N in Model AI in the mass basis.

- **AIII.** This model has the same Lagrangian as model AI but with $m_N \neq 0$, and therefore the generated portal operators and matching conditions are shared. In this manner, this model is the most general case with a complex mediator without Higgs portal and self-interaction couplings in $V_{\not{L}}$. It is motivated by its relation to the model in which instead of the complex scalar field, a real scalar is considered as the mediator, as it will be commented below.

With regard to the parameter space considered in the DM phenomenology analysis, a wide range of masses for m_χ and m_N were taken with the natural assumption of Yukawa coupling $f = 1$, see Fig. 5.5. The mass values for m_N are subjected to stringent BBN constraints and the minimum allowed value of $m_N = 2\,\text{GeV}$ was chosen in the plots. In the same way, in model AI, the value of $\mu_\sigma = 10^4\,\text{GeV}$ was chosen so that the m_N generated radiatively is allowed. It is important to mention that when the coupling f is taken to be of order $\mathcal{O}(1)$, the mechanism to reproduce the measured relic abundance is freeze-out, in the range of masses considered, as the DM reaches thermal equilibrium with the other DS particles.

The Fig. 5.5 shows in the dashed-blue line the parameter space where the correct relic abundance is achieved for Models AI (left) and AII (right). This was computed in the analytical approach, explained in Sec. 1.5.2.[5] The white and light blue regions in the plots correspond to values of parameters satisfying $\Omega h^2 \leq 0.12$ and $\Omega h^2 > 0.12$ respectively. The former is able to provide some fraction of the total relic abundance of DM and evade all the experimental bounds, while the last would overclose the Universe. In summary, the regions with a good DM candidate are approximately in the parameter space of $100\,\text{GeV} \lesssim m_\chi \lesssim 300\,\text{GeV}$ and $200\,\text{GeV} \lesssim m_\sigma \lesssim 300\,\text{GeV}$ for model AII; and of $100\,\text{GeV} \lesssim m_\chi \lesssim 800\,\text{GeV}$ and $300\,\text{GeV} \lesssim m_\theta \lesssim 800\,\text{GeV}$ for model AI. In the case of AI, the values for the 1-loop generated RH neutrino mass are $2\,\text{GeV} \lesssim m_N \lesssim 10\,\text{GeV}$.

We have also found that the results for model AII and AIII are very similar, for purely real or imaginary Yukawa coupling, with slight differences when m_χ tends to be close to m_θ. Even so the differences are not obvious in the logarithmic scale of Fig. 5.5, so the l.h.s plot should apply to model AIII quite accurately.

---

[5] The cross sections employed can be found in Ref. [4].

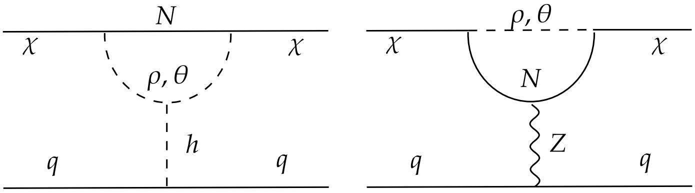

Figure 5.4: Diagrammatic representation of the 1-loop penguin contributions to DM scattering off nuclei.

Constraints on Model A

In Model A, tree-level contributions to DD signals are absent, however this is not the case at 1-loop order. The Higgs portal term and the neutrino mixing are responsible for the contributions of the diagrams shown in Fig. 5.4. Furthermore, there are 1-loop diagrams generating invisible Higgs and Z boson decays when they are kinematically allowed. Although, given the smallness of the neutrino Yukawa coupling y_ν and the unimportant Higgs portal coupling of this framework, all the bounds are easily evaded.[6]

The pink and light brown regions of the plots represent the ID bounds of CMB and dSphs, respectively, from Ref. [161], see Sec. 1.5.1. However, ID constraints from DM being captured in the Sun are neglected due its minimal interactions with the SM quarks.

Two extra cases for scalar mediator in t-channel:

- When lepton number is conserved, $m_N = 0$ and $V_{\not{L}} = 0$, neutrinos are of Dirac-type and only $\mathcal{O}_1$ is generated. Constraints on this case are easily evaded given the p-wave nature of the annihilations $\chi\,\chi \to N\,N$ and the smallness of the interactions with the visible sector.

- In model A, where the Lagrangian is given in Eq. (5.5), one of the scalar components could be very heavy and so decoupled from the rest, leading to an effective model in which the mediator is a real scalar field, named ϕ. The most general Lagrangian in such a model is:

$$\mathcal{L} = \mathcal{L}_4 + \frac{1}{2}\left(\partial_\mu \phi\right)\left(\partial^\mu \phi\right) - V(\phi, H) - \left[f\overline{N_R}\chi_L\phi + \text{H.c.}\right] , \tag{5.12}$$

---

[6] A detailed analysis of 1-loop contributions can be found in Ref. [160].

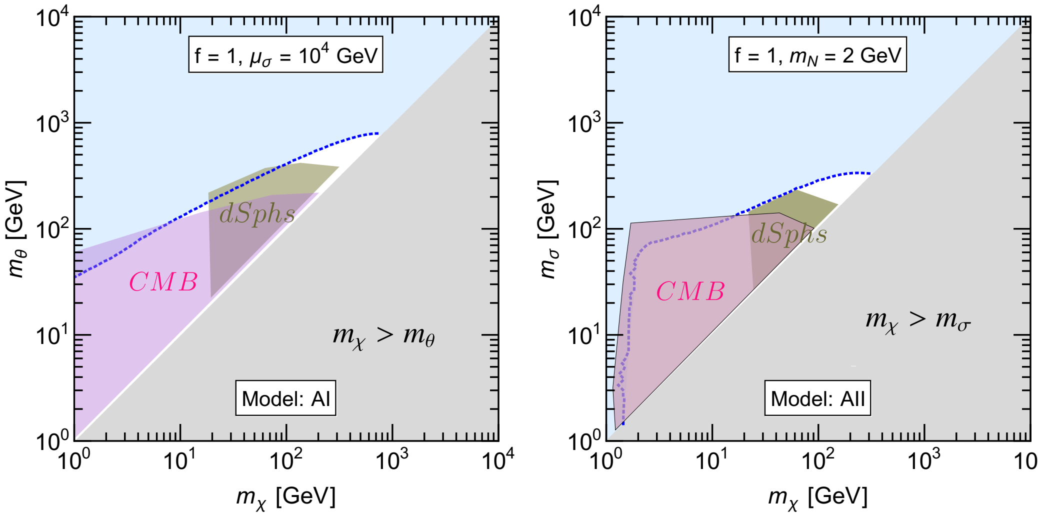

Figure 5.5: Relevant parameter space for models AI (left) and AII (right). Values of the fixed parameters are specified in the upper region of each plots. The color-code is specified in the text. The pink and light brown regions of the plots represent the excluded area from the ID bounds of CMB and dSphs respectively.

where

$$V(\phi, H) = \frac{1}{2} m_\phi^2 \phi^2 + \lambda_{\phi H} \phi^2 |H|^2 + \lambda_\phi \phi^4 \,. \tag{5.13}$$

Since ϕ is a real field and N_R and χ_L are re-phased to have real and positive Majorana masses, the possible phase of the Yukawa coupling f can not be removed and f should be treated as a complex number. Taking μ_σ^2 positive (negative), then the field ρ (θ) can be integrated out and θ (ρ) would be associated with ϕ. In such a scenario the phenomenological analysis discussed for model AIII can be associated to the real scalar mediator case, when the Yukawa coupling is correspondingly purely real or imaginary. Furthermore, the $D \leq 6$ generated operators would be $\mathcal{O}_1$ and $\mathcal{O}_2$, see Table 5.1 for model AIII.

With regard to the DM phenomenology in the regime $m_N \leq m_\chi \leq m_\theta$, Ref. [162] explored the generation of correct relic abundance in the limit $m_N \to 0$; while Refs. [163] and [164] focused when particles were almost degenerate for the pair (m_N, χ) and triplet (m_N, χ, θ) cases respectively. On the other side, an extended region of masses m_N and m_χ was considered in Ref. [161], with particular attention to the ID limits. Alternatively, beyond the freeze-out mechanism, Refs. [165, 166] considered the freeze-in mechanism for either χ or θ being the DM; while Ref. [167] analyed when the two sectors are fully thermally decoupled in the regime $m_\phi > m_\chi + m_N$.

5.3 Results with complete Boltzmann equations

In the previous section, the results for the relic abundance of DM were computed using the analytical approach, explained in Sec. 1.5.2, and relying on the following important assumptions and approximations:

- The dark and SM sectors share the same temperature until freeze-out. This is achieved if the two sector are in kinetic equilibrium until freeze-out, or if there is one or more relativistic particles in the DS and none of them become non-relativistic after the kinetic equilibrium occurs and before the freeze-out, as is discussed in Sec. 5.4. In our models we expect the kinetic equilibrium to be due to the neutrino or Higgs portals.[7]
- Only $2 \leftrightarrow 2$ processes are taken into account.
- Only the DM number density n_{DM} is evolved out of thermal equilibrium, with all the other particles in equilibrium with the heat bath at all times. The differential equation for the evolution of the number density of DM has the form of Eq. (1.74): when j species of particles contribute with $2 \leftrightarrow 2$ processes,

$$\frac{dY}{dx} = -\sum_{i}^{j} \frac{\lambda \langle \sigma v \rangle_i}{x^2} \left(Y^2 - Y_{eq}^2 \right) , \tag{5.14}$$

- The value for freeze-out is approximated or simplified to $x_f = 20$. After the freeze-out occurs the equilibrium yield Y_{eq} is neglected.

In turn, when we employed `micrOMEGAs` [98, 99] the forth assumption is lifted and the freeze-out happens when $Y \equiv 3.5 Y_{eq}$ and Y_{eq} is only neglected after $Y \equiv 10\, Y_{eq}$ occurs. Despite this, the analytical and `micrOMEGAs` computations perfectly agree in the plot of logarithmic scale shown in Fig. 5.5. However, in some particular regions of the parameter space the second and third assumptions should be dropped as they are not good approximations. In this manner, it was necessary to abandon `micrOMEGAs` and developed the required tools for solving more complete Boltzmann equations that include $1 \leftrightarrow 2$ processes and allow more particles to evolve out of thermal equilibrium as the DM does.[8]

Accordingly, differences in the results compared with the analytical approach appear when $1 \leftrightarrow 2$ processes have a strong effect or when the DM and another

---

[7] Examples of corrections due to a DS being decoupled from the SM close to the freeze-out can be found in e.g. Refs. [168, 169]

[8] `micrOMEGAs` allows for a second particle to evolve out of thermal equilibrium with the DM, however this fell short in our case with three particles in the DS.

particle (i.e. SM or DS particles) have similar freeze-out temperatures. In this section we review the comparison of the relic abundance obtained with the full set of Boltzmann equations (BEQs) and what we will call standard approximation (STD), which includes the first, second and third approximations mentioned above. This review will take place in model AIII and the complete BEQs, for $m_\theta > m_\chi + m_N$ and ρ being decoupled, are expressed as:

$$\begin{aligned} x\, s\, H \frac{dY_\chi}{dx} &= -\langle\sigma v\rangle_{\chi\chi\to NN} s^2 \left(Y_\chi^2 - \left(\frac{Y_\chi^{\rm eq}}{Y_N^{\rm eq}}\right)^2 Y_N^2\right) + \langle\sigma v\rangle_{\theta\theta\to\chi\chi} s^2 \left(Y_\theta^2 - \left(\frac{Y_\theta^{\rm eq}}{Y_\chi^{\rm eq}}\right)^2 Y_\chi^2\right) \\ &\quad + s\,\tilde{\Gamma}_\theta \left(Y_\theta - \frac{Y_\chi Y_N Y_\theta^{\rm eq}}{Y_\chi^{\rm eq} Y_N^{\rm eq}}\right), \end{aligned} \tag{5.15}$$

$$\begin{aligned} x\, s\, H \frac{dY_\theta}{dx} &= -\langle\sigma v\rangle_{\theta\theta\to NN} s^2 \left(Y_\theta^2 - \left(\frac{Y_\theta^{\rm eq}}{Y_N^{\rm eq}}\right)^2 Y_N^2\right) - \langle\sigma v\rangle_{\theta\theta\to\chi\chi} s^2 \left(Y_\theta^2 - \left(\frac{Y_\theta^{\rm eq}}{Y_\chi^{\rm eq}}\right)^2 Y_\chi^2\right) \\ &\quad - s\,\tilde{\Gamma}_\theta \left(Y_\theta - \frac{Y_\chi Y_N Y_\theta^{\rm eq}}{Y_\chi^{\rm eq} Y_N^{\rm eq}}\right), \end{aligned} \tag{5.16}$$

$$\begin{aligned} x\, s\, H \frac{dY_N}{dx} &= \langle\sigma v\rangle_{\chi\chi\to NN} s^2 \left(Y_\chi^2 - \left(\frac{Y_\chi^{\rm eq}}{Y_N^{\rm eq}}\right)^2 Y_N^2\right) + \langle\sigma v\rangle_{\theta\theta\to NN} s^2 \left(Y_\theta^2 - \left(\frac{Y_\theta^{\rm eq}}{Y_N^{\rm eq}}\right)^2 Y_N^2\right) \\ &\quad - s\,\tilde{\Gamma}_N \left(Y_N - Y_N^{\rm eq}\right) + s\,\tilde{\Gamma}_\theta \left(Y_\theta - \frac{Y_\chi Y_N Y_\theta^{\rm eq}}{Y_\chi^{\rm eq} Y_N^{\rm eq}}\right), \end{aligned} \tag{5.17}$$

in terms of the yields $Y_i = n_i/s$, where n_i is the number density for species i and s is the total entropy density, $x = m_\chi/T$, H is the (x-dependent) Hubble rate, and the superscript "eq" denotes equilibrium distributions with zero chemical potential, as in Refs. [93, 94] and Sec. 1.5.2. $\tilde{\Gamma}_i$ corresponds to the thermal decay rates of species i, given in Eq. (C.13). When $m_N < m_h(T)$, decays into N are addressed by the following substitution $\tilde{\Gamma}_N \to \tilde{\Gamma}_h$ with,

$$\tilde{\Gamma}_h = \frac{1}{n_N^{\rm eq}} \int \frac{d^3p}{(2\pi)^3 E_h} f_h^{\rm eq} m_h \Gamma_h \,. \tag{5.18}$$

The Higgs boson decay rate is considered with the approximation taken in Ref. [170], in which all the four states of the Higgs doublet have the Higgs boson mass $m_h(T)$. The temperature dependence of the masses, in particular the scalars, was considered as in Ref. [163]. The thermally averaged cross section $\langle\sigma v\rangle$ is given by [93]:

$$\langle\sigma v\rangle = \frac{1}{8m^4 T K_2^2(m/T)} \int_{4m^2}^{\infty} ds\, \sigma(s) \left[s - 4m^2\right] \sqrt{s}\, K_1\left(\sqrt{s}/T\right), \tag{5.19}$$

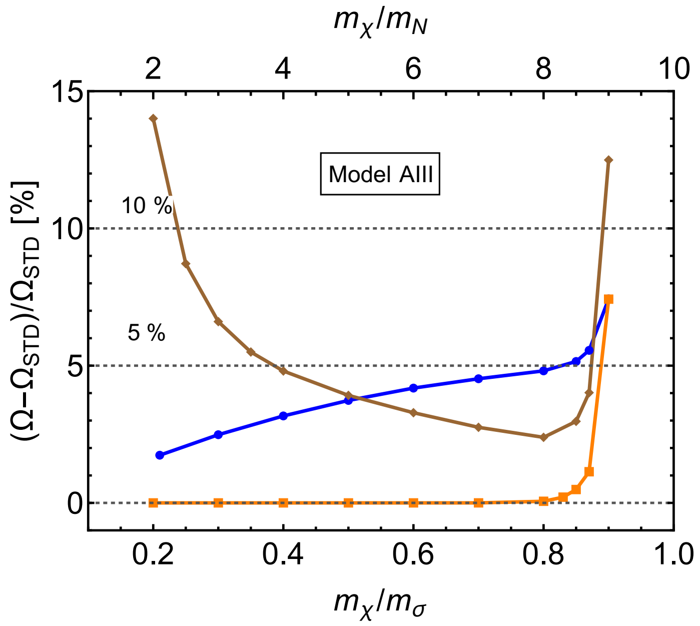

Figure 5.6: Comparison of the relative deviation in the relic abundance (Ω) and the standard approximation ($\Omega_{\rm STD}$) computed in different scenarios of Model AIII: by solving the full set of BEQs in Eqs. (5.15)–(5.17) (brown line), by setting the neutrino N in thermal equilibrium (blue line) and by considering N in thermal equilibrium and $1 \leftrightarrow 2$ processes (orange line). The fixed parameters considered are $f = 1$ and $m_\sigma = 1\,\text{TeV}$.

where $K_{1,2}$ are modified Bessel functions, and m is the DM mass.

In Fig. 5.6 we show the relative deviation of the relic abundance obtained from the BEQs and STD approaches. The quantity plotted is $(\Omega - \Omega_{\rm STD})/\Omega_{\rm STD}$ [%], as a function of $m_\chi/m_{\theta,N}$ for Model AIII. Furthermore, the following three different scenarios were considered in Ω:

- **i)** We include in the STD approach the evolution of θ out of equilibrium with only $2 \leftrightarrow 2$ processes, this implies using Eqs. (5.15) and (5.16); this scenario is represented by a blue line.

- **ii)** To (i), the $1 \leftrightarrow 2$ processes are included; this scenario is represented by an orange line.

- **iii)** The evolution of N is taken freely out of equilibrium and then the complete BEQs in Eqs. (5.15)–(5.17) are met; this scenario is represented by a brown line.

The BEQs in Eqs. (5.15)–(5.17) include the other DS particles, θ and N, as evolving in temperature and forming a coupled system of equations.[9] The impact was more relevant when N and/or θ and the DM became non-relativistic at nearly the same temperature, that is, when the masses of the particles were similar. The resulting effect is a tendency for the freeze-out to occur earlier,[10] as is seen by the orange line being away from zero in Fig. 5.6.

On the other side, the BEQs allow for $1 \leftrightarrow 2$ processes involving the production/decay of N from/to SM particles and the decays of θ to χ and N. This inclusion acts as a source of damping towards the equilibrium functions, as the expression, $dY/dx \propto (Y\text{-}Y_{eq})$, suggests. In this manner particles would follow the equilibrium for lower temperatures provided that the decaying particle is not exceedingly Boltzmann suppressed. For example, in Fig. 5.6, the θ decays/inverse-decay carry the system to equilibrium for longer as it is shown by the orange line being closer to zero than the blue line.

Finally, in Fig. 5.7 we considered the evolution of the yields in one illustrative point of the parameter space of Fig. 5.6. The goal is to exhibit the effect of the $1 \leftrightarrow 2$ processes, which clearly shows the evolution of Y_θ staying closer to the equilibrium values after comparing the gray lines in the top and bottom panels. The blue and orange lines follow closely the black lines. It should be taken into consideration that the relic abundance associated with each panel would be proportional to

$$\Omega h^2 \propto m_\chi Y_\chi^{total} = m_\chi \left(Y_\chi + Y_\theta\right) \, , \tag{5.20}$$

because θ will, sooner or later, decay to χ and N when it is kinematically allowed.

In summary, allowing more particles to go out of thermal equilibrium brings instability to the system; while, in contrast, the inclusion of $1 \leftrightarrow 2$ processes act as a restoring agent towards equilibrium.

The region of parameter space chosen for Fig. 5.6 was such that it represented where the use of BEQs is more suitable than the STD case. With regard to the conclusion of the comparison of the two approaches, the deviation is below the 10 % in almost all of the parameter space, except for $m_\chi \sim m_\sigma$ and $m_\chi \sim m_N$.

5.4 Evolution of the dark sector temperature

We discuss here the evolution of the dark sector temperature based on the conservation of the total entropy S_{tot} of the Universe. Its importance is manifested when the kinetic equilibrium between the two sectors vanish and they can develop different

---

[9] It should be noted that when N and θ are assumed to be in thermal equilibrium at all temperatures, $Y_N \equiv Y_N^{eq}$ and $Y_\theta \equiv Y_\theta^{eq}$, then Eqs. (5.15)–(5.17) reduce to Eq. (5.14).

[10] This feature also arose in Model A with a real scalar mediator, see Refs. [163, 164].

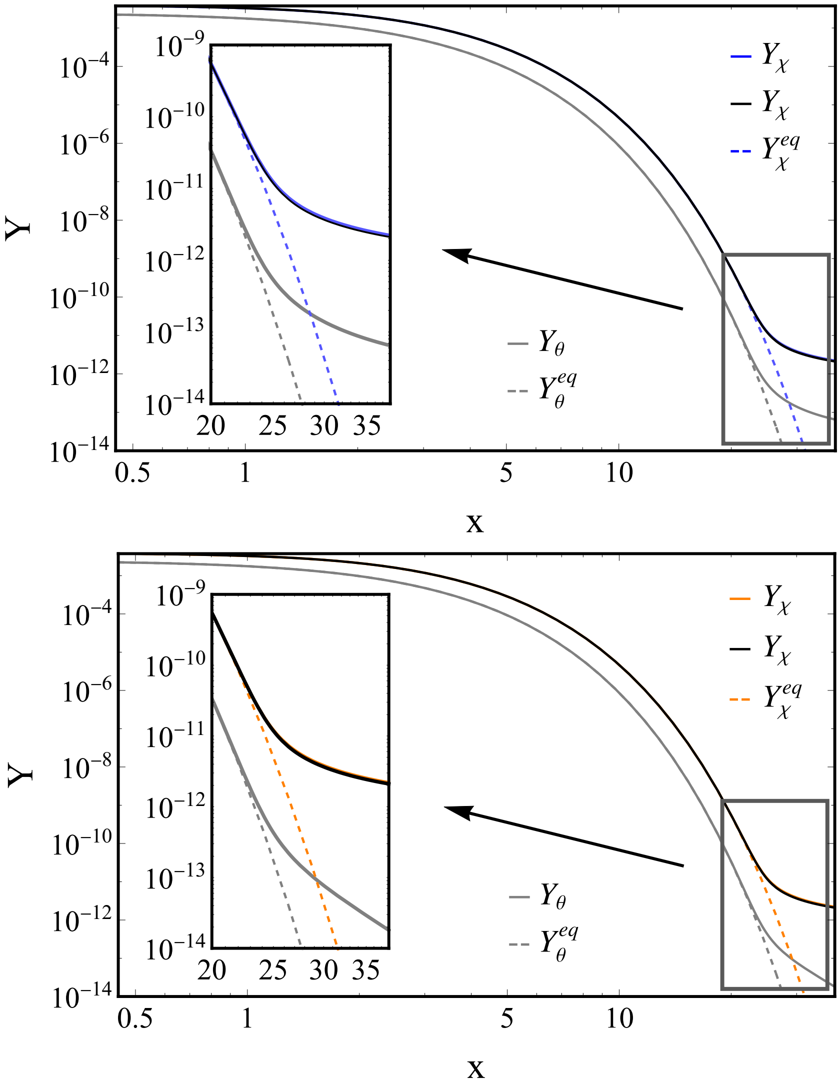

Figure 5.7: Evolution of the yields of the fields θ and χ in terms of $x = m_\chi/T$, for the Model AIII. The $1 \leftrightarrow 2$ processes are (not) considered in the top (bottom) panel. The gray line represents the yield of the field θ. The blue and orange lines stand for the evolution of χ in the color-code mentioned in the text. The black line represents the yield of χ in the STD approach. The dashed lines represent the yields of equilibrium. The point of the parameter space was chosen such that the effect of the $1 \leftrightarrow 2$ processes becomes visible. The values are $f = 1$, $m_N = 100\,\text{GeV}$, $m_\theta = 1\,\text{TeV}$ and $m_\chi = 899\,\text{GeV}$.

temperatures, invalidating the first assumption of the analytical approach. The total entropy of the Universe is the sum of the entropies of the two sectors:

$$S_{tot} = a^3\left(s_{\rm SM} + s_{\rm DS}\right) \,, \tag{5.21}$$

where $s_{\rm SM}$ and $s_{\rm DS}$ are the entropy densities of the SM and DS, respectively; a is the scale factor which evolves in time as expressed in the Friedmann equation, Eq. (E.4):

$$H^2 = \frac{8\pi}{3} G\rho_{tot} - \frac{\kappa}{a^2} \,, \tag{5.22}$$

with ρ_{tot} being the total energy and $\kappa = 0$ in a flat Universe. H is the Hubble parameter defined as $H = \dot{a}/a$. The entropy conservation gives

$$\frac{dS_{tot}}{dt} = 3a^2\dot{a}\left(s_{\rm SM} + s_{\rm DS}\right) + a^3\left(\dot{s}_{\rm SM} + \dot{s}_{\rm DS}\right) = 0 \,, \tag{5.23}$$

$$\boxed{-3H\left(s_{\rm SM} + s_{\rm DS}\right) - \dot{s}_{\rm SM} = \dot{s}_{\rm DS}} \tag{5.24}$$

We assume the total energy density is dominated by the SM: $\rho_{\rm SM} \gg \rho_{\rm DS}$ and $s_{\rm SM} \gg s_{\rm DS}$. Then to order zero in $s_{\rm DS}$ we have:

$$-3Hs_{\rm SM} = \dot{s}_{\rm SM} \tag{5.25}$$

Plugging Eq. (5.25) into Eq. (5.23) leads to the evolution of s_{DS} to the first order:

$$-3Hs_{\rm DS} = \dot{s}_{\rm DS} \,. \tag{5.26}$$

The ratio of the previous two equations gives:

$$\frac{\dot{s}_{\rm SM}}{\dot{s}_{\rm DS}} = \frac{s_{\rm SM}}{s_{\rm DS}} \,, \tag{5.27}$$

whose solution is $s_{\rm DS}/s_{\rm SM} = c$, with c being a constant that depends on the boundary conditions.[11] During the radiation dominated era: $s_{\rm SM} = (2\pi^2/45)g_* T^3$; and the expression for $T_D(T)$ can be obtained from the knowledge of dependence of $s_{\rm DS}$ with T_D.[12]

In particular, if the particles in the DS are relativistic then $s_{\rm DS} = (2\pi^2/45)g_D T_D^3$, with g_D accounting for the relativistic degrees of freedom; therefore, the two temperatures are proportional to one another, $T \propto T_D$. While if the DS particles are

---

[11] This solution implies the same relation between the two sectors' entropy as in Ref. [167].

[12] The dependence of $s_{\rm DS}$ with T_D follows from the general expression: $s_{\rm DS} = (\rho_D + p_D)/T_D$; where ρ_D and p_D are the energy and pressure densities of the dark sector, see e.g. Ref. [167].

non-relativistic, from $s_{\text{DS}} = c\, s_{\text{SM}}$ we have:

$$c_1 T^3 = c_2 (T_D)^{1/2} \exp(-m/T_D)\,, \tag{5.28}$$

where c_1 and c_2 are constants and m is the mass of the lightest particles in the DS (in our set up it is always N).

Notice that if at some moment in the history of the Universe there is kinetic equilibrium between the two sectors, then the temperatures stay equal after kinetic decoupling until the effective relativistic degrees of freedom of DS change (or freeze-out occurs). If we define $\xi = T_D/T$, then $\xi \approx 1$ in the above context and there is no impact of kinetic decoupling from the heat bath in the final relic abundance, which is what occurs in the white region of Fig. 5.5.

For illustration, the evolution of $\xi(T_D)$ can be seen in Fig. 5.8 when χ and N (red line) or only N (blue line) are/is relativistic at the time of the kinetic decoupling. In this case, it is shown that if the kinetic decoupling happens when only N is relativistic then $\xi \approx 1$ until the freeze-out ($T_D^{fo} \approx m_\chi/20 > m_N$). For the parameter space of the white region of Fig. 5.5 to satisfy $T \approx T_D$, it is necessary a Higgs portal coupling $\lambda_{\sigma H} \geq 10^{-6}$, as can be seen in Fig. 5.9 for the same values of masses as in Fig. 5.8.

5.5 Model B: real scalar mediator in s-channel

The mediator in this model is a real scalar field ϕ, that is not charged under the discrete Z_2 symmetry and the Lagrangian reads,

$$\mathcal{L}_{\text{B}} = \mathcal{L}_4 + \frac{1}{2}\,(\partial_\mu \phi)\,(\partial^\mu \phi) - V(\phi, H) - \left[f \overline{N_R^c} N_R\, \phi + y \overline{\chi_L^c} \chi_L\, \phi + \text{H.c.}\right], \tag{5.29}$$

with $V(\phi, H)$ being the most general scalar potential:[13]

$$V(\phi, H) = \frac{1}{2} m_\phi^2\, \phi^2 + \mu_\phi \phi^3 + \lambda_\phi\, \phi^4 + \mu_{\phi H} \phi |H|^2 + \lambda_{\phi H} \phi^2 |H|^2\,. \tag{5.30}$$

The Yukawa couplings f and y should be taken as complex numbers in full generality. In this model, the lepton violating portal operators $\mathcal{O}_2$ and $\mathcal{O}_3$ appear after integrating out the scalar ϕ, and the matching conditions are given in Tab. 5.1. Furthermore four other operators at $D \leq 6$ are generated: at $D = 5$ we have,[14]

$$\mathcal{L}_5 \supset \frac{\mu_\phi}{m_\phi^2} (f \overline{N_R^c} N_R + y \overline{\chi_L^c} \chi_L)(H^\dagger H)\,, \tag{5.31}$$

---

[13] Linear terms of ϕ in the Lagrangian, Eq. (5.29), can always be removed by a shift.

[14] An interesting set up with this type of interaction between a fermion singlet and two Higgs doublets is developed in Refs. [171, 172].

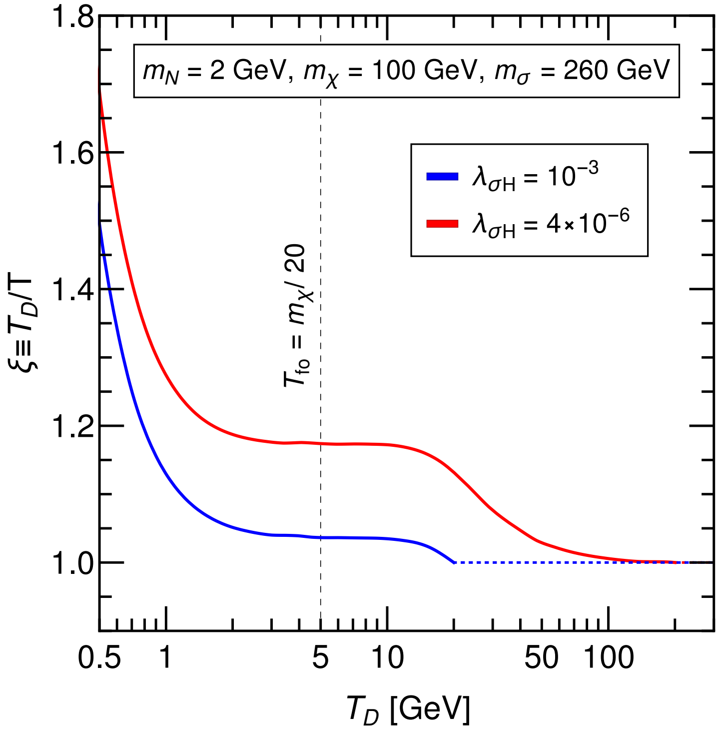

Figure 5.8: Evolution of the ratio of the dark and visible sectors temperatures, $\xi = T_D/T$, for two representative values of the Higgs portal coupling $\lambda_{\sigma H}$ in model AIII. The parameters have been fixed to the values $f = 1$, $m_N = 2\,\text{GeV}$, $m_\chi = 100\,\text{GeV}$ and $m_\sigma = 260\,\text{GeV}$. For $\lambda_{\sigma H} = 10^{-3}$ (blue line), N is relativistic at the time of kinetic decoupling, $T_D = 20\,\text{GeV}$, and down to the DM freeze-out at $T_D = 5\,\text{GeV}$. For $\lambda_{\sigma H} = 4 \times 10^{-6}$ (red line), both χ and N are relativistic at kinetic decoupling, $T_D = 200\,\text{GeV}$, but only N is at the freeze-out.

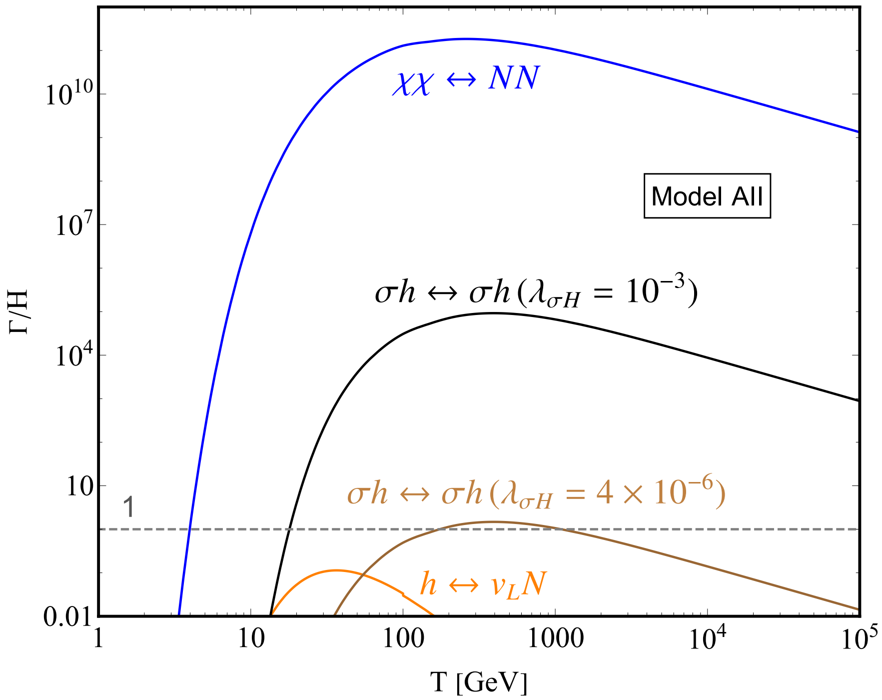

Figure 5.9: Ratio of the contributions of the 1 ↔ 2 and 2 ↔ 2 processes to the Hubble parameter in Model AII. The parameters were taken to be $f = 1$, $m_N = 2\,\mathrm{GeV}$, $m_\chi = 100\,\mathrm{GeV}$ and $m_\sigma = 260\,\mathrm{GeV}$, corresponding to a point in Fig. 5.5 reproducing the correct relic abundance and evading all the experimental bounds.

and at $D = 6$,[15]

$$\mathcal{L}_6 \supset \frac{|f|^2}{m_\phi^2}(\overline{N_R^c}N_R)(\overline{N_R}N_R^c) + \frac{|y|^2}{m_\phi^2}(\overline{\chi_L^c}\chi_L)(\overline{\chi_L}\chi_L^c)\,. \tag{5.32}$$

After EWSB, the first $D = 5$ operator contributes to the (mostly-)sterile neutrino mass and to the DM Majorana mass, as well as to the decays of the Higgs boson or N, depending on the value of m_N. The second $D = 5$ operator constitutes the fermionic Higgs portal, see e.g. Refs. [173–175]. Finally the $D = 6$ operators correspond to four-fermion self-interactions.[16]

The DM phenomenology in this model is considered in the same regions of masses m_N and m_χ as in Models A. Furthermore the Yukawa couplings, $f = f_r + if_i$ and $y = y_r + iy_i$, are studied separately in its real and imaginary components: (I) $f_r = y_r = 1$ and (II) $f_i = y_i = 1$. The motivation is due to the different properties of the averaged cross section of annihilation of DM, being p-wave when the Yukawas are real, and thus evading the ID bounds. For illustration we took $|f| = |y| = 1$.

Regions with good DM candidates were found to be different in both cases, related to the dominance of the resonance in Model BI. For Model BI, it was in the range $2\,\text{GeV} \lesssim m_\chi \lesssim 10\,\text{TeV}$ and between $2\,\text{GeV} \lesssim m_\phi \lesssim 20\,\text{TeV}$, whereas for Model BII the region is shrunk into $30\,\text{GeV} \lesssim m_\chi \lesssim 50\,\text{TeV}$ and $1\,\text{TeV} \lesssim m_\phi \lesssim 100\,\text{TeV}$.

Extra models with mediator in s-channel

In the following we briefly describe the remaining models with a mediator in the s-channel that generate the four-fermion portal operators at low energies:

- **Complex mediator**
  The mediator is a complex scalar field $\sigma = \rho + i\theta$, and it entails the conservation of a global $U(1)$ symmetry, which can be associated with lepton number. The charges of the particles in the DS should be $L(N_R) = L(\chi_L^c) = 1$ and $L(\sigma) = -2$. The most general Lagrangian is given by,

$$\mathcal{L} = \mathcal{L}_4|_{m_N = m_\chi = 0} + (\partial_\mu\sigma)^*(\partial^\mu\sigma) - V(\sigma, H) - \left[f\overline{N_R^c}N_R\sigma + y\overline{\chi_L}\chi_L^c\sigma + \text{H.c.}\right], \tag{5.33}$$

  with,

$$V(\sigma, H) = m_\sigma^2|\sigma|^2 + \lambda_{\sigma H}|\sigma|^2|H|^2 + \lambda_\sigma|\sigma|^4\,. \tag{5.34}$$

---

[15] The operators $(\overline{N_R^c}N_R)(\overline{N_R^c}N_R)$ and $(\overline{\chi_L^c}\chi_L)(\overline{\chi_L^c}\chi_L)$ vanish because we have considered only one generation of N_R and χ_L.

[16] In the considered parameter space the DM self-interactions $\chi\chi \leftrightarrow \chi\chi$ are negligible, with $\sigma_{\chi\chi\to\chi\chi}/m_\chi \lesssim 10^{-6}\,\text{cm}^2/\text{g}$, compared to the current limits [176].

In this case the couplings f and y are in general real. When the scalar σ acquires a VEV, v_σ, and so lepton number is spontaneously broken, Majorana masses $m_N = \sqrt{2} f v_\sigma$ and $m_\chi = \sqrt{2} y v_\sigma$ appear for the fermions of the DS. In this manner, there is a Goldstone boson J, the Majoron in this case, and we should parameterize the scalar as[17]

$$\sigma = \frac{1}{\sqrt{2}} \left(v_\sigma + s \right) e^{iJ/v_\sigma} \,, \tag{5.35}$$

in order to integrate out the radial excitation s ($m_s \gg m_\chi, v_h$). Before EWSB the portal operators $\mathcal{O}_{2,3}$ are,[18]

$$\mathcal{L}_6 = -\frac{fy}{m_s^2} \mathcal{O}_2 + \frac{fy}{2m_s^2} \mathcal{O}_3 + \text{H.c.} \,. \tag{5.36}$$

This model has been analyzed in detail in Ref. [177].

- **Vector mediator**
  The mediator is considered to be a heavy neutral vector boson, Z'_μ. This case should be viewed as an effective set up of a more complete UV model with Z'_μ being the gauge boson of a local symmetry, e.g. see Model C2 in Ref. [4]. The Lagrangian is expressed as,

$$\begin{aligned} \mathcal{L} = \mathcal{L}_4 - \frac{1}{4} Z'_{\mu\nu} Z'^{\mu\nu} + \frac{1}{2} m_{Z'}^2 Z'_\mu Z'^\mu + f \overline{N_R} \gamma^\mu N_R Z'_\mu \\ + y \overline{\chi_L} \gamma^\mu \chi_L Z'_\mu + \delta m^2 Z'_\mu Z^\mu + \epsilon Z'_{\mu,\nu} B^{\mu,\nu} \,, \end{aligned} \tag{5.37}$$

where $Z'_{\mu\nu}$ is the corresponding field strength tensor and the couplings f and y are real. Integrating out Z'_μ gives the lepton conserving operator $\mathcal{O}_1$:

$$\mathcal{L}_6 = +\frac{2fy}{m_{Z'}^2} \mathcal{O}_1 \,. \tag{5.38}$$

---

[17] More about this Goldstone boson is mentioned in Ch. 6.

[18] Minimization of the potential leads to the following relation between the masses and the VEV: $m_\sigma^2 = -\lambda_\sigma v_\sigma^2$ and $m_s^2 = 2\lambda_\sigma v_\sigma^2$.

Chapter 6

Dark matter from two scalar singlets

In the model described in Ch. 4, there is a pseudo-Goldstone boson that results from a spontaneous and explicit breaking of the lepton number symmetry. Unfortunately, this scalar is not a good dark matter candidate in the composite scheme because its lifetime is smaller than the age of the Universe. However, this can be solved by making the Yukawa coupling y_ν of the neutrino portal small enough, see Eq. (4.16), relaxing the composite scenario constraints. In this chapter we explore this line of reasoning considering, for simplicity, the simplest model with a pseudo-Goldstone-like particle.

In this manner, we study the dark matter phenomenology of the scenario where a DM candidate emerges from a two-scalar SM-singlet model, charged under a $O(2)$ global symmetry that is spontaneously and explicitly (in different ways) broken, see Ref. [3]. Besides simplifying and organizing the analysis, the choice of different explicit symmetry breaking terms is motivated by their diverse effects on the possible DM phenomenology. This can allow, in some cases, after combining a number of measurements, to identify signatures of specific terms in the scalar potential.

6.1 Introduction to the model

As mentioned in Sec. 1.5, the particle content of the SM does not contain any good dark matter candidate and must be extended. The simplest scenario consists of adding a real scalar SM-singlet ϕ, with a Z_2 discrete symmetry that forbids its decays, see Refs. [89, 178, 179]. The most general Lagrangian for ϕ is

$$V(H,\phi) = m_\phi^2 \phi^2 + \lambda_{H\phi} \left|H\right|^2 \phi^2 + \lambda_\phi \phi^4 \,, \tag{6.1}$$

where the three new couplings are the DM mass term m_ϕ and the quartic terms $\lambda_{H\phi}$, which connect ϕ with the SM (the so-called Higgs portal), and λ_ϕ which controls the self-interactions.

When freeze-out is considered as the path to reproduce the right value of the relic abundance Ωh^2, see Sec. 1.5.2, the Higgs portal coupling is responsible for the pair-annihilation between ϕ and SM particles. In this simple scenario, constraints from the lack of evidence of invisible Higgs boson decays or from DD experiments exclude almost all of the parameter space possible, except for two regions: one is close to the resonance with the Higgs boson $m_\phi \approx m_h/2$, see Fig. 6.1 (left); while the other is for masses $m_\phi > 1\,\mathrm{TeV}$ [180], see Fig. 6.1 (right).

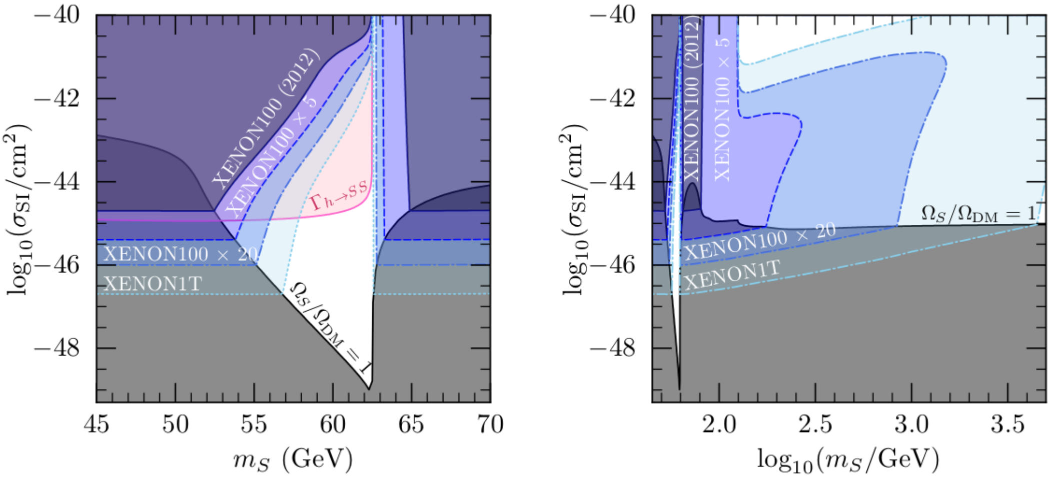

Figure 6.1: Limits from DD on scalar singlet DM, extracted from Ref. [180], shown in a mass and cross section plane. The l.h.s is the close-up of the resonant annihilation region, while in the r.h.s it is the full mass range. The scalar field S in the plot correspond to ϕ in this thesis.

The next simplest extension of the SM, which is the focus of the chapter, comes from adding a second real SM-singlet scalar with some discrete symmetry that stabilizes the DM candidate [181]. In this manner, our main goal is to find whether it is possible to have a good DM candidate outside the two regions of masses of the simplest scenario.

The most general potential with two real scalar singlets, ϕ_1 and ϕ_2, satisfying the discrete symmetry $(\phi_1 \to \phi_1, \phi_2 \to -\phi_2)$, needed to stabilize the DM and dubbed *dark CP symmetry* (DCP), can be described as,[1]

$$V(H,\phi_1,\phi_2) = V_0 + V_{\rm I} + V_{\rm II} + V_{\rm III} + V_{\rm IV}\,, \tag{6.2}$$

with

$$\begin{aligned} V_0 = \frac{|H|^2}{2}\lambda_{HS}(\phi_1^2+\phi_2^2) + m_S^2(\phi_1^2+\phi_2^2) + \lambda_S(\phi_1^2+\phi_2^2)^2\,,\\ V_{\rm I} &= \mu^3\phi_1 + \mu_{H1}|H|^2\phi_1\,,\\ V_{\rm II} &= \mu_S^2\left(\phi_1^2-\phi_2^2\right) + \lambda_{H2}|H|^2\left(\phi_1^2-\phi_2^2\right)\,,\\ V_{\rm III} &= (\mu_3+\mu_1)\phi_1^3 + (-3\mu_3+\mu_1)\phi_1\phi_2^2\,,\\ V_{\rm IV} &= (\lambda_4+\lambda_2)\phi_1^4 - 6\lambda_4\phi_1^2\phi_2^2 + (\lambda_4-\lambda_2)\phi_2^4\,. \end{aligned} \tag{6.3}$$

V_0 is invariant under $O(2)$ rotations in the DS fields (ϕ_1 and ϕ_2) and V_k contains the breaking terms with k number of fields of the DS.

When $O(2)$ is exact, that is if $\langle\phi_1\rangle = 0$ and $V_{I,\ldots,IV} = 0$, ϕ_1 and ϕ_2 are degenerate and the model is like twice the simplest Higgs portal case. If the symmetry is spontaneously broken ($\langle\phi_1\rangle \neq 0$) there is a Goldstone boson which has only derivative couplings. This makes it a good DM candidate because the interactions are relatively weak at low energies, thus easily evading DD constraints, while strong at high energies when the DM should acquire the right relic abundance. However this is not enough since the potential DM particle would be massless. Hence an explicit breaking of the symmetry is needed in order to have a pseudo-Goldstone boson. Likewise, explicit breaking, without SSB, is also not enough to extend the simplest Higgs portal case.

In summary, both spontaneous and explicit symmetry breakings are needed. Notice that the DCP is not broken by ϕ_1 acquiring a VEV and the stability of the DM is preserved.

Mapping model parameters to physical variables

We will parametrize the scalars as

$$H = \frac{1}{\sqrt{2}}\begin{pmatrix} 0 \\ v_h + h' \end{pmatrix}\,, \quad \phi_1 = \frac{1}{\sqrt{2}}\left(v_s + \rho'\right)\,. \tag{6.4}$$

We use the minimization equations on h' and ρ' in Eq. (6.2) to express the bare

---

[1] In the model, we require stability of the dark matter by considering a discrete symmetry and avoid the difficulties from satisfying the constraints on the lifetime, see Refs. [136, 137].

mass parameters in terms of the couplings and VEVs,

$$\begin{aligned}
-m_H^2 &= \frac{1}{2}(\lambda_{H2} + \lambda_{HS})v_s^2 + \lambda_H v_h^2 + \frac{\sqrt{2}}{2}\mu_{H1} v_s\,, \\
-m_S^2 &= \mu_S^2 + (\lambda_2 + \lambda_S + \lambda_4)v_s^2 + \frac{1}{2}(\lambda_{H2} + \lambda_{HS})v_h^2 + \frac{\sqrt{2}}{4}\mu_{H1}\left(\frac{v_h}{v_s}\right)v_h \\
&\quad + \frac{3\sqrt{2}}{4}(\mu_1 + \mu_3)v_s + \frac{\sqrt{2}}{2}\frac{\mu^3}{v_s}\,.
\end{aligned} \tag{6.5}$$

Substituting them back in the potential allows us to compute the mass term of the fields, leading to the following mass matrix in the basis (h',ρ'):

$$M_S^2 = \begin{pmatrix} (M_S^2)_{11} & (M_S^2)_{12} \\ (M_S^2)_{21} & (M_S^2)_{22} \end{pmatrix}\,, \tag{6.6}$$

with the following matrix elements:

$$\begin{aligned}
&(M_S^2)_{11} = 2\lambda_H v_h^2\,, \quad (M_S^2)_{12} = (M_S^2)_{21} = (\lambda_{H2} + \lambda_{HS})\, v_s v_h + \frac{\mu_{H1} v_h}{\sqrt{2}}\,, \\
&(M_S^2)_{22} = 2\,(\lambda_2 + \lambda_S + \lambda_4)\, v_s^2 + \frac{3v_s}{2\sqrt{2}}\,(\mu_1 + \mu_3) - \frac{\mu_{H1} v_h}{2\sqrt{2}}\left(\frac{v_h}{v_s}\right) - \frac{\sqrt{2}\mu^3}{2v_s}\,.
\end{aligned} \tag{6.7}$$

The mass eigenstates will be called h and ρ. The matrix M_S^2 can be diagonalized by an orthogonal rotation of an angle α

$$\begin{pmatrix} h \\ \rho \end{pmatrix} = R\begin{pmatrix} h' \\ \rho' \end{pmatrix}\,, \quad R \equiv \begin{pmatrix} c_\alpha & -s_\alpha \\ s_\alpha & c_\alpha \end{pmatrix}\,, \quad R M_S^2 R^T = \begin{pmatrix} m_h^2 & 0 \\ 0 & m_\rho^2 \end{pmatrix}\,, \tag{6.8}$$

where we defined $s_\alpha = \sin\alpha$ and $c_\alpha = \cos\alpha$ in order to simplify the notation. The eigenstate h is the 125 GeV boson observed at the LHC.[2]

The field ϕ_2, which will be called θ from now on, does not mix with the others because of the DCP symmetry and its mass is

$$m_\theta^2 = -2\mu_S^2 - \frac{\sqrt{2}}{2}\frac{\mu^3}{v_s} - (\lambda_2 + 4\lambda_4)v_s^2 - \lambda_{H2}v_h^2 - \frac{v_s}{2\sqrt{2}}(\mu_1 + 9\mu_3) - \mu_{H1}\frac{v_h}{2\sqrt{2}}\left(\frac{v_h}{v_s}\right)\,, \tag{6.9}$$

which displays the pseudo-Goldstone boson nature of the DM candidate θ, namely, its mass is zero if all the 8 symmetry breaking couplings vanish.

The quartic couplings in V_0 can be expressed in terms of the physical variables associated to the model (the masses m_h, m_ρ and the mixing angle α) and the sym-

---

[2] We consider the mixing $s_\alpha < 0.1$ in the analysis as to satisfy the experimental measurements of the Higgs signal strengths.

metry breaking terms as

$$\begin{aligned}
\lambda_H &= \frac{c_\alpha^2 m_h^2 + s_\alpha^2 m_\rho^2}{2v_h^2}\,,\\
\lambda_S &= \frac{s_\alpha^2 m_h^2 + c_\alpha^2 m_\rho^2}{2v_s^2} - \frac{3}{4\sqrt{2}}\frac{(\mu_1+\mu_3)}{v_s} - (\lambda_2+\lambda_4) + \frac{\mu_{H1}}{4\sqrt{2}v_s}\left(\frac{v_h}{v_s}\right)^2 + \frac{\sqrt{2}}{4}\frac{\mu^3}{v_s^3}\,,\\
\lambda_{HS} &= \frac{s_\alpha c_\alpha(m_\rho^2 - m_h^2)}{v_h v_s} - \frac{\mu_{H1}}{\sqrt{2}v_s} - \lambda_{H2}\,. \qquad (6.10)
\end{aligned}$$

Therefore, the five parameters included in the V_0 potential can be substituted for the five physical variables:

$$m_H,\, m_S,\, \lambda_H,\, \lambda_S,\, \lambda_{HS} \quad \rightarrow \quad v_h,\, m_h,\, v_s,\, m_\rho,\, s_\alpha\,. \qquad (6.11)$$

In the following, we will consider a number of simplified cases where there is only one degree of freedom among the symmetry breaking terms at a time, which will be parameterize in terms of the DM mass m_θ, see Eq. (6.9); and we can study separately their impact in the DM phenomenology. Therefore, each of these models, which we will dub *minimal models*, depends on 6 variables, those in Eq. (6.11) plus m_θ, and four are unknown.

6.2 The minimal models

In a broad manner, the four minimal models we will consider here contain only one power of the fields ϕ_1 and ϕ_2 each (in the breaking sector); therefore, the correspondence among the possible DM phenomenology and the number of powers in the fields will be manifest. Their names will be linear (V_1), quadratic (V_2), cubic (V_3) and quartic (V_4) models corresponding to the power they are related to. In particular, the linear model would induce a VEV for the field ϕ_1, while the quadratic term would contribute only to a splitting in the scalar masses. Cubic and quartic models are different because their symmetry breaking terms generate new interactions among the DM particles (self-interactions), which can have important effects in the generation of the measured relic abundance and the formation of small scale structures in the Universe, see Ref. [176].

The idea then is to spot differences among the models from the DM phenomenology they produce. This could give information in the future, after a positive measurement of DM, of the minimal potential necessary to reproduce the observations.

The symmetry breaking potentials of the minimal models are,

$$\begin{aligned}
V_1 &= \mu^3 \phi_1 \,, \\
V_2 &= \mu_S^2 (\phi_1^2 - \phi_2^2) \,, \\
V_3 &= \mu_3 \left(\phi_1^3 - 3\phi_1\phi_2^2\right) \,, \\
V_4 &= \lambda_4 \left(\phi_1^4 - 6\phi_1^2\phi_2^2 + \phi_2^4\right) \,. \qquad (6.12)
\end{aligned}$$

Notice that the potentials V_1 and V_2 are the most general without the Higgs doublet H and having one and two powers of the fields, respectively. In addition V_3 and V_4 preserved the discrete subgroup of $O(2)$ corresponding to rotations in angles $2\pi/3$ and $2\pi/4$ respectively.

Theoretical and experimental constraints

In the subsequent analysis we have imposed the necessary theoretical constraints on all the models: perturbativity conditions [182], stability of the potential and the global minimum being at $v_h \neq 0$ and $v_s \neq 0$. The co-positivity condition on the matrix of quartic couplings reads [183, 184]

$$\begin{gathered}
\lambda_H > 0 \,, \quad \lambda_S - |\lambda_4| > 0 \,, \quad \lambda_{HS} - |\lambda_{H2}| + 2\sqrt{\lambda_H(\lambda_S + \lambda_4)} > 0 \,, \\
4(\lambda_S - \lambda_4)\sqrt{\lambda_H} + 2(\lambda_{HS} - \lambda_{H2})\sqrt{\lambda_S + \lambda_4} + \sqrt{\lambda_{HR}\lambda_{HI}(\lambda_S - \lambda_4)} > 0 \,, \\
\lambda_{HR} \equiv \lambda_{HS} + \lambda_{H2} + 2\sqrt{\lambda_H(\lambda_S + \lambda_4)} > 0 \,, \\
\lambda_{HI} \equiv \lambda_{HS} - \lambda_{H2} + 2\sqrt{\lambda_H(\lambda_S + \lambda_4)} > 0 \,. \qquad (6.13)
\end{gathered}$$

In the minimal models, the general expressions for λ_H, λ_S and λ_{HS} from Eq. (6.10) are:

$$\lambda_H = \frac{c_\alpha^2 m_h^2 + s_\alpha^2 m_\rho^2}{2v_h^2} \,, \quad \lambda_{HS} = \frac{s_\alpha c_\alpha (m_\rho^2 - m_h^2)}{v_h v_s} \,, \quad \lambda_S = \frac{1}{2v_s^2}\left(s_\alpha^2 m_h^2 + c_\alpha^2 m_\rho^2 + A\, m_\theta^2\right) \,, \qquad (6.14)$$

with $A = -1,\, 0,\, 1/3,\, 1/2$ in the linear, quadratic, cubic and quartic models respectively. In the linear model, the condition for $\lambda_S > 0$ reads $m_\theta^2 \lesssim m_\rho^2$; while for the rest of the models it is satisfied automatically.

With respect to DD constraints, see Sec.1.5.1, tree-level contributions to the scatterings of DM with nuclei appear in the minimal models because of the non-zero mixing between the CP-even scalars. In the Goldstone boson limit, these scatterings are suppressed by the small momentum transfer and therefore they should be proportional to the symmetry breaking terms in the minimal models, or, in what it translates to: m_θ. Following the analysis presented in Refs. [182, 185], the spin-independent DD cross section at tree-level is given by

$$\frac{d\sigma_{SI}}{d\Omega} = \frac{\lambda_{SI}^2\, f_N^2\, m_N^2}{16\pi^2\, m_\theta^2}\left(\frac{m_\theta\, m_N}{m_\theta + m_N}\right)^2 , \tag{6.15}$$

where $m_N = 0.939\,\mathrm{GeV}$ is the nucleon mass and $f_N = 0.3$ is the effective Higgs-nucleon coupling [180]. The effective DM-nucleon coupling λ_{SI} reads as

$$\lambda_{SI}^2 \equiv \frac{1}{4f_N^2 m_N^4}|\mathcal{M}|^2 = \frac{1}{4m_N^2 v_h^2}\left(\frac{\beta_{h\theta\theta}\, c_\alpha}{t - m_h^2} + \frac{\beta_{\rho\theta\theta}\, s_\alpha}{t - m_\rho^2}\right)^2 (4m_N^2 - t)\,, \tag{6.16}$$

and the β_{ijk} coefficients describe the interactions in the Lagrangian among the fields (i, j, k) and are defined in Tab. D.1.

One can see that in the zero momentum limit ($t \to 0$), the effective coupling goes as

$$\lambda_{SI} \propto -\left(\frac{\beta_{h\theta\theta}\, c_\alpha}{m_h^2} + \frac{\beta_{\rho\theta\theta}\, s_\alpha}{m_\rho^2}\right) . \tag{6.17}$$

The expressions of the effective coupling for the minimal models in the small momentum limit are presented in Tab. 6.1. Differences among the minimal models are expected, which help to distinguish the models in direct detection signals. Unfortunately, because the cross section depends on the square of λ_{SI}, there will be no difference between the linear and cubic models. In the quartic model the effective coupling is two times larger than the previous, while in the quadratic model it vanishes.[3]

Minimal model	$\lambda_{SI} \propto -\left(\frac{\beta_{h\theta\theta}\, c_\alpha}{m_h^2} + \frac{\beta_{\rho\theta\theta}\, s_\alpha}{m_\rho^2}\right)$
Linear	$\frac{s_\alpha c_\alpha}{v_s m_h^2 m_\rho^2} m_\theta^2 (m_h^2 - m_\rho^2)$
Quadratic	0
Cubic	$-\frac{s_\alpha c_\alpha}{v_s m_h^2 m_\rho^2} m_\theta^2 (m_h^2 - m_\rho^2)$
Quartic	$-2\frac{s_\alpha c_\alpha}{v_s m_h^2 m_\rho^2} m_\theta^2 (m_h^2 - m_\rho^2)$

Table 6.1: Effective DM-nucleon coupling that enters in the DD cross section in terms of the physical parameters defined in Sec. 6.1.

The DD constraint from XENON1T [190] has been included in the analysis by rescaling the experimental bound with the values of Ωh^2 obtained at each point in

---

[3] Contributions coming from one-loop diagrams are dominant in some particular points of the parameter space, where cancellations at tree-level occur [182, 186–189]. However, in general, we will assume that the tree-level contributions are the dominant in order to simplify the analysis.

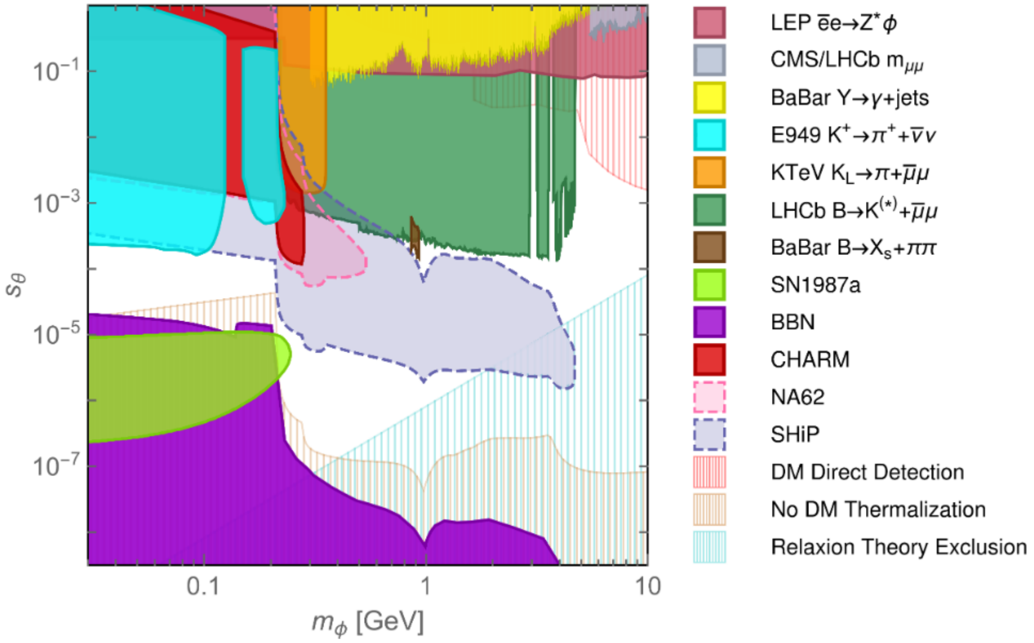

Figure 6.2: Constraints on the mixing angle s_θ between a light scalar field, ϕ, and the Higgs boson in the MeV-GeV mass window. Model-independent constraints were set by the filled regions with solid boundaries, while sensitivity projections by the dashed boundary. The hatched regions are model-dependent exclusions areas. Details can be found in the original work in Ref. [191].

the parameter space analyzed. The bound is read as

$$\frac{\Omega}{\Omega_{\rm obs}} \sigma_{SI} \leqslant \sigma^{\rm XENON1T} , \tag{6.18}$$

where $\sigma^{\rm XENON1T}$ is the 90% CL upper limit on the DM-nucleon spin-independent cross section from XENON1T.

Constraints on the mixing angle with the Higgs boson are taken from Ref. [191] and displayed in Fig. 6.2.

6.3 Scenarios for DM candidates

In this section, we consider the generation of the DM abundance from the non-relativistic case of the freeze-out mechanism, see Sec 1.5.2. In doing so, we assume the real scalar singlets are in thermal equilibrium with the SM particles in the early Universe, because of the interactions mediated by the Higgs portal coupling, $\lambda_{HS} \neq 0$. The relic abundance is computed using the code `micrOMEGAs` from Ref. [99].

In general, as in the minimal Higgs portal scenario, the final DM relic abundance is too large because the annihilation cross section is very small. Exceptions were found in some parts of the parameter space described below:

- **h-res. and ρ-res.:** Resonances with the Higgs boson h or the scalar ρ, which happen for $2m_\theta \simeq m_h$ or $2m_\theta \simeq m_\rho$ respectively. The relevant process is $\theta\theta \leftrightarrow$ SM SM, see Fig. 6.3 (top panel). The advantages of the resonance enhancement in the annihilation processes are twofold. On one side, it does not need large mixing angles and then it is easier to evade the related experimental constraints, for example, from light scalar mixing with the Higgs boson or invisible Higgs boson decays, see Fig. 6.2. On the other side, the scattering cross section does not acquire the enhancement and could be suppressed by small mixing angles. In this manner, DD contributions could be negligible.

- **SDM:** Direct annihilations into lighter pairs of scalars h and/or ρ, for $m_\theta \gtrsim m_h$ and/or $m_\theta \gtrsim m_\rho$, see Fig. 6.3 (bottom panel). This case is known as secluded dark matter (SDM).

- **FDM:** Direct annihilations into slightly heavier pairs of $hh, h\rho, \rho\rho$, see Fig. 6.3 (bottom panel). This is known as forbidden dark matter (FDM). When the masses of ρ and h are similar, which channel dominates depends on the mixing angle α.

- **non-res h:** Non-resonant Higgs-mediated annihilations into SM states. They mainly happen for DM masses above 100 GeV and at mixing angles s_α larger than in the resonant cases [178, 179], see Fig. 6.3 (top panel).

Thermalization conditions

The thermalization conditions considered here are twofold and require for the two sectors to be in thermal equilibrium at: (i) at least until the freeze-out happens and (ii) some earlier time in the history of the Universe. As mentioned in Sec. 1.5.2, with (i) we make sure there is a common temperature between the two sectors, what enables us to perform the calculations described in Sec. 1.5 [192][4]. On the other hand, (ii) allows us to consider as initial conditions the relativistic equilibrium values, Eq. (1.60), for evolving the number density.

In the parameter space considered in the minimal models we found condition (ii) to be easily satisfied. However, condition (i) needed to be studied carefully at each scenario described in Sec. 6.3 separately, as we describe in what follows.

---

[4] Therefore, we can safely use `micrOMEGAs` for the numerical computations.

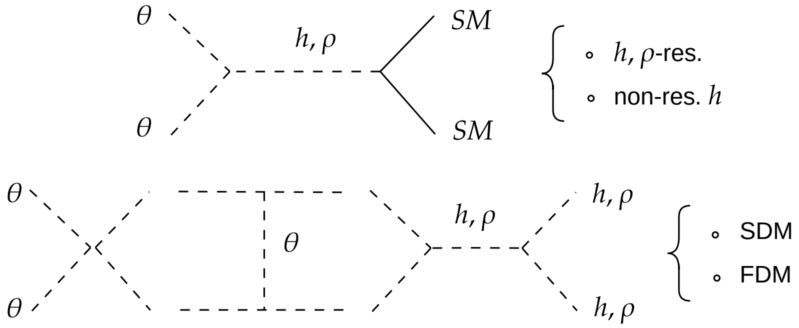

Figure 6.3: Feynman diagrams of the DM annihilation processes: for final states with SM particles mediated by the Higgs boson h and the scalar ρ in the top panel and for final states with only the scalars h and/or ρ particles in the bottom panel.

Refs. [169, 193] found differences in the computation of the relic abundance based on the fact that, in some special circumstances, the kinetic equilibrium might not be maintained until the freeze-out. Consequently the complete calculation would need to take into account the second momentum of the distribution function. These special circumstances included resonances and FDM scenarios. The explanation for the first is based on the fact that the scattering processes would not be enhanced as the related annihilations responsible for the relic abundance.

However, in their computations they did not consider $1 \leftrightarrow 2$ processes and, in fact, this has major implications in the kinetic equilibrium in the resonant scenario. We have seen that for ρ-res., the process $\rho \leftrightarrow \theta\,\theta$ can be responsible for thermalizing the DS, while the processes $\rho \leftrightarrow SM\,SM$ and $\rho\,SM \rightarrow \rho\,SM$ make the connection between the two sectors. In this manner, the scattering $\theta\,SM \rightarrow \theta\,SM$ was not needed in achieving the kinetic equilibrium, even well after the freeze-out happened.

In Fig. 6.4, the regions of parameter space satisfying the condition for the scalar ρ being in thermal equilibrium with the thermal bath are shown in the hatched-brown area, obtained by requiring that the thermal decay rate of the process $\rho \leftrightarrow SM\,SM$ is larger than the Hubble parameter at a temperature $m_\rho/20$.[5]

The detailed analysis of the kinetic equilibrium in the FDM and SDM scenarios is left for a future work and here we assume that there might be small corrections as described in Refs. [169, 193].

---

[5] Furthermore, the region where ρ evades the bounds on the DM lifetime (see e.g. Refs. [136, 137]) and becomes a second dark matter candidate corresponds to mixing angles $s_\alpha \leq 10^{-17}$.

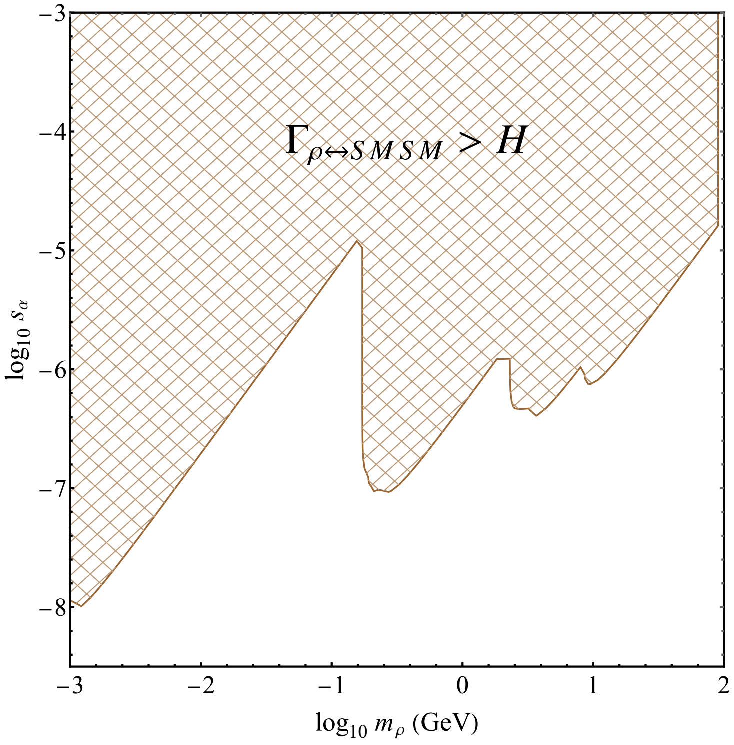

Figure 6.4: Regions of parameter space where the scalar ρ is in thermal equilibrium with the SM particles through the process $\rho \leftrightarrow SM\,SM$ (brown colored region).

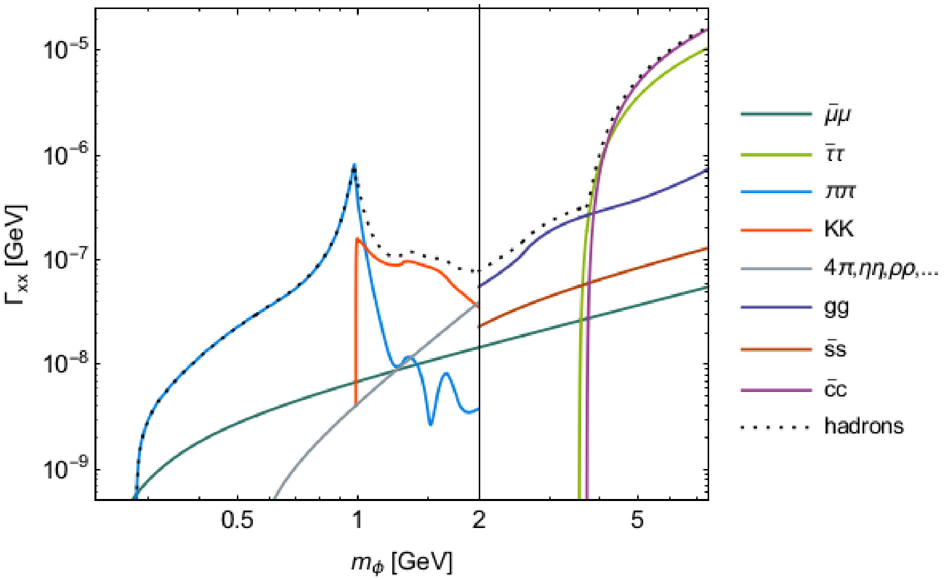

Figure 6.5: Hadronic and leptonic decay rates of a light scalar field, ϕ, that mixes with the Higgs boson. Taken from Ref. [191]. The decay rates Γ_{xx} scale with the squared of the mixing angle and it was set to unity here.

Hadrons as final states

For DM masses below 4-5 GeV and $s_\alpha \neq 0$, mediators decay into mesons and not quarks. The `micrOMEGAs` tool does not consider hadronic final states, so we followed the procedure described in Ref. [180]. The cross section for the ρ-mediated s-channel DM annihilations into hadronic final states is written as

$$\sigma v_{rel} = \frac{4\beta^2_{\rho\theta\theta}}{\sqrt{s}} \, |D_\rho(s)|^2 \, \Gamma_{\rho\to\text{hadrons}}(\sqrt{s}) \, , \tag{6.19}$$

with

$$|D_\rho(s)|^2 = \frac{1}{\left(s - m_\rho^2\right)^2 + m_\rho^2 \Gamma^2_{\rho,\text{full}}\,(m_\rho)} \, . \tag{6.20}$$

The $\beta_{\rho\theta\theta}$ coefficient is given in Tab. D.1. The decay width of ρ going to hadron states, $\Gamma_{\rho\to\text{hadrons}}$, is taken from Fig. 6.5; while the full width of ρ, $\Gamma_{\rho,\text{full}}$, is just $\Gamma_{\rho\to\theta\theta}$, which is the dominant channel in the considered parameter space. This last decay width is written as

$$\Gamma_{\rho\to\theta\theta} = \frac{\beta^2_{\rho\theta\theta}}{32\pi\, m_\rho} \sqrt{1 - \frac{4m_\theta^2}{m_\rho^2}} \, . \tag{6.21}$$

6.4 The resonance scenario

Here we describe the resonance scenario which occurs when $2m_\theta \simeq m_h$ and/or $2m_\theta \simeq m_\rho$. We first discuss in detail one of the minimal models, specifically the quadratic model, to analyze the thermal equilibrium, the appearance of hadrons as final states and the possible light DM in the sub-GeV range. The results obtained in the rest of the minimal models will be shown later.

In the resonance scenario, the relevant annihilation cross section is $\theta\theta \to SM\, SM$ and its value is considerably enhanced near the resonances of the mediator particles: ρ and h. This feature is of importance for sub-GeV and GeV masses of DM because a large cross section with relative small mixing angle is needed in order to reproduce the correct relic abundance while evading constraints. That is why the resonance is a good scenario.

Notice that the scalar mass m_ρ is a free parameter, and so ρ can be taken in resonance with the DM, allowing for DM masses beyond the intervals required in the one-real scalar model, see Fig. 6.1. It seems adequate to parametrize the resonance with the dimensionless mass splitting parameter

$$\Delta = \frac{(m_\rho - m_\theta)}{m_\theta}\,, \tag{6.22}$$

so that $m_\rho = (\Delta + 1)\, m_\theta$.

We depict in Fig. 6.6 the correct relic abundance in the plane of $(m_\theta, \log_{10} s_\alpha)$ with different constant values of Δ and $v_s = 100$ GeV. In the parameter space examined here the most relevant constraints are due to: invisible Higgs boson decays, limits on rare B-meson decays and the condition for thermal equilibrium in the Early Universe. The first one is shown in the blue shaded region, while the orange shaded region is excluded by the limits set on $B \to K\rho \to K$ + "invisible" [115]: ρ decays into an invisible final state composed of two θ. The calculation of the decay rate $B \to K\rho$ was performed using the expressions in Ref. [191].

The features of the red curve in Fig. 6.6 that generates the measured relic abundance can be understood from Fig. 6.5. Below the muon mass m_μ, the DM annihilations can only occur to e^- and e^+, which are very suppressed and a large mixing angle is needed to accommodate the relic abundance. While above m_μ, the kinks are related to the opening of the annihilation channels into different hadronic and leptonic states. At $m_\theta \simeq 60\,\text{GeV}$, the Higgs boson's resonance is clearly visible, with a strong drop in the correct mixing angle values.

Close to the resonance there is a cancellation in the annihilation rate that makes it independent of v_s; consequently, the red curves and thermalization boundary do

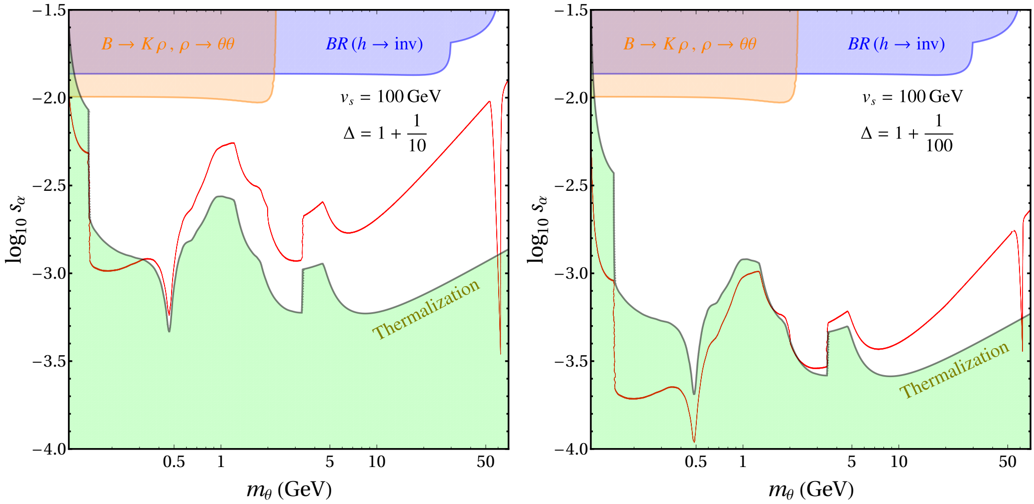

Figure 6.6: The red line shows the relic abundance for the resonance condition with ρ in the quadratic model. We plot different values of $\Delta = 1 + 1/10,\ 1 + 1/100$ on the left and right panels respectively, see Eq. (6.22), with $v_s = 100$ GeV. Experimental constraints from invisible Higgs boson decays (blue), rare B meson decays into light scalars (orange) and the thermalization condition (green) are shown.

not change with v_s. On the other side, the invisible Higgs boson decay limits get weaker for larger values of v_s.

For the sake of comparing the minimal models, we analyze the possibility to distinguish them by finding differences in the parameter space required for a DM candidate. In the resonant scenario, this is done in Fig. 6.7, where all the models are superposed in the same plane of $(m_\theta, \log_{10} s_\alpha)$ and values of Δ as in Fig. 6.6. Two values of the VEV were taken: $v_s = 100\,\mathrm{GeV}$ on the l.h.s and $v_s = 1000\,\mathrm{GeV}$ on the r.h.s. Notice the opening of the channels $\theta\theta \to WW$, ZZ, hh once m_θ is close to the mass threshold m_W, m_Z or m_h.

In summary, the results show that the differences in the mixing angles required to satisfy the correct relic abundance are not significant among the minimal models, and so they can not be disentangled in this scenario.

6.5 Comparison of minimal models

In this section we focus on the comparison of the minimal models and we notice that the best way to present the results is in the plane of Δ and $\log_{10} s_\alpha$, as in Fig. 6.8. A value for the VEV was fixed to $v_s = 100\,\mathrm{GeV}$ and three different illustrative DM masses were chosen $m_\theta = 40, 60, 130\,\mathrm{GeV}$ (from left to right). This way all the

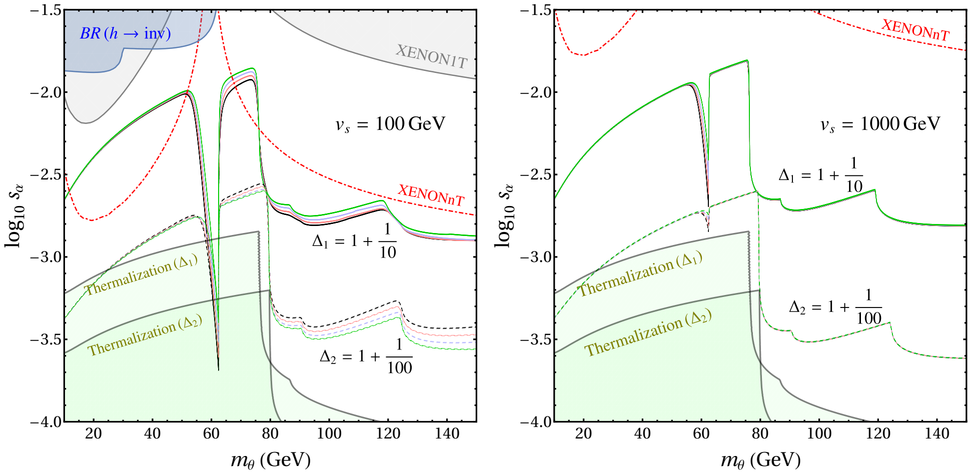

Figure 6.7: Regions of parameter space satisfying the correct value of the measured relic abundance in the ρ resonance. Different values of the mass splitting were taken: $\Delta_1 = 1 + 1/10$ (solid) and $\Delta_2 = 1 + 1/100$ (dashed); and $v_s = 10^2, 10^3$ GeV (left, right). Experimental constraints are shown as follows: invisible Higgs decays by the blue areas, XENON1T experiment [190] by the gray areas, the projection for XENONnT [194] in the red dot-dashed line and the thermalization condition by the green areas. The green, blue, red and black colors correspond to the linear, quadratic, cubic and quartic models, respectively.

freeze-out scenarios discussed in Sec. 6.3 can be spotted in separated regions: h-res. for $m_\theta = 60\,\text{GeV}$ at a fixed mixing angle value, ρ-res. for $\Delta \simeq 1$, FDM for $\Delta \gtrsim 0$, SDM for $\Delta < 0$ and the non-res. h for masses above 100 GeV and s_α larger than in the previous cases. Notice that for the linear model, the correct relic abundance is reached only at the resonances, and it is due to the theoretical constraint $\lambda_S > 0$, which allows only $\Delta > 0$. Therefore, SDM can not be realized in this case.

In Ref. [179], the correct relic abundance was also obtained in what would be our h, ρ-res and non-res h scenarios, as their Fig. 11 shows. Non-res. h can only be seen in the right plot of Fig. 6.8, where the resonant region starts to expand from $\Delta \simeq 1$. Notice how the upper wing tends to become independent on Δ.[6] However, the regions with the correct relic abundance in the FDM and SDM scenarios were not discussed in the mentioned work.

---

[6] The perturbativity constraint $\lambda_S < 4\pi$ has reduced the parameter space in the case of large ρ masses.

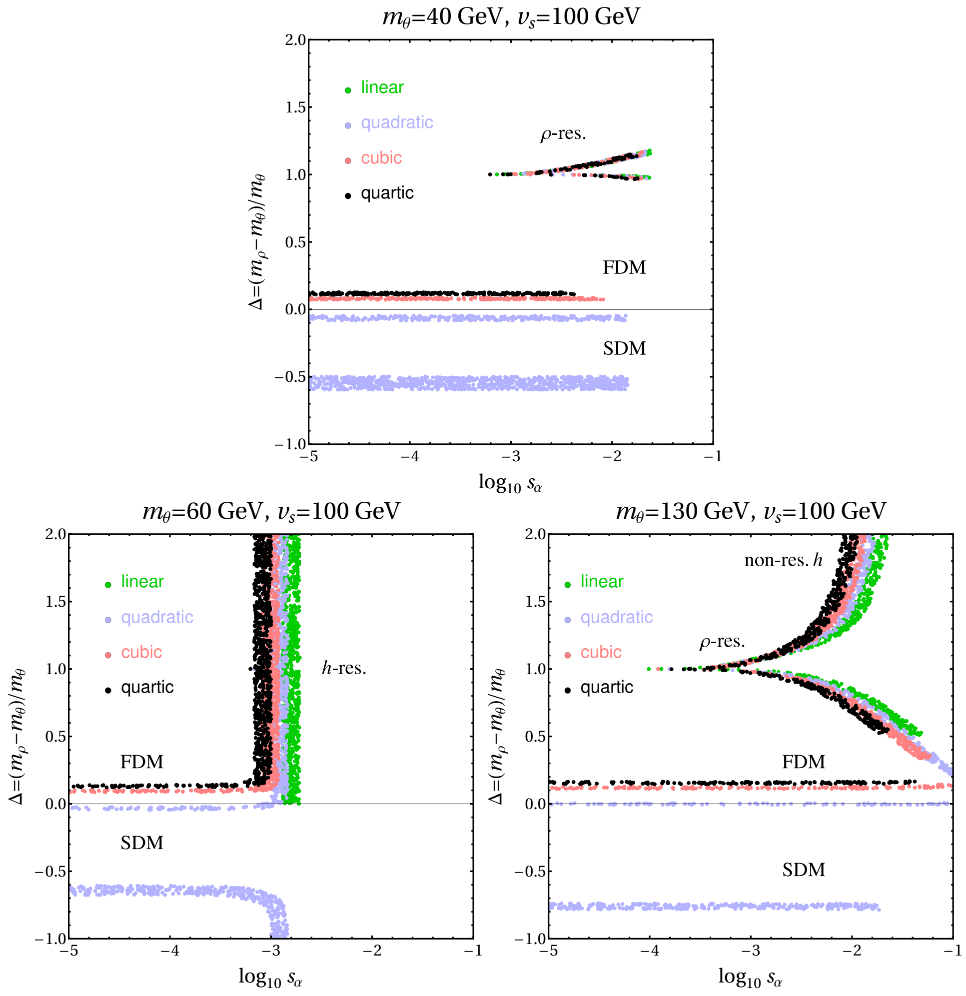

Figure 6.8: Scan in the normalized mass splitting Δ versus the (logarithm of the) mixing s_α for $m_\theta = 40, 60, 130\,\text{GeV}$ from left to right, and $v_s = 100\,\text{GeV}$, for the minimal models described in the text. All these points fulfill the relic abundance condition $0.5 \leqslant \Omega/\Omega_{\text{obs}} \leqslant 1$. We also impose the XENON1T and the invisible Higgs boson decay constraints. Same color-code for the minimal models as in Fig. 6.7.

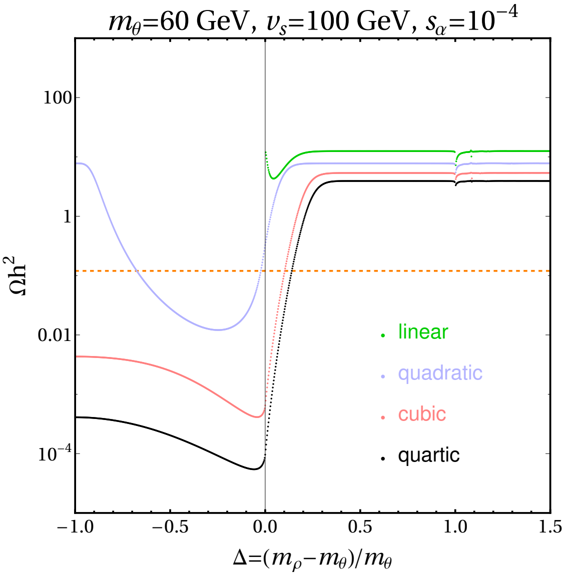

Figure 6.9: Relic abundance as a function of Δ for $m_\theta = 60\,\text{GeV}$, $v_s = 100\,\text{GeV}$ and $s_\alpha = 10^{-4}$ for the minimal models. The correct value for the relic abundance is shown as an orange dashed line.

From Fig. 6.8, it is also evident the lack of differences among the minimal models in the resonance scenarios, ρ-res. and h-res., as concluded in the previous section, and in the non-resonant Higgs-mediated case, non-res. h. On the contrary, in the FDM and SDM there is a clear distinction, so the relic abundance is achieved in different sectors of the parameter space (different strips in the plots). To look into it deeper, in Fig. 6.9 we plot the resulting Ωh^2 values as a function of Δ for fixed values of the rest of the physical variables, in a way to better understand the structure of the strips. We observe that for the case of FDM, close to $\Delta \gtrsim 0$, the linear model does not reach a cross section large enough in order to have the correct relic abundance. This is due to a partial cancellation among the diagrams, which can be glimpsed in the sign difference in Eq. (6.10) of the contribution to λ_S of μ^3, with respect to the μ_3 or λ_4 one. Conversely in the quadratic model, for $\Delta < 0$ the SDM is allowed for two different values of the mass splitting. This can be understood from the two possible contributions to the amplitude for the DM annihilations into ρ: one is proportional to m_ρ and the other one to m_θ, however in the quadratic model only the former is present, so when $m_\rho \to 0$ the amplitude is negligible at tree level.[7]

The previous observations can also be seen in Fig. 6.10, where the normalized mass splitting versus the VEV v_s for the minimal models is plotted. It is important

---

[7] The values of Ωh^2 close to $\Delta = -1$ displayed in Fig. 6.9 should not be trusted as the amplitude of the annihilation $\theta\,\theta \to \rho\,\rho$ goes to zero.

to notice that the SDM scenario can also be present in the cubic and quartic models if the value of v_s is increased.

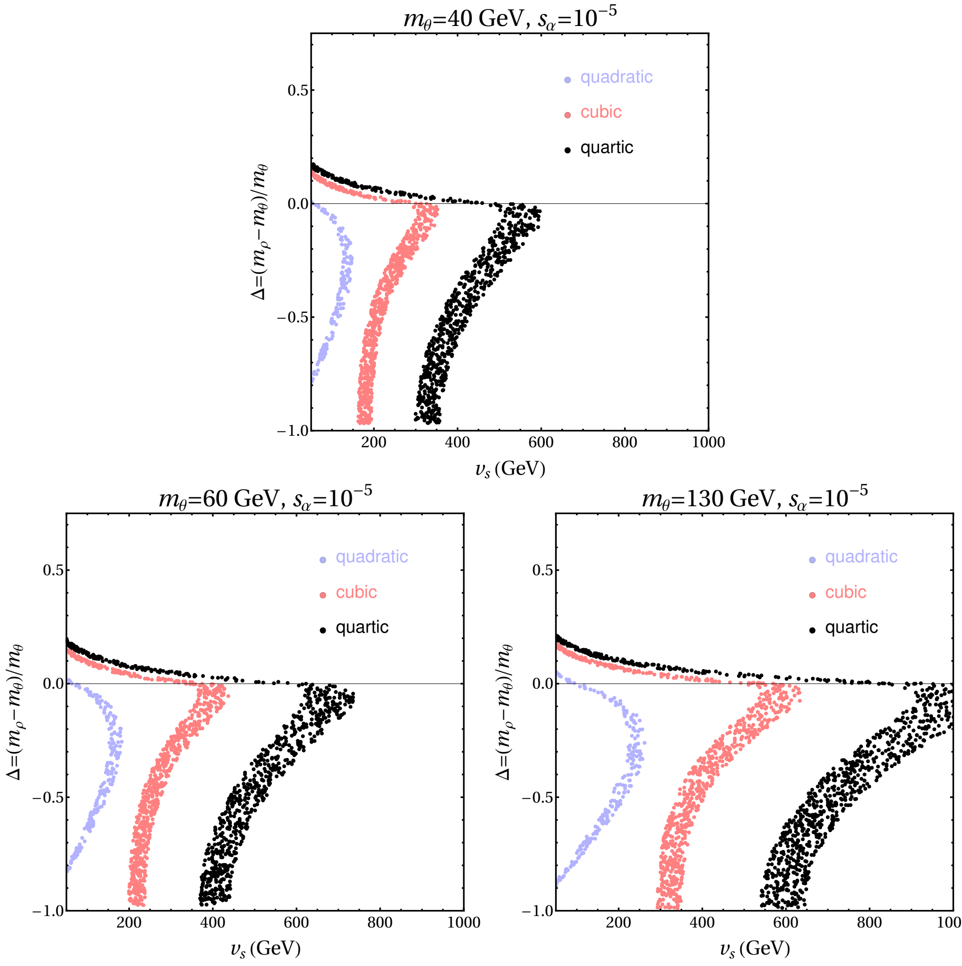

Figure 6.10: Scan in the plane (Δ,v_s) for fixed values of m_θ and s_α. The points fulfill the condition $0.5 \leqslant \Omega/\Omega_{\rm obs} \leqslant 1$. Constraints from XENON1T and the invisible Higgs boson decays were imposed. The color-code is as in Fig. 6.8.

In Fig. 6.11, we show the results of a scan in the parameters $s_\alpha \,\epsilon\, [10^{-5}, 10^{-1}]$ and $m_\theta \,\epsilon\, [10, 1000]$ GeV, for fixed $v_s = 100$ GeV and Δ (FDM, $\Delta = 0.1$; ρ resonance $\Delta = 1.1$) and keeping only the points satisfying $0.5 \leqslant \Omega/\Omega_{\rm obs} \leqslant 1$ at each minimal model.[8] Remember that for the quadratic model, in the zero-momentum limit, there is an exact cancellation at tree level in the DD cross section (see Tab. 6.1). Hence, the dominant contribution is at 1-loop level and it is very suppressed.

---

[8] We do not show the case of SDM ($\Delta = -0.1$, for instance) because in the parameter space considered the DM is under-abundant.

It is important to mention that in the FDM region ($\Delta = 0.1$), a sufficiently precise positive measurement of a DD signal could allow to distinguish the minimal models. On the contrary, in the resonance ($\Delta = 1.1$) this is not possible.

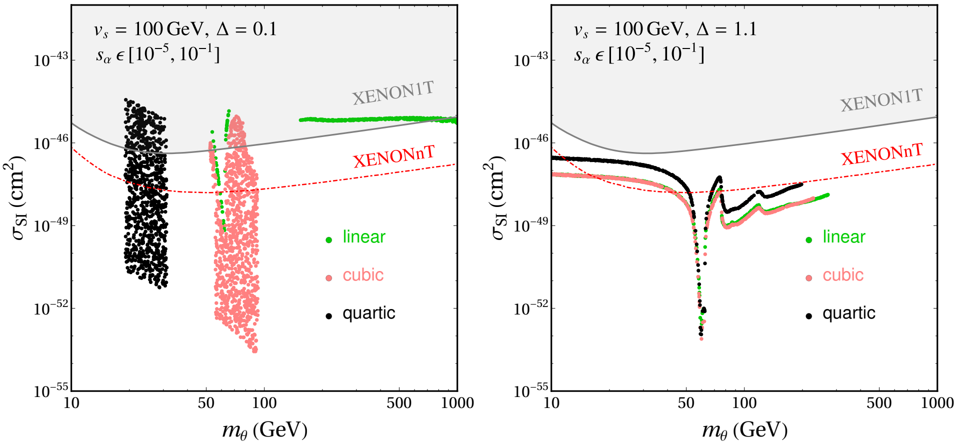

Figure 6.11: Scan in the rescaled spin-independent DD cross section signal for the minimal models versus the DM mass, for mixing in the range $s_\alpha \,\epsilon\, [10^{-5},\, 10^{-1}]$, and fixed values $v_s = 100\,\text{GeV}$ and $\Delta = 0.1$ (left, FDM) $\Delta = 1.1$ (right, ρ resonance). Constraints from perturbativity and invisible Higgs boson decays have been taken into account. We also plot in gray the exclusion region from the current XENON1T experimental limit [190] and its projection [194] as a red dot-dashed line.

With regard to ID bounds [195], we found a different temperature dependence of the annihilation cross section in each scenario associated to the measured relic abundance. In the first (ρ-res. and h-res.) and forth (non-res. h) scenarios the dependence was very strong and then ID bounds were easily evaded.[9] Contrarily, in the SDM the temperature dependence was subtle and a careful study is needed along the parameter space, for an example see Sec. 6.6. Finally, FDM is not constrained from ID measurements as the DM annihilations at zero temperature are absent.

We also studied self-interactions in the minimal models, as a way to distinguish the models, specially in the cubic and quartic cases. The self-interaction cross sections of DM particles, $\sigma_{\theta\theta\to\theta\theta}/m_\theta$, should be in the interval from 0.1 to $1\,g/cm^2$ to explain some features in between dwarf and cluster scales, for a review see e.g. Ref. [176]. The predictions in the minimal models could reach the mentioned values only at the resonances in the analyzed parameter space ($m_\theta < 200\,\text{GeV}$), and they were found to be velocity independent. Due to this, the minimal models could not be disentangled nor explain fully the small scale structure issues on dwarf galaxies.

---

[9] A similar characteristic was also found in the quadratic model in Ref. [178].

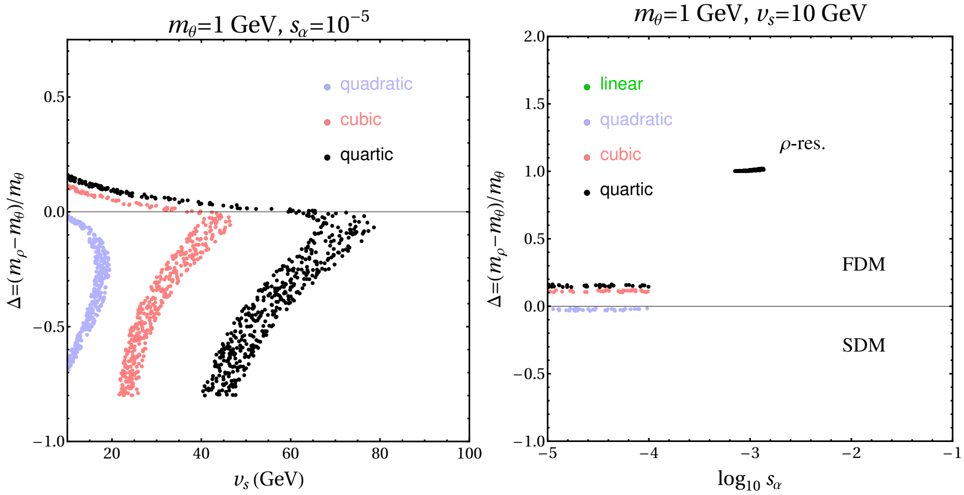

Figure 6.12: Scan in Δ and v_s (s_α) with fixed $m_\theta = 1$ GeV and $s_\alpha = 10^{-5}$ ($v_s =$ 10 GeV) for the minimal models on the left (right) panel. Constraints from light scalars that mix the Higgs boson, Fermi-LAT and invisible Higgs boson decay have been taken into account. All the points fulfill the relic abundance condition $0.5 \leqslant \Omega/\Omega_{\text{obs}} \leqslant 1$.

6.6 Light dark matter

Here we analyze light DM at the sub-GeV scale[10], and in particular the minimum DM mass values, at each minimal model and scenario described in Sec. 6.3. After taking into account constraints from DD experiments, namely CRESST-III and DarkSide-50 [197, 198], and invisible Higgs boson decays, the following points can be made:

- **ρ-res.:** the smallest possible DM mass can be read from Fig. 6.6 and it could be well at the sub-GeV scale. As discussed in Sec. 6.4, especially in Fig. 6.7, it is not easy to disentangle the minimal models in the resonance scenario and so the same lower bound for the DM mass applies to all of them. In particular, constraints on the mixing angle from measurements of meson decays into invisible states ($B \to K\rho$ and $K \to \pi\rho$ [191]) forbid lower values of DM masses.

- **SDM/FDM:** the lightest possible DM has constraints on the mixing angle from the following conditions. First from the limits on light scalars mixing with the Higgs boson as shown in Fig. 6.2. Second, the scalar ρ needs to be in thermal equilibrium with the thermal bath in order to compute the STD

---

[10] Ref. [196] discussed light thermal DM candidates in similar scenarios to the minimal models.

freeze-out method, see Fig. 6.4 and Sec. 5.3. For the SDM case, ID bounds could be important.

For illustrative purposes, we considered $m_\theta = 1$ GeV to perform a scan for the minimal models requiring: $0.5 \leqslant \Omega/\Omega_{\rm obs} \leqslant 1$. The results were plotted in Fig. 6.12 on the plane (Δ,v_s) with $s_\alpha = 10^{-5}$ (left) and on the plane (Δ,s_α) with $v_s = 10$ GeV (right). The invisible Higgs boson decay almost excludes the ρ resonance scenario for $v_s = 10\,\mathrm{GeV}$, while ID bounds from Fermi-LAT [195] forbid SDM when $\Delta \lesssim -0.1$.

Chapter 7

Summary

The Higgs potential in the SM includes mass and quartic self-interaction terms, which are fixed in order to satisfy the electroweak phenomenology. Furthermore, Higgs-fermion-antifermion Yukawa terms are present in the SM to account for the associated interactions and generate the precise values of the fermion masses after the spontaneous breaking of the electroweak symmetry.

However, the fact that the Higgs boson mass is sensitive to new physics scales and the above parameters need to be adjusted at specific values, which span over many orders of magnitude, is somehow undesirable and leads to the open question to whether there is a more fundamental theory beyond the SM. Due to this we hypothesize the Higgs boson as a composite state made of the SM fermions in the scenarios called composite Higgs models. Among this framework's appealing features lies the connection between the dynamical generation of fermions masses and the dynamical origin of EWSB. Moreover we have set ourselves in the subset of models with a $\bar{t}t$ composite with the aim of explaining the masses of the top quark and the Higgs boson at the same time.

The simplest set up for this purpose in the composite scheme is BHL (Bardeen, Hill and Lindner - 1990), which relies on the existence of strong enough four-fermion interactions with the third generation of quarks at some high energy scale Λ, leading to composite effective states at a lower scale. Unfortunately, in this minimal scenario the predictions on the two masses resulted in larger values than the measured ones.

In this manner, with the aim of lowering the predictions for $m_{t,h}$, we have considered two sets of new interactions and/or fundamental particles at the scale Λ. First, we have extended BHL by implementing three four-fermion interactions with different color structures between the third generation of quarks. No new fundamental particles were included in this scenario and composite states of colored triplet, sextet and octet (and $SU(2)_L$-doublet) scalars are formed. These minimal extensions of the SM in colored scalars were motivated by their desirable contributions to the renormalization group equations, which reduce the relevant couplings of the effective theory as well as the final masses.

Regarding the results for m_t, the predictions were larger than the measured values in the colored triplet and sextet cases, although smaller than in BHL, with minimum values for m_t slightly above and below 200 GeV respectively. On the contrary, in the colored octet case values smaller than $m_t = 173$ GeV were obtained even for $\Lambda = 10^8$ GeV. The colored octet was particularly motivated for avoiding flavor violation in the quark sector of the SM, while able to deeply modify the Higgs boson production, EW precision observables and anomalous dipole moments, among other observables.

Concerning m_h, the colored triplet case have led to values similar to those for m_t; unfortunately, the potentials in the colored sextet and octet cases had some subtleties and they will be analyzed elsewhere.

In a second scenario, we have embedded the inverse seesaw mechanism into the composite framework with the addition of new fundamental fermions and four-fermion interactions. The purpose of this set up was to improve HK (Hill and Krog - 2015) and Martin's (Martin - 1991) models, by naturally lowering the scale of new physics and imposing a composite nature to all the scalar particles.

The new fundamental fields were one generation of right-handed neutrino N and sterile fermion χ, and two forms of four-fermion interactions were assumed: among the extra fields and among the right-handed neutrino with the third generation of leptons and quarks. Hence the model contained two composite states: one is associated with the electroweak symmetries of the SM and the other with lepton number symmetry. Both scalars acquired VEVs and a mixture of the CP-even scalars proceeded generating a mass eigenstate that was identified with the Higgs boson measured in the LHC. A constrained region in the parameter space of Λ and the colored scalar mass was found to reproduce the correct values of $m_{t,h}$ at the same time, while the light neutrino masses were easily adjusted by the Majorana mass of the sterile neutrino.

The aforementioned model have implied the existence of a pseudo-Goldstone boson after SSB of the lepton number, which could serve as a DM candidate given the advantage of avoiding direct and indirect detection constraints. However, the model have led to a 1-loop interaction among the pseudo-Goldstone boson and the SM fermions, allowing its decay when kinetically allowed. Unfortunately, the composite scheme involved large Yukawa couplings and decay width, which excluded this scenario because, for example, of constraints on the dark matter lifetime being larger than ten times the age of the Universe.

Consequently, we have examined if four-fermion interactions between the same two extra fermions could lead to χ being a good DM candidate outside of the composite scheme. This connection between a DM particle and neutrinos was an appealing feature for answering two of the main open questions in physics. Moreover the stringent constraints on the interactions between the visible and dark sectors have provided a reason for considering the N as the portal to DM, called sterile neutrino portal.

In this manner, we have explored the possibility for the fermion χ to be the DM candidate, while requiring a discrete Z_2 symmetry that rendered it as stable. In the analysis we have considered the freeze-out mechanism to generate the correct relic abundance of DM, and simultaneously we looked for the annihilation $\chi\,\chi \to N\,N$ to be the main process.

We have found three independent four-fermion interactions when considering only one generation of fermions, and we have proceeded to analyze the models where these operators are generated after integrating out some heavy scalar field. These models were separated based on the nature of the mediator, being a real/complex heavy scalar field, in either t-channel or s-channel, or a heavy vector field. We have studied in some detail the phenomenology in the complex scalar cases, which were further separated in the t-channel in three scenarios, AI-III, depending on which terms in the general Lagrangian were kept. It was interesting to find that the masses of the scalar and χ tend to approach each other to satisfy the measured relic abundance of DM. We have also discussed when it was possible to extrapolate the results to the real scalar case.

After considering all the theoretical and experimental constraints in the models, the results in the t-channel have showed that a good DM candidate was possible in the regions of $100\,\mathrm{GeV} \lesssim m_\chi \lesssim 300\,\mathrm{GeV}$ and $200\,\mathrm{GeV} \lesssim m_\sigma \lesssim 300\,\mathrm{GeV}$ for models AII and AIII, and for $100\,\mathrm{GeV} \lesssim m_\chi \lesssim 800\,\mathrm{GeV}$ and $300\,\mathrm{GeV} \lesssim m_\theta \lesssim 800\,\mathrm{GeV}$ for model AI. While in the s-channel the masses expanded to $2\,\mathrm{GeV} \lesssim m_\chi \lesssim 10\,\mathrm{TeV}$ and $2\,\mathrm{GeV} \lesssim m_\phi \lesssim 20\,\mathrm{TeV}$ or to $30\,\mathrm{GeV} \lesssim m_\chi \lesssim 50\,\mathrm{TeV}$ and $1\,\mathrm{TeV} \lesssim m_\phi \lesssim 100\,\mathrm{TeV}$ depending whether the Yukawa coupling was taken purely real or imaginary, respectively. The fields σ, θ and ϕ correspond to the heavy scalar fields of the models.

We have also analyzed the differences in the results in computing the relic abundance of DM using the full set of Boltzmann equations and the approach we called standard. In doing so we have examined the relevance of the $1 \leftrightarrow 2$ processes and the effect of letting all the particles in the dark sector to evolve out of the thermal equilibrium like the DM. It was found that the first acted as a restoring agent towards equilibrium, while the second brought instability to the system's evolution. In summary, the differences in the relic abundance from the two approaches were below the $10\,\%$ in almost all of the parameter space, except for $m_\chi \sim m_\theta$ and $m_\chi \sim m_N$.

On the other hand, the second model mentioned in the composite scheme served as motivation for studying whether a pseudo-Goldstone boson could in fact be a good dark matter candidate outside of the composite approach, by requiring the Yukawa coupling of the neutrino portal to be small enough.

We have explored the simplest model with a pseudo-Goldstone like particle: the two-scalar SM-singlet model, charged under a $O(2)$ global symmetry that is spontaneously and explicitly broken. We have focused our analysis of the DM phenomenology on four different simplified scenarios with one degree of freedom in the breaking potential, which can be linked to a specific explicit symmetry breaking pattern, that we called minimal models. Namely, the minimal models contained only one power of the extra scalar fields -called linear, quadratic, cubic and quartic models- and therefore a correspondence among the possible DM phenomenology and the number of powers in the fields could become manifest. The pseudo-Goldstone was taken to be stable thanks to a discrete Z_2 symmetry. The purpose was to find regions of parameter space for a good dark matter candidate at each model and, at the same time, compared them with that of the simplest dark matter model, the real SM-singlet scalar case. The correct DM properties were only found in some regions of the parameter space corresponding to the following cases:

- In resonances with the Higgs boson h or the new CP-even scalar ρ.
- In the non-resonant Higgs-mediated annihilations into SM states, when the mixing angle was not constrained to be very small.
- In the secluded dark matter scenario when the h and/or ρ were lighter than the DM.
- In the forbidden dark matter scenario when the h and/or ρ were slightly heavier than the DM.

Due to this, the minimal models were not constrained to the parameter space associated to a good DM particle in the real SM-singlet scalar case. Furthermore, we have sought for possible differences among the minimal models in the regions corresponding to each case mentioned. This was important for understanding the minimal and necessary content in the scalar potential (or the symmetry breaking pattern), after a positive measurement of a DM candidate and the discovery of a new CP-even scalar in the future. The results have showed clear differences in the models only at the last two cases: SDM and FDM; while in the first two the models approximately coincided.

In addition, we have studied light DM candidates in the sub-GeV regime at each model and cases. In the resonance with ρ, DM could be slightly below the GeV scale and lower values were not possible due to constraints on the mixing angle from measurements of meson decays into invisible states. While in the SDM and FDM lower DM masses were possible when the limits on the mixing angle and constraints from ID were evaded. The non-resonant Higgs-mediated annihilations happened only at DM masses larger than 100 GeV, where the mixing angle was allowed to be relatively large.

Bibliography

[1] L. Coito and A. Santamaria, *Top quark mass from a nambu-jona-lasinio higgs with additional composite scalars*, *Work in progress* (2022) .

[2] L. Coito, C. Faubel and A. Santamaria, *Composite Higgs bosons from neutrino condensates in an inverted seesaw scenario*, *Phys. Rev. D* **101** (2020) 075009, [`1912.10001`].

[3] L. Coito, C. Faubel, J. Herrero-Garcia and A. Santamaria, *Dark matter from a complex scalar singlet: the role of dark CP and other discrete symmetries*, *JHEP* **11** (2021) 202, [`2106.05289`].

[4] L. Coito, C. Faubel, J. Herrero-García, A. Santamaria and A. Titov, *Sterile neutrino portals to Majorana dark matter: effective operators and UV completions*, `2203.01946`.

[5] S. L. Glashow, *Partial Symmetries of Weak Interactions*, *Nucl. Phys.* **22** (1961) 579–588.

[6] F. Englert and R. Brout, *Broken Symmetry and the Mass of Gauge Vector Mesons*, *Phys. Rev. Lett.* **13** (1964) 321–323.

[7] P. W. Higgs, *Broken Symmetries and the Masses of Gauge Bosons*, *Phys. Rev. Lett.* **13** (1964) 508–509.

[8] G. S. Guralnik, C. R. Hagen and T. W. B. Kibble, *Global Conservation Laws and Massless Particles*, *Phys. Rev. Lett.* **13** (1964) 585–587.

[9] P. W. Higgs, *Spontaneous Symmetry Breakdown without Massless Bosons*, *Phys. Rev.* **145** (1966) 1156–1163.

[10] S. Weinberg, *A Model of Leptons*, *Phys. Rev. Lett.* **19** (1967) 1264–1266.

[11] A. Salam, *Weak and Electromagnetic Interactions*, *Conf. Proc. C* **680519** (1968) 367–377.

[12] H. Fritzsch and M. Gell-Mann, *Current algebra: Quarks and what else?*, *eConf* **C720906V2** (1972) 135–165, [`hep-ph/0208010`].

[13] M. Gell-Mann, *Quarks*, *Acta Phys. Austriaca Suppl.* **9** (1972) 733–761.

[14] P. W. Higgs, *Broken symmetries, massless particles and gauge fields*, *Phys. Lett.* **12** (1964) 132–133.

[15] L. Susskind, *The gauge hierarchy problem, technicolor, supersymmetry, and all that.*, *Phys. Rept.* **104** (1984) 181–193.

[16] G. F. Giudice, *Beyond the standard model*, in *3rd European School of High-energy Physics*, 5, 1996. `hep-ph/9605390`.

[17] M. Dine, *Naturalness Under Stress*, *Ann. Rev. Nucl. Part. Sci.* **65** (2015) 43–62, [`1501.01035`].

[18] W. A. Bardeen, C. T. Hill and M. Lindner, *Minimal dynamical symmetry breaking of the standard model*, *Physical Review D* **41** (Mar., 1990) 1647–1660.

[19] M. A. Luty, *Dynamical electroweak symmetry breaking with two composite Higgs doublets*, *Physical Review D* **41** (May, 1990) 2893.

[20] Y. Nambu and G. Jona-Lasinio, "Dynamical Model of Elementary Particles Based on an Analogy with Superconductivity I | Broken Symmetry." 10.1142/97898127958230011.

[21] Y. Nambu and G. Jona-Lasinio, *Dynamical Model of Elementary Particles Based on an Analogy with Superconductivity. II*, *Physical Review* **124** (Oct., 1961) 246.

[22] G. Cvetic, *Top quark condensation*, *Rev. Mod. Phys.* **71** (1999) 513–574, [`hep-ph/9702381`].

[23] C. Cowan, F. Reines, F. Harrison, H. Kruse and A. McGuire, *Detection of the free neutrino: A Confirmation*, *Science* **124** (1956) 103–104.

[24] F. Reines, C. Cowan, F. Harrison, A. McGuire and H. Kruse, *Detection of the free anti-neutrino*, *Phys. Rev.* **117** (1960) 159–173.

[25] G. Danby, J. M. Gaillard, K. Goulianos, L. M. Lederman, N. Mistry, M. Schwartz et al., *Observation of high-energy neutrino reactions and the existence of two kinds of neutrinos*, *Physical Review Letters* **9** (1962) 36.

[26] K. Kodama, N. Ushida, C. Andreopoulos, N. Saoulidou, G. Tzanakos, P. Yager et al., *Observation of tau neutrino interactions*, *Physics Letters B* **504** (2001) 218–224.

[27] CMS collaboration, *Precision measurement of the Z boson invisible width in pp collisions at $\sqrt{s} = 13$ TeV*, `2206.07110`.

[28] T. S. Electroweak, H. F. Groups, A. Collaboration, D. Collaboration, L. Collaboration, O. Collaboration et al., *Precision electroweak measurements on the z resonance*, *Physics Reports* **427** (2006) 257–454.

[29] R. Davis, *Solar neutrinos. II: Experimental*, *Phys. Rev. Lett.* **12** (1964) 303–305.

[30] J. N. Bahcall and R. Davis, Jr., *On the Problem of Detecting Solar Neutrinos*, .

[31] J. N. Bahcall, N. A. Bahcall and G. Shaviv, *Present status of the theoretical predictions for the Cl-36 solar neutrino experiment*, *Phys. Rev. Lett.* **20** (1968) 1209–1212.

[32] K. Hirata, A. Mann, M. Takita, W. Frati, K. Takahashi, T. Kajita et al., *Experimental study of the atmospheric neutrino flux*, *Phys. Lett.* **205** (1988) 416.

[33] B. Pontecorvo, *Inverse beta processes and nonconservation of lepton charge*, *Zh. Eksp. Teor. Fiz.* **7** (1957) 247.

[34] B. Pontecorvo, *Neutrino Experiments and the Problem of Conservation of Leptonic Charge*, *Sov. Phys. JETP* **26** (1968) 984–988.

[35] T. Kajita et al., *Atmospheric neutrino results from super-kamiokande and kamiokandeevidence for $\nu\mu$ oscillations*, *Nuclear Physics B-Proceedings Supplements* **77** (1999) 123–132.

[36] S.-K. Collaboration et al., *Y. fukuda et al., evidence for oscillation of atmospheric neutrinos*, *Phys. Rev. Lett* **81** (1998) 1562–1567.

[37] S. Weinberg, *Baryon- and lepton-nonconserving processes*, *Phys. Rev. Lett.* **43** (Nov, 1979) 1566–1570.

[38] S. Weinberg, *Varieties of baryon and lepton nonconservation*, *Phys. Rev. D* **22** (Oct, 1980) 1694–1700.

[39] L. M. Neves Cebola, *Gauge Anomalies and Neutrino Seesaw Models*, Master's thesis, Lisbon, IST, 2013.

[40] P. Minkowski, *$\mu \to e\gamma$ at a Rate of One Out of 10^9 Muon Decays?*, *Phys. Lett.* **67B** (1977) 421–428.

[41] T. Yanagida, *Horizontal Symmetry and Masses of Neutrinos*, in *Proceedings of Workshop on the Unified Theories and the Baryon Number in the Universe, Tsukuba, Japan, February 13–14, 1979*, pp. 95–99, 1979.

[42] P. Ramond, *The Family Group in Grand Unified Theories*, in *International Symposium on Fundamentals of Quantum Theory and Quantum Field Theory, Palm Coast, Florida, United States, 25 February–2 March, 1979*, 1979. `hep-ph/9809459`.

[43] M. Gell-Mann, P. Ramond and R. Slansky, *Complex Spinors and Unified Theories*, in *Proceedings of Supergravity Workshop, Stony Brook, New York, September 27–28, 1979*, pp. 315–321, 1979. `1306.4669`.

[44] S. L. Glashow, *The Future of Elementary Particle Physics*, *NATO Sci. Ser. B* **61** (1980) 687.

[45] R. N. Mohapatra and G. Senjanovic, *Neutrino mass and spontaneous parity nonconservation*, *Phys. Rev. Lett.* **44** (1980) 912.

[46] H. Hettmansperger, M. Lindner and W. Rodejohann, *Phenomenological consequences of sub-leading terms in see-saw formulas*, *Journal of High Energy Physics* **2011** (2011) 123.

[47] W. Grimus and L. Lavoura, *The seesaw mechanism at arbitrary order: disentangling the small scale from the large scale*, *Journal of High Energy Physics* **2000** (Nov, 2000) 042042.

[48] R. N. Mohapatra, *Limits on the mass of the right-handed majorana neutrino*, *Physical Review D* **34** (1986) 909.

[49] R. N. Mohapatra, *Mechanism for Understanding Small Neutrino Mass in Superstring Theories*, *Phys. Rev. Lett.* **56** (1986) 561–563.

[50] R. N. Mohapatra and J. W. F. Valle, *Neutrino Mass and Baryon Number Nonconservation in Superstring Models*, *Phys. Rev.* **D34** (1986) 1642.

[51] D. Wyler and L. Wolfenstein, *Massless Neutrinos in Left-Right Symmetric Models*, *Nucl. Phys.* **B218** (1983) 205–214.

[52] J. Bernabeu, A. Santamaria, J. Vidal, A. Mendez and J. W. F. Valle, *Lepton Flavor Nonconservation at High-Energies in a Superstring Inspired Standard Model*, *Phys. Lett.* **B187** (1987) 303–308.

[53] P. S. B. Dev and A. Pilaftsis, *Minimal radiative neutrino mass mechanism for inverse seesaw models*, *Phys. Rev. D* **86** (Dec, 2012) 113001.

[54] R. M. Wald, *General Relativity.* University of Chicago Press, 1984.

[55] D. Cline, *Sources and detection of dark matter and dark energy in the universe*, .

[56] B. Famaey and S. S. McGaugh, *Modified newtonian dynamics (mond): Observational phenomenology and relativistic extensions*, *Living Reviews in Relativity* (2012) .

[57] M. Milgrom, *A Modification of the Newtonian dynamics as a possible alternative to the hidden mass hypothesis*, *Astrophys. J.* **270** (1983) 365–370.

[58] N. C. Martens and D. Lehmkuhl, *Dark matter=modified gravity? scrutinising the spacetimematter distinction through the modified gravity/ dark matter lens*, *Studies in History and Philosophy of Science Part B: Studies in History and Philosophy of Modern Physics* **72** (2020) 237–250.

[59] P. Villanueva-Domingo, O. Mena and S. Palomares-Ruiz, *A brief review on primordial black holes as dark matter*, *Front. Astron. Space Sci.* **8** (2021) 87, [`2103.12087`].

[60] V. De Romeri, P. Martínez-Miravé and M. Tórtola, *Signatures of primordial black hole dark matter at DUNE and THEIA*, *JCAP* **10** (2021) 051, [`2106.05013`].

[61] D. Aristizabal Sierra, V. De Romeri, L. J. Flores and D. K. Papoulias, *Axionlike particles searches in reactor experiments*, *JHEP* **03** (2021) 294, [`2010.15712`].

[62] D. Papoulias, D. Aristizabal Sierra, V. De Romeri and L. J. Flores, *Probing axion-like particles with reactor neutrino experiments*, *PoS* **NuFact2021** (2022) 090.

[63] D. Aristizabal Sierra, V. De Romeri and D. K. Papoulias, *Consequences of the Dresden-II reactor data for the weak mixing angle and new physics*, `2203.02414`.

[64] M. Schumann, *Direct Detection of WIMP Dark Matter: Concepts and Status*, *J. Phys. G* **46** (2019) 103003, [`1903.03026`].

[65] D. Aristizabal Sierra, N. Rojas and M. H. G. Tytgat, *Neutrino non-standard interactions and dark matter searches with multi-ton scale detectors*, *JHEP* **03** (2018) 197, [`1712.09667`].

[66] D. Aristizabal Sierra, B. Dutta, S. Liao and L. E. Strigari, *Coherent elastic neutrino-nucleus scattering in multi-ton scale dark matter experiments: Classification of vector and scalar interactions new physics signals*, *JHEP* **12** (2019) 124, [`1910.12437`].

[67] R. Bernabei et al., *Final model independent result of DAMA/LIBRA-phase1*, *Eur. Phys. J. C* **73** (2013) 2648, [`1308.5109`].

[68] DAMA, LIBRA collaboration, R. Bernabei et al., *New results from DAMA/LIBRA*, *Eur. Phys. J. C* **67** (2010) 39–49, [`1002.1028`].

[69] DAMA collaboration, R. Bernabei et al., *First results from DAMA/LIBRA and the combined results with DAMA/NaI*, *Eur. Phys. J. C* **56** (2008) 333–355, [`0804.2741`].

[70] R. Bernabei et al., *First model independent results from DAMA/LIBRA-phase2*, *Nucl. Phys. Atom. Energy* **19** (2018) 307–325, [`1805.10486`].

[71] J. Cooley, *Dark Matter direct detection of classical WIMPs*, `2110.02359`.

[72] XMASS collaboration, K. Abe et al., *A direct dark matter search in XMASS-I*, *Phys. Lett. B* **789** (2019) 45–53, [`1804.02180`].

[73] D. S. Akerib et al., *Snowmass2021 Cosmic Frontier Dark Matter Direct Detection to the Neutrino Fog*, in *2022 Snowmass Summer Study*, 3, 2022. `2203.08084`.

[74] K.-Y. Wu and Z.-H. Xiong, *Spin-Dependent Scattering of Scalar and Vector Dark Matter on the Electron*, *Symmetry* **14** (2022) 1061, [`2203.00392`].

[75] J. F. Beacom, N. F. Bell and G. D. Mack, *General Upper Bound on the Dark Matter Total Annihilation Cross Section*, *Phys. Rev. Lett.* **99** (2007) 231301, [`astro-ph/0608090`].

[76] S. Palomares-Ruiz and S. Pascoli, *Testing MeV dark matter with neutrino detectors*, *Phys. Rev. D* **77** (2008) 025025, [`0710.5420`].

[77] C. El Aisati, C. Garcia-Cely, T. Hambye and L. Vanderheyden, *Prospects for discovering a neutrino line induced by dark matter annihilation*, *JCAP* **10** (2017) 021, [`1706.06600`].

[78] A. Olivares-Del Campo, C. Bœhm, S. Palomares-Ruiz and S. Pascoli, *Dark matter-neutrino interactions through the lens of their cosmological implications*, *Phys. Rev. D* **97** (2018) 075039, [`1711.05283`].

[79] C. A. Argüelles, A. Diaz, A. Kheirandish, A. Olivares-Del-Campo, I. Safa and A. C. Vincent, *Dark matter annihilation to neutrinos*, *Rev. Mod. Phys.* **93** (2021) 035007, [`1912.09486`].

[80] S. Basegmez Du Pree, C. Arina, A. Cheek, A. Dekker, M. Chianese and S. Ando, *Robust Limits from Upcoming Neutrino Telescopes and Implications on Minimal Dark Matter Models*, *JCAP* **05** (2021) 054, [`2103.01237`].

[81] Fermi-LAT, DES collaboration, A. Albert et al., *Searching for Dark Matter Annihilation in Recently Discovered Milky Way Satellites with Fermi-LAT*, *Astrophys. J.* **834** (2017) 110, [`1611.03184`].

[82] T. Miener, D. Kerszberg, C. Nigro, J. Rico and D. Nieto, *Open-source Analysis Tools for Multi-instrument Dark Matter Searches*, in *31st Astronomical Data Analysis Software and Systems*, 12, 2021. `2112.01818`.

[83] HESS collaboration, H. Abdallah et al., *Search for γ-Ray Line Signals from Dark Matter Annihilations in the Inner Galactic Halo from 10 Years of Observations with H.E.S.S.*, *Phys. Rev. Lett.* **120** (2018) 201101, [`1805.05741`].

[84] HAWC collaboration, A. Albert et al., *Dark Matter Limits From Dwarf Spheroidal Galaxies with The HAWC Gamma-Ray Observatory*, *Astrophys. J.* **853** (2018) 154, [`1706.01277`].

[85] Fermi-LAT collaboration, E. Charles et al., *Sensitivity Projections for Dark Matter Searches with the Fermi Large Area Telescope*, *Phys. Rept.* **636** (2016) 1–46, [`1605.02016`].

[86] A. Boveia and C. Doglioni, *Dark matter searches at colliders*, *Annual Review of Nuclear and Particle Science* **68** (2018) 429–459.

[87] P. Galison and A. Manohar, *TWO Z's OR NOT TWO Z's?*, *Phys. Lett. B* **136** (1984) 279–283.

[88] B. Holdom, *Two U(1)'s and Epsilon Charge Shifts*, *Phys. Lett. B* **166** (1986) 196–198.

[89] V. Silveira and A. Zee, *SCALAR PHANTOMS*, *Phys. Lett. B* **161** (1985) 136–140.

[90] B. Patt and F. Wilczek, *Higgs-field portal into hidden sectors*, 2006.

[91] M. Pospelov, A. Ritz and M. B. Voloshin, *Secluded WIMP Dark Matter*, *Phys. Lett. B* **662** (2008) 53–61, [`0711.4866`].

[92] M. A. Acero et al., *White Paper on Light Sterile Neutrino Searches and Related Phenomenology*, `2203.07323`.

[93] P. Gondolo and G. Gelmini, *Cosmic abundances of stable particles: Improved analysis*, *Nucl. Phys. B* **360** (1991) 145–179.

[94] E. W. Kolb and M. S. Turner, *The Early Universe*, vol. 69. 1990.

[95] L. Husdal, *On effective degrees of freedom in the early universe*, *Galaxies* **4** (2016) .

[96] D. Baumann, *Primordial Cosmology*, *PoS* **TASI2017** (2018) 009, [`1807.03098`].

[97] J. Bernstein, *KINETIC THEORY IN THE EXPANDING UNIVERSE.* Cambridge Monographs on Mathematical Physics. Cambridge University Press, Cambridge, U.K., 1988, 10.1017/CBO9780511564185.

[98] G. Belanger, F. Boudjema, A. Pukhov and A. Semenov, *MicrOMEGAs: A Program for calculating the relic density in the MSSM*, *Comput. Phys. Commun.* **149** (2002) 103–120, [`hep-ph/0112278`].

[99] G. Bélanger, F. Boudjema, A. Goudelis, A. Pukhov and B. Zaldivar, *micrOMEGAs5.0 : Freeze-in*, *Comput. Phys. Commun.* **231** (2018) 173–186, [`1801.03509`].

[100] C. T. Hill, C. N. Leung and S. Rao, *Renormalization group fixed points and the higgs boson spectrum*, *Nuclear Physics B* **262** (1985) 517–537.

[101] S. P. Martin, *Dynamical electroweak symmetry breaking with top-quark and neutrino condensates*, *Physical Review D* **44** (Nov., 1991) 2892–2898.

[102] A. Smetana, *Top quark and neutrino composite higgs bosons*, *The European Physical Journal C* **73** (2013) 2513.

[103] J. Krog and C. T. Hill, *Is the Higgs boson composed of neutrinos?*, *Physical Review D* **92** (Nov., 2015) 093005.

[104] K. S. Babu and R. N. Mohapatra, *Top-quark mass in a dynamical symmetry-breaking scheme with radiative b-quark and -lepton masses*, *Physical Review Letters* **66** (Feb., 1991) 556–559.

[105] M. Bando, T. Kugo, N. Maekawa, N. Sasakura, Y. Watabiki and K. Suehiro, *Compositeness Condition in Renormalization Group Equation*, *Phys. Lett. B* **246** (1990) 466–470.

[106] M. Suzuki, *Formation of Composite Higgs Bosons From Quark - Anti-quarks at Lower Energy Scales*, *Mod. Phys. Lett.* **A5** (1990) 1205–1212.

[107] M. Bastero-Gil and J. Perez-Mercader, *Composite Higgs and the Reduction of Couplings*, *Phys. Lett. B* **247** (1990) 346–350.

[108] S. H. Mannan and S. F. King, *The Top quark condensate in the presence of higher dimensional operators*, *Int. J. Mod. Phys. A* **6** (1991) 4949–4958.

[109] A. Hasenfratz, P. Hasenfratz, K. Jansen, J. Kuti and Y. Shen, *The Equivalence of the top quark condensate and the elementary Higgs field*, *Nucl. Phys. B* **365** (1991) 79–97.

[110] C. T. Hill, *Topcolor: Top quark condensation in a gauge extension o f the standard model*, *Phys. Lett.* **B266** (1991) 419–424.

[111] M. Lindner, *Top condensates as Higgs substitute*, *Int. J. Mod. Phys.* **A8** (1993) 2167–2240.

[112] K. S. Babu and R. N. Mohapatra, *Top quark mass in a dynamical symmetry breaking scheme with radiative b quark and tau lepton masses*, *Phys. Rev. Lett.* **66** (1991) 556–559.

[113] B. A. Kniehl and O. L. Veretin, *Two-loop electroweak threshold corrections to the botto m and top Yukawa couplings*, *Nucl. Phys.* **B885** (2014) 459–480, [`1401.1844`].

[114] R. Hempfling and B. A. Kniehl, *On the relation between the fermion pole mass and MS Yukawa coupling in the standard model*, *Phys. Rev.* **D51** (1995) 1386–1394, [`hep-ph/9408313`].

[115] Particle Data Group collaboration, P. A. Zyla et al., *Review of Particle Physics*, *PTEP* **2020** (2020) 083C01.

[116] A. V. Manohar and M. B. Wise, *Flavor changing neutral currents, an extended scalar sector, and the Higgs production rate at the CERN LHC*, *Phys. Rev.* **D74** (2006) 035009, [`hep-ph/0606172`].

[117] V. Miralles and A. Pich, *Lhc bounds on colored scalars*, *Phys. Rev. D* **100** (Dec, 2019) 115042.

[118] O. Eberhardt, V. Miralles and A. Pich, *Constraints on coloured scalars from global fits*, *JHEP* **10** (2021) 123, [`2106.12235`].

[119] M. Heikinheimo, K. Kannike, F. Lyonnet, M. Raidal, K. Tuominen and H. Veerme, *Vacuum Stability and Perturbativity of SU(3) Scalars*, *JHEP* **10** (2017) 014, [`1707.08980`].

[120] A. Sirlin and R. Zucchini, *Dependence of the Quartic Coupling H(m) on M(H) and the Possible Onset of New Physics in the Higgs Sector of the Standard Model*, *Nucl. Phys.* **B266** (1986) 389–409.

[121] C. Dib, S. Kovalenko, I. Schmidt and A. Smetana, *Low-scale seesaw from neutrino condensation*, *Nucl.Phys.* **B952** (2020) 114910, [`1904.06280`].

[122] G. Barenboim and C. Bosch, *Composite states of two right-handed neutrinos*, *Phys. Rev.* **D94** (2016) 116019, [`1610.06588`].

[123] G. Barenboim and J. Rasero, *Baryogenesis from a right-handed neutrino condensate*, *JHEP* **03** (2011) 097, [`1009.3024`].

[124] G. Barenboim, *Inflation might be caused by the right: Handed neutrino*, *JHEP* **03** (2009) 102, [`0811.2998`].

[125] F. Del Aguila, J. I. Illana, J. M. Perez-Poyatos and J. Santiago, *Inverse see-saw neutrino masses in the Littlest Higgs model with T-parity*, *JHEP* **12** (2019) 154, [`1910.09569`].

[126] G. B. Gelmini and M. Roncadelli, *Left-Handed Neutrino Mass Scale and Spontaneously Broke n Lepton Number*, *Phys. Lett.* **99B** (1981) 411–415.

[127] S. Bertolini and A. Santamaria, *The Doublet Majoron Model and Solar Neutrino Oscillations*, *Nucl. Phys.* **B310** (1988) 714–742.

[128] Y. Chikashige, R. N. Mohapatra and R. D. Peccei, *Are There Real Goldstone Bosons Associated with Broken Lepton Number?*, *Phys. Lett.* **98B** (1981) 265–268.

[129] C. Dib, S. Kovalenko, I. Schmidt and A. Smetana, *Low-scale seesaw from neutrino condensation*, *AIP Conf. Proc.* **2165** (2019) 020023.

[130] S. Bertolini and A. Santamaria, *The doublet majoron model and solar neutrino oscillations*, *Nuclear Physics B* **310** (1988) 714–742.

[131] N. Rojas, R. A. Lineros and F. Gonzalez-Canales, *Majoron Dark Matter From a Spontaneous Inverse Seesaw Model*, `1703.03416`.

[132] M. C. Gonzalez-Garcia and J. W. F. Valle, *Fast Decaying Neutrinos and Observable Flavor Violation in a New Class of Majoron Models*, *Phys. Lett.* **B216** (1989) 360–366.

[133] V. Berezinsky and J. W. F. Valle, *The KeV majoron as a dark matter particle*, *Phys. Lett. B* **318** (1993) 360–366, [`hep-ph/9309214`].

[134] C. Garcia-Cely and J. Heeck, *Neutrino Lines from Majoron Dark Matter*, *JHEP* **05** (2017) 102, [`1701.07209`].

[135] P.-H. Gu, E. Ma and U. Sarkar, *Pseudo-Majoron as Dark Matter*, *Phys. Lett. B* **690** (2010) 145–148, [`1004.1919`].

[136] S. Palomares-Ruiz, *Model-independent bound on the dark matter lifetime*, *Phys. Lett. B* **665** (2008) 50–53, [`0712.1937`].

[137] K. Ichiki, M. Oguri and K. Takahashi, *Constraints from the wilkinson microwave anisotropy probe on decayingcold dark matter*, *Phys. Rev. Lett.* **93** (Aug, 2004) 071302.

[138] B. Audren, J. Lesgourgues, G. Mangano, P. D. Serpico and T. Tram, *Strongest model-independent bound on the lifetime of Dark Matter*, *JCAP* **12** (2014) 028, [`1407.2418`].

[139] V. Poulin, P. D. Serpico and J. Lesgourgues, *A fresh look at linear cosmological constraints on a decaying dark matter component*, *JCAP* **08** (2016) 036, [`1606.02073`].

[140] K. Enqvist, S. Nadathur, T. Sekiguchi and T. Takahashi, *Constraints on decaying dark matter from weak lensing and cluster counts*, *JCAP* **04** (2020) 015, [`1906.09112`].

[141] A. Nygaard, T. Tram and S. Hannestad, *Updated constraints on decaying cold dark matter*, *JCAP* **05** (2021) 017, [`2011.01632`].

[142] T. Simon, G. Franco Abellán, P. Du, V. Poulin and Y. Tsai, *Constraining decaying dark matter with BOSS data and the effective field theory of large-scale structures*, *Phys. Rev. D* **106** (2022) 023516, [`2203.07440`].

[143] S. Alvi, T. Brinckmann, M. Gerbino, M. Lattanzi and L. Pagano, *Do you smell something decaying? Updated linear constraints on decaying dark matter scenarios*, `2205.05636`.

[144] E. B. Holm, T. Tram and S. Hannestad, *Decaying warm dark matter revisited*, `2205.13628`.

[145] M. Lindner, A. Merle and V. Niro, *Enhancing Dark Matter Annihilation into Neutrinos*, *Phys. Rev. D* **82** (2010) 123529, [`1005.3116`].

[146] A. Ahriche, S. M. Boucenna and S. Nasri, *Dark Radiative Inverse Seesaw Mechanism*, *Phys. Rev. D* **93** (2016) 075036, [`1601.04336`].

[147] S. Bhattacharya, I. de Medeiros Varzielas, B. Karmakar, S. F. King and A. Sil, *Dark side of the Seesaw*, *JHEP* **12** (2018) 007, [`1806.00490`].

[148] C. Pongkitivanichkul, N. Thongyoi and P. Uttayarat, *Inverse seesaw mechanism and portal dark matter*, *Phys. Rev. D* **100** (2019) 035034, [`1905.13224`].

[149] L. Duarte, G. A. González-Sprinberg and O. A. Sampayo, *Majorana neutrinos production at LHeC in an effective approach*, *Phys. Rev. D* **91** (2015) 053007, [`1412.1433`].

[150] M. Duch, B. Grzadkowski and J. Wudka, *Classification of effective operators for interactions between the Standard Model and dark matter*, *JHEP* **05** (2015) 116, [`1412.0520`].

[151] S. M. Boucenna, S. Morisi and J. W. F. Valle, *The low-scale approach to neutrino masses*, *Adv. High Energy Phys.* **2014** (2014) 831598, [`1404.3751`].

[152] E. Ma, *Verifiable radiative seesaw mechanism of neutrino mass and dark matter*, *Phys. Rev.* **D73** (2006) 077301, [`hep-ph/0601225`].

[153] C. Hagedorn, J. Herrero-Garca, E. Molinaro and M. A. Schmidt, *Phenomenology of the Generalised Scotogenic Model with Fermionic Dark Matter*, *JHEP* **11** (2018) 103, [`1804.04117`].

[154] A. Beniwal, J. Herrero-García, N. Leerdam, M. White and A. G. Williams, *The ScotoSinglet Model: a scalar singlet extension of the Scotogenic Model*, *JHEP* **21** (2020) 136, [`2010.05937`].

[155] P. Escribano, M. Reig and A. Vicente, *Generalizing the Scotogenic model*, *JHEP* **07** (2020) 097, [`2004.05172`].

[156] Y. Cai, J. Herrero-Garca, M. A. Schmidt, A. Vicente and R. R. Volkas, *From the trees to the forest: a review of radiative neutrino mass models*, *Front.in Phys.* **5** (2017) 63, [`1706.08524`].

[157] C. Cosme, M. a. Dutra, T. Ma, Y. Wu and L. Yang, *Neutrino Portal to FIMP Dark Matter with an Early Matter Era*, *JHEP* **03** (2021) 026, [`2003.01723`].

[158] R. Coy, A. Gupta and T. Hambye, *Seesaw neutrino determination of the dark matter relic density*, *Phys. Rev. D* **104** (2021) 083024, [`2104.00042`].

[159] M. Becker, *Dark Matter from Freeze-In via the Neutrino Portal*, *Eur. Phys. J. C* **79** (2019) 611, [`1806.08579`].

[160] J. Herrero-Garcia, E. Molinaro and M. A. Schmidt, *Dark matter direct detection of a fermionic singlet at one loop*, *Eur. Phys. J.* **C78** (2018) 471, [`1803.05660`].

[161] B. Batell, T. Han and B. Shams Es Haghi, *Indirect Detection of Neutrino Portal Dark Matter*, *Phys. Rev. D* **97** (2018) 095020, [`1704.08708`].

[162] M. Escudero, N. Rius and V. Sanz, *Sterile Neutrino portal to Dark Matter II: Exact Dark symmetry*, *Eur. Phys. J. C* **77** (2017) 397, [`1607.02373`].

[163] Y.-L. Tang and S.-h. Zhu, *Dark Matter Relic Abundance and Light Sterile Neutrinos*, *JHEP* **01** (2017) 025, [`1609.07841`].

[164] P. Bandyopadhyay, E. J. Chun, R. Mandal and F. S. Queiroz, *Scrutinizing Right-Handed Neutrino Portal Dark Matter With Yukawa Effect*, *Phys. Lett. B* **788** (2019) 530–534, [`1807.05122`].

[165] L. Bian and Y.-L. Tang, *Thermally modified sterile neutrino portal dark matter and gravitational waves from phase transition: The Freeze-in case*, *JHEP* **12** (2018) 006, [`1810.03172`].

[166] P. Bandyopadhyay, E. J. Chun and R. Mandal, *Feeble neutrino portal dark matter at neutrino detectors*, *JCAP* **08** (2020) 019, [`2005.13933`].

[167] A. Berlin, D. Hooper and G. Krnjaic, *Thermal Dark Matter From A Highly Decoupled Sector*, *Phys. Rev. D* **94** (2016) 095019, [`1609.02555`].

[168] T. Binder, T. Bringmann, M. Gustafsson and A. Hryczuk, *DRAKE: Dark matter Relic Abundance beyond Kinetic Equilibrium*, `2103.01944`.

[169] T. Binder, T. Bringmann, M. Gustafsson and A. Hryczuk, *Early kinetic decoupling of dark matter: when the standard way of calculating the thermal relic density fails*, *Phys. Rev. D* **96** (2017) 115010, [`1706.07433`].

[170] T. Hambye and D. Teresi, *Higgs doublet decay as the origin of the baryon asymmetry*, *Phys. Rev. Lett.* **117** (2016) 091801, [`1606.00017`].

[171] M. E. Cabrera, J. A. Casas, A. Delgado and S. Robles, *Generalized Blind Spots for Dark Matter Direct Detection in the 2HDM*, *JHEP* **02** (2020) 166, [`1912.01758`].

[172] M. E. Cabrera, J. A. Casas, A. Delgado and S. Robles, *2HDM singlet portal to dark matter*, *JHEP* **01** (2021) 123, [`2011.09101`].

[173] L. Lopez-Honorez, T. Schwetz and J. Zupan, *Higgs portal, fermionic dark matter, and a Standard Model like Higgs at 125 GeV*, *Phys. Lett. B* **716** (2012) 179–185, [`1203.2064`].

[174] M. A. Fedderke, J.-Y. Chen, E. W. Kolb and L.-T. Wang, *The Fermionic Dark Matter Higgs Portal: an effective field theory approach*, *JHEP* **08** (2014) 122, [`1404.2283`].

[175] GAMBIT collaboration, P. Athron et al., *Global analyses of Higgs portal singlet dark matter models using GAMBIT*, *Eur. Phys. J. C* **79** (2019) 38, [`1808.10465`].

[176] S. Tulin and H.-B. Yu, *Dark Matter Self-interactions and Small Scale Structure*, *Phys. Rept.* **730** (2018) 1–57, [`1705.02358`].

[177] M. Escudero, N. Rius and V. Sanz, *Sterile neutrino portal to Dark Matter I: The* $U(1)_{B-L}$ *case*, *JHEP* **02** (2017) 045, [`1606.01258`].

[178] C. Arina, A. Beniwal, C. Degrande, J. Heisig and A. Scaffidi, *Global fit of pseudo-Nambu-Goldstone Dark Matter*, *JHEP* **04** (2020) 015, [`1912.04008`].

[179] D. Azevedo, M. Duch, B. Grzadkowski, D. Huang, M. Iglicki and R. Santos, *Testing scalar versus vector dark matter*, *Phys. Rev. D* **99** (2019) 015017, [`1808.01598`].

[180] J. M. Cline, K. Kainulainen, P. Scott and C. Weniger, *Update on scalar singlet dark matter*, *Phys. Rev. D* **88** (2013) 055025, [`1306.4710`].

[181] J. McDonald, *Gauge singlet scalars as cold dark matter*, *Phys. Rev. D* **50** (1994) 3637–3649, [`hep-ph/0702143`].

[182] T. Alanne, N. Benincasa, M. Heikinheimo, K. Kannike, V. Keus, N. Koivunen et al., *Pseudo-Goldstone dark matter: gravitational waves and direct-detection blind spots*, *JHEP* **10** (2020) 080, [`2008.09605`].

[183] K. Kannike, *Vacuum Stability Conditions From Copositivity Criteria*, *Eur. Phys. J. C* **72** (2012) 2093, [`1205.3781`].

[184] K. Kannike, *Vacuum Stability of a General Scalar Potential of a Few Fields*, *Eur. Phys. J. C* **76** (2016) 324, [`1603.02680`].

[185] C. Gross, O. Lebedev and T. Toma, *Cancellation Mechanism for Dark-Matter–Nucleon Interaction*, *Phys. Rev. Lett.* **119** (2017) 191801, [`1708.02253`].

[186] S. Abe, G.-C. Cho and K. Mawatari, *Probing a degenerate-scalar scenario in a pseudoscalar dark-matter model*, `2101.04887`.

[187] S. Glaus, M. Mühlleitner, J. Müller, S. Patel, T. Römer and R. Santos, *Electroweak Corrections in a Pseudo-Nambu Goldstone Dark Matter Model Revisited*, *JHEP* **12** (2020) 034, [`2008.12985`].

[188] K. Ishiwata and T. Toma, *Probing pseudo Nambu-Goldstone boson dark matter at loop level*, *JHEP* **12** (2018) 089, [`1810.08139`].

[189] D. Azevedo, M. Duch, B. Grzadkowski, D. Huang, M. Iglicki and R. Santos, *One-loop contribution to dark-matter-nucleon scattering in the pseudo-scalar dark matter model*, *JHEP* **01** (2019) 138, [`1810.06105`].

[190] XENON collaboration, E. Aprile et al., *Dark Matter Search Results from a One Ton-Year Exposure of XENON1T*, *Phys. Rev. Lett.* **121** (2018) 111302, [`1805.12562`].

[191] M. W. Winkler, *Decay and detection of a light scalar boson mixing with the Higgs boson*, *Phys. Rev. D* **99** (2019) 015018, [`1809.01876`].

[192] J. A. Evans, S. Gori and J. Shelton, *Looking for the WIMP Next Door*, *JHEP* **02** (2018) 100, [`1712.03974`].

[193] T. Abe, *The early kinetic decoupling and a pseudo-Nambu Goldstone dark matter model*, `2106.01956`.

[194] XENON collaboration, E. Aprile et al., *Physics reach of the XENON1T dark matter experiment*, *JCAP* **04** (2016) 027, [`1512.07501`].

[195] Fermi-LAT, DES collaboration, A. Albert et al., *Searching for Dark Matter Annihilation in Recently Discovered Milky Way Satellites with Fermi-LAT*, *Astrophys. J.* **834** (2017) 110, [`1611.03184`].

[196] T. Hara, S. Kanemura and T. Katayose, *Is light thermal scalar dark matter possible?*, `2109.03553`.

[197] CRESST collaboration, A. H. Abdelhameed et al., *First results from the CRESST-III low-mass dark matter program*, *Phys. Rev. D* **100** (2019) 102002, [`1904.00498`].

[198] DarkSide collaboration, P. Agnes et al., *Low-Mass Dark Matter Search with the DarkSide-50 Experiment*, *Phys. Rev. Lett.* **121** (2018) 081307, [`1802.06994`].

[199] F. Staub, *SARAH 4: A tool for (not only SUSY) model builders*, *Comput. Phys. Commun.* **185** (2014) 1773–1790, [`1309.7223`].

[200] X.-G. He, H. Phoon, Y. Tang and G. Valencia, *Unitarity and vacuum stability constraints on the couplings of color octet scalars*, *JHEP* **05** (2013) 026, [`1303.4848`].

[201] L. J. Hall, K. Jedamzik, J. March-Russell and S. M. West, *Freeze-In Production of FIMP Dark Matter*, *JHEP* **03** (2010) 080, [`0911.1120`].

[202] V. A. Rubakov and D. S. Gorbunov, *Introduction to the Theory of the Early Universe: Hot big bang theory.* World Scientific, Singapore, 2017, 10.1142/10447.

Appendix A

RGEs for the quartic couplings of colored scalar fields

The RGEs for the colored scalar quartic couplings of Ch. 3 are ($\beta_\epsilon = d\epsilon/d\ln(\mu)$):[1]

- Triplet:

$$\begin{aligned}
16\pi^2\beta_{\lambda_H} =& + 12\lambda_H^2 + 12\lambda_H y_t^2 - 12y_t^4 + 6\lambda_2^2 - 9g_2^2\lambda_H + \frac{27}{100}g_1^4 + \frac{9}{10}g_1^2 g_2^2 \\
& + \frac{9}{4}g_2^4 - \frac{9}{5}g_1^2\lambda_H \,, \\
16\pi^2\beta_{\lambda_2} =& + \frac{3}{25}g_1^4 - \frac{13}{10}g_1^2\lambda_2 - \frac{9}{2}g_2^2\lambda_2 - 8g_3^2\lambda_2 + 6\lambda_H\lambda_2 + 8\lambda_2\lambda_3 + 4\lambda_2^2 \\
& + 16\lambda_2 f_t^2 + 6\lambda_2 y_t^2 - 32h^2 f_t^2 \,, \\
16\pi^2\beta_{\lambda_3} =& - 128 f_t^4 + 14\lambda_3^2 - 16g_3^2\lambda_3 + 32\lambda_3 f_t^2 + 4\lambda_2^2 + \frac{13}{3}g_3^4 - \frac{4}{5}g_1^2\lambda_3 \\
& + \frac{4}{75}g_1^4 + \frac{8}{15}g_1^2 g_3^2 \,.
\end{aligned} \tag{A.1}$$

- Sextet (in agreement with Ref. [119]):

$$\begin{aligned}
16\pi^2\beta_{\lambda_H} =& + 27g_1^4/100 + \left(9g_1^2 g_2^2\right)/10 + \left(9g_2^4\right)/4 - 9g_1^2\lambda_H/5 - 9g_2^2\lambda_H + 12\lambda_H^2 \\
& + 12\lambda_2^2 + 12\lambda_H y_t^2 - 12y_t^4 \,, \\
16\pi^2\beta_{\lambda_2} =& + 48g_1^4/25 - 73g_1^2\lambda_2/10 - 9g_2^2\lambda_2/2 - 20g_3^2\lambda_2 + 6\lambda_H\lambda_2 + 14\lambda_2\lambda_3 + 4\lambda_2^2 \\
& + 4\lambda_2 f_s^2 + 6\lambda_2 y_t^2 - 16f_s^2 y_t^2 \,,
\end{aligned}$$

---

[1] The RGEs are computed in this thesis with the Mathematica package SARAH [199].

$$\begin{aligned}
16\pi^2\beta_{\lambda_3} &= + 8\lambda_3 f_s^2 + 512 g_1^4/75 - 64 g_1^2 \left(2g_3^2 - 3\lambda_3\right)/15 + 35 g_3^4/3 - 40 g_3^2\lambda_3 + 40\lambda_3^2 \\
&\quad + 2\lambda_2^2 + 6\lambda_4^2 + 32\lambda_3\lambda_4 \,, \\
16\pi^2\beta_{\lambda_4} &= + 8\lambda_4 f_s^2 + 128 g_1^2 g_3^2/5 - 64 g_1^2\lambda_4/5 + 5 g_3^4 - 40 g_3^2\lambda_4 + 22\lambda_4^2 \\
&\quad + 24\lambda_3\lambda_4 - 16 f_s^4 \,. \qquad \text{(A.2)}
\end{aligned}$$

- Octet (Yukawa contributions are original for $\beta_{\lambda_{4-11}}$ and the rest are in agreement with Ref. [200]):

$$\begin{aligned}
16\pi^2\beta_{\lambda_H} &= + 2\lambda_H^2 + \lambda_2^2 + 4\lambda_3^2 + 4\lambda_H\left(3\lambda_H + \lambda_2\right) \\
&\quad + \left(+7\lambda_4\lambda_4^* - 2\lambda_4^*\lambda_5 - 2\lambda_5^*\lambda_4 + 7\lambda_5\lambda_5^*\right)/6 \\
&\quad + \lambda_H\left(8\lambda_6 + 8\lambda_7 + 17\lambda_8 + 10\lambda_9 + 3\lambda_{10} + 5\lambda_{11}\right)/2 \\
&\quad + \lambda_2\left(8\lambda_6 + 8\lambda_7 + 24\lambda_8 + 3\lambda_9 + 3\lambda_{10} + 8\lambda_{11}\right)/6 + \lambda_H\left(f_o^2 + 6y_t^2\right) - 4 f_o^2 y_t^2 \,, \\
16\pi^2\beta_{\lambda_2} &= + 2\lambda_2^2 + 4\lambda_H\lambda_2 + 16\lambda_3^2 + 4\lambda_H\lambda_2 \\
&\quad + \left(8\lambda_4\lambda_4^* + 17\lambda_4^*\lambda_5 + 17\lambda_5^*\lambda_4 + 8\lambda_5\lambda_5^*\right)/12 \\
&\quad + \lambda_2\left(16\lambda_6 + 16\lambda_7 + 6\lambda_8 + 48\lambda_9 + 6\lambda_{10} - 2\lambda_{11}\right)/12 + \lambda_2\left(f_o^2 + 6y_t^2\right) - 4 f_o^2 y_t^2 \,, \\
16\pi^2\beta_{\lambda_3} &= + 2\lambda_3\left(2\lambda_H + 3\lambda_2 + 2\lambda_H\right) + \left(17\lambda_4^2 + 16\lambda_4\lambda_5 + 17\lambda_5^2\right)/24 \\
&\quad + \lambda_3\left(-\lambda_6 - \lambda_7 + 3\lambda_8 + 3\lambda_9 + 24\lambda_{10} + 8\lambda_{11}\right)/6 + \lambda_3\left(f_o^2 + 6y_t^2\right) - 2 f_o^2 y_t^2 \,, \\
16\pi^2\beta_{\lambda_4} &= + 8\lambda_4^*\lambda_3 + 2\lambda_3\lambda_5^* + \lambda_5\left(2\lambda_2 - \lambda_7/2 + \lambda_9 + 2\lambda_{10} + \lambda_{11}/2\right) \\
&\quad + \lambda_4\left(3\lambda_H + 2\lambda_2 + 3\lambda_6 + \lambda_7 + 3\lambda_8/2 + \lambda_9 + \lambda_{10}/2 + \lambda_{11}/2\right) \\
&\quad + 3\lambda_4\left(f_o^2/2 + y_t^2\right) - 16 f_o^3 y_t/3 \,, \\
16\pi^2\beta_{\lambda_5} &= + \lambda_4^*\lambda_3 + 4\lambda_3\lambda_5^* + \lambda_4\left(2\lambda_2 - \lambda_6/2 + \lambda_9 + 2\lambda_{10} + \lambda_{11}/2\right) \\
&\quad + \lambda_5\left(3\lambda_H + 2\lambda_2 + 3\lambda_6 + \lambda_7 + 3\lambda_8/2 + \lambda_9 + \lambda_{10}/2 + \lambda_{11}/2\right) \\
&\quad + 3\lambda_5\left(f_o^2/2 + y_t^2\right) - 4 f_o^3 y_t \,, \\
16\pi^2\beta_{\lambda_6} &= + 6\lambda_4\lambda_4^* + 7\lambda_6^2/2 + \lambda_6\left(6\lambda_7 + 6\lambda_8 + 4\lambda_9 - \lambda_{10} - 2\lambda_{11}\right)/2 \\
&\quad + \lambda_7\left(4\lambda_9 - \lambda_{10}\right)/2 - \lambda_9\lambda_{11} + \lambda_{10}\lambda_{11} + \lambda_{11}^2/2 + 2\lambda_6 f_o^2 - 3 f_o^4 \,, \\
16\pi^2\beta_{\lambda_7} &= + 6\lambda_5\lambda_5^*/2 + 7\lambda_7^2/2 + \lambda_7\left(6\lambda_6 + 6\lambda_8 + 4\lambda_9 - \lambda_{10} - 2\lambda_{11}\right)/2 \\
&\quad + \lambda_6\left(4\lambda_9 - \lambda_{10}\right)/2 - \lambda_9\lambda_{11} + \lambda_{10}\lambda_{11} + \lambda_{11}^2/2 + 2\lambda_7 f_o^2 - f_o^4 \,, \\
16\pi^2\beta_{\lambda_8} &= + 10\lambda_8^2 + \lambda_8\left(288\lambda_6 + 288\lambda_7 + 360\lambda_9 + 108\lambda_{10} + 180\lambda_{11}\right)/36 \\
&\quad + \left(36\lambda_H^2 + 36\lambda_H\lambda_2 - 24\lambda_4\lambda_4^* - 6\lambda_4^*\lambda_5 - 6\lambda_5^*\lambda_4 - 24\lambda_5\lambda_5^*\right)/9 \\
&\quad + [62\lambda_6^2 + 64\lambda_6\lambda_7 + 62\lambda_7^2 + 96\lambda_9\left(\lambda_6 + \lambda_7\right) + 18\lambda_{10}\left(\lambda_6 + \lambda_7\right) \\
&\quad + 58\lambda_{11}\left(\lambda_6 + \lambda_7\right) \\
&\quad + 54\lambda_9^2 + 36\lambda_9\lambda_{10} + 132\lambda_9\lambda_{11} + 18\lambda_{10}^2 + 18\lambda_{10}\lambda_{11} + 29\lambda_{11}^2]/36 + 2\lambda_8 f_o^2 \,,
\end{aligned}$$

$$
\begin{aligned}
16\pi^2\beta_{\lambda_9} =& + 2\lambda_2^2 + 8\lambda_9^2 + 4\lambda_{10}^2 - \lambda_{11}^2/9 - \left(2\lambda_4\lambda_4^* - 4\lambda_4^*\lambda_5 - 4\lambda_5^*\lambda_4 + 2\lambda_5\lambda_5^*\right)/3 \\
&+ \lambda_{10}\left(\lambda_6 + \lambda_7 + \lambda_{11}\right)/2 + \lambda_9\left(16\lambda_6/6 + 16\lambda_7/6 + 4\lambda_{11}/6 + \lambda_{10}\right) \\
&+ \big(\lambda_6^2 + 26\lambda_6\lambda_7 + \lambda_7^2 - 4\lambda_{11}\left(\lambda_6 + \lambda_7\right)\big)/18 + 2\lambda_9 f_o^2\,, \\
16\pi^2\beta_{\lambda_{10}} =& + 8\lambda_3^2 + 4\lambda_{10}^2 + 7\lambda_{11}^2/18 - \left(2\lambda_4\lambda_4^* - 4\lambda_4^*\lambda_5 - 4\lambda_5^*\lambda_4 + 2\lambda_5\lambda_5^*\right)/3 \\
&+ \lambda_{10}\left(\lambda_6/6 + \lambda_7/6 + 19\lambda_{11}/6 + 4\lambda_8 + 3\lambda_9\right) + \lambda_9\lambda_{11} \\
&+ \big(\lambda_6^2 - 10\lambda_6\lambda_7 + \lambda_7^2 - 4\lambda_{11}\left(\lambda_6 + \lambda_7\right)\big)/18 + 2\lambda_{10} f_o^2\,, \\
16\pi^2\beta_{\lambda_{11}} =& - \lambda_6^2 - \lambda_7^2 + \lambda_{11}^2/4 + 6\left(\lambda_4\lambda_4^* + \lambda_5\lambda_5^*\right) \\
&+ 3\lambda_{10}\left(\lambda_6 + \lambda_7\right) + 7\lambda_{11}\left(\lambda_6 + \lambda_7 + \lambda_8\right)/2 + 2\lambda_{11} f_o^2\,.
\end{aligned}
\tag{A.3}
$$

Appendix B

RGEs for the ISS scenario in the composite scheme

The RGEs corresponding to the model in Ch. 4 are (using the $SU(5)$ convention $3g_1^2 = 5g'^2$ for the $U(1)$ factor):

- gauge couplings:

$$\beta_{g_1} = \frac{41}{10} g_1^3 \,, \qquad \beta_{g_2} = -\frac{19}{6} g_2^3 \,, \qquad \beta_{g_3} = -7 g_3^3 \,. \tag{B.1}$$

- Yukawa couplings:

$$\begin{aligned} \beta_{y_t} &= y_t \left(\frac{9}{2} y_t^2 - 8 g_3^2 - \frac{9}{4} g_2^2 - \frac{17}{20} g_1^2 + y_\nu^2 \right) \,, \\ \beta_{y_\nu} &= y_\nu \left(\frac{5}{2} y_\nu^2 + \frac{1}{2} y_s^2 + 3 y_t^2 - \frac{9}{20} \left(5 g_2^2 + g_1^2 \right) \right) \,, \\ \beta_{y_s} &= y_s \left(2 y_s^2 + y_\nu^2 \right) \,. \end{aligned} \tag{B.2}$$

- quartic couplings:

$$\begin{aligned} \beta_{\lambda_H} =& + 12 \lambda_H^2 + \frac{27}{100} g_1^4 + \frac{9}{10} g_1^2 g_2^2 + \frac{9}{4} g_2^4 + \lambda_H \left(12 y_t^2 - \frac{9}{5} g_1^2 - 9 g_2^2 + 4 y_\nu^2 \right) \\ & + 2 \lambda_{HS}^2 - 4 y_\nu^4 - 12 y_t^4 \,, \\ \beta_{\lambda_S} =& + 10 \lambda_S^2 + 4 \lambda_S y_s^2 + 4 \lambda_{HS}^2 - 4 y_s^4 \,, \\ \beta_{\lambda_{HS}} =& + \lambda_{HS} \left(4 \lambda_{HS} + 6 \lambda_H + 4 \lambda_S + 2 y_\nu^2 + 2 y_s^2 + 6 y_t^2 - \frac{9}{10} g_1^2 - \frac{9}{2} g_2^2 \right) - 4 y_s^2 y_\nu^2 \,. \end{aligned} \tag{B.3}$$

Appendix C

Boltzmann equations for $1 \leftrightarrow 2$ processes

In this appendix, we consider the effects of decays and inverse decays, dubbed $1 \leftrightarrow 2$ processes, in the evolution of the DM number density, identified as particle 2 for the moment. Let us consider, in general, only the process $1 \leftrightarrow 2\,3$ among the particles, and then the collisional ($C[f]$) operator, Eq. (1.62), is expressed as

$$\frac{g_2}{(2\pi)^3}\int C\left[f_2\right]\frac{d^3p}{E} = \int\left[f_1\left(1\pm f_2\right)\left(1\pm f_3\right)\mid M_{1\to 2,3}\mid^2 - f_2 f_3\left(1\pm f_1\right)\mid M_{2,3\to 1}\mid^2\right] \\ \left(2\pi\right)^4\delta^4\left(p_1-p_2-p_3\right)\frac{d^3p_1}{\left(2\pi\right)^3 2E_1}\frac{d^3p_2}{\left(2\pi\right)^3 2E_2}\frac{d^3p_3}{\left(2\pi\right)^3 2E_3}\,. \tag{C.1}$$

Time invariance ensures: $\mid M_{1\to 2,3}\mid^2 = \mid M_{2,3\to 1}\mid^2$ and we will make the following three assumptions: (i) approximate $1-f_i \sim 1+f_i \sim 1$, (ii) detail balance among the equilibrium distributions $f_1^{eq} = f_2^{eq} f_3^{eq}$ and (iii) only the particle 1 is in thermal equilibrium with the heat bath. Then the r.h.s. of Eq. (C.1) is expressed as

$$= \int \mid M_{1\to 2,3}\mid^2\left[f_2^{eq}f_3^{eq} - f_2 f_3\right]\left(2\pi\right)^4\delta^4\left(p_1-p_2-p_3\right)\frac{d^3p_1}{\left(2\pi\right)^3 2E_1}\frac{d^3p_2}{\left(2\pi\right)^3 2E_2}\frac{d^3p_3}{\left(2\pi\right)^3 2E_3}\,, \tag{C.2}$$

and

$$\int\left(2\pi\right)^4\delta^4\left(p_1-p_2-p_3\right)\frac{d^3p_2}{\left(2\pi\right)^3 2E_2}\frac{d^3p_3}{\left(2\pi\right)^3 2E_3} = \int d\Omega\frac{\sqrt{\lambda\left(s,m_2^2,m_3^2\right)}}{32\pi^2 s}\,. \tag{C.3}$$

Then

$$\frac{g_2}{(2\pi)^3}\int C\left[f_2\right]\frac{d^3p}{E}=\int \mid M_{1\to 2,3}\mid^2\left[f_2^{eq}f_3^{eq}-f_2f_3\right]\frac{d^3p_1}{\left(2\pi\right)^3 2E_1}d\Omega\frac{\sqrt{\lambda\left(s,m_2^2,m_3^2\right)}}{32\pi^2 m_1 s}\,, \tag{C.4}$$

and[1]

$$\begin{aligned}\frac{g_2}{(2\pi)^3}\int C\left[f_2\right]\frac{d^3p}{E}&=\int\left[f_2^{eq}f_3^{eq}-f_2f_3\right]\frac{d^3p_1}{\left(2\pi\right)^3 E_1}m_1\Gamma\,,\\ \Gamma&=\int d\Omega\frac{\sqrt{\lambda\left(s,m_2^2,m_3^2\right)}}{64\pi^2 m_1 s}\mid M_{1\to 2,3}\mid^2\,.\end{aligned} \tag{C.5}$$

Under the assumption that the equilibrium and non-equilibrium distributions are proportional by a factor that does not depend on the momentum, it follows that for any function of momentum $g(p)$ [93, 94],

$$\int f_2(p)g(p)\frac{d^3p}{\left(2\pi\right)^3}=\frac{\int f_2^{eq}(p)g(p)\frac{d^3p}{\left(2\pi\right)^3}}{g_2\int f_2^{eq}(p)\frac{d^3p}{\left(2\pi\right)^3}}n_2\,. \tag{C.6}$$

Then, if we take 2 and 3 to be the same particle χ,

$$\frac{g_\chi}{(2\pi)^3}\int C\left[f_\chi\right]\frac{d^3p}{E}=\Gamma_{1\to 2,3}\left[n_{\chi,eq}^2-n_\chi^2\right]\,. \tag{C.7}$$

And $\Gamma_{1\to 2,3}$ is the thermally-average decay width of particle 1 [94],

$$\boxed{\Gamma_{1\to 2,3}=\frac{\int f_1^{eq}\frac{d^3p_1}{\left(2\pi\right)^3 E_1}m_1\Gamma}{n_{\chi,eq}^2}}\,. \tag{C.8}$$

From the equality between the Liouville ($\hat{L}[f]$) and collisional ($C[f]$) operators we can obtain the Boltzmann equation, in a similar manner to Eq. (1.72) for 2 ↔ 2 processes, as

$$\frac{x}{Y_{\chi,eq}}\frac{dY_\chi}{dx}=-\frac{sY_{\chi,eq}\Gamma_{1\to 2,3}}{H\left(T\right)}\left(\left(\frac{Y_\chi}{Y_{\chi,eq}}\right)^2-1\right)\,. \tag{C.9}$$

And for the Boltzmann distribution the previous can be simplified to (see Eq. (6.6)

---

[1] The function Γ would correspond to the zero-temperature decay rate of particle 1 after the substitution $s\to m_1^2$.

in Ref. [201]):

$$\int f_1^{eq} \frac{d^3 p_1}{(2\pi)^3} \frac{m_1 \Gamma}{E_1} = \frac{m_1^2 \Gamma}{2\pi^2} T K_1 \left(\frac{m_1}{T}\right) . \tag{C.10}$$

However, in general, if no particle is assumed to be in thermal equilibrium, the collisional operator for the process 1 ↔ 2 3 is (focusing on the evolution of particle 1 for illustration)

$$\begin{aligned} \frac{g_1}{(2\pi)^3} \int C[f_1] \frac{d^3 p}{E} &= - \int [f_1 - f_2 f_3] \mid M_{1\to 2,3} \mid^2 (2\pi)^4 \delta^4 (p_1 - p_2 - p_3) \\ &\quad \frac{d^3 p_1}{(2\pi)^3 2E_1} \frac{d^3 p_2}{(2\pi)^3 2E_2} \frac{d^3 p_3}{(2\pi)^3 2E_3} \\ &= - \int [f_1 - f_2 f_3] \frac{d^3 p_1}{(2\pi)^3 E_1} m_1 \Gamma . \end{aligned} \tag{C.11}$$

Then

$$\frac{g_1}{(2\pi)^3} \int C[f_1] \frac{d^3 p}{E} = -\Gamma_{1\to 2,3} \left(n_1 - \frac{n_2 n_3}{n_2^{eq} n_3^{eq}} n_1^{eq} \right) , \tag{C.12}$$

where the detailed balance assumption has been taken. And $\Gamma_{1\to 2,3}$ is,

$$\boxed{\Gamma_{1\to 2,3} = \frac{\int f_1^{eq} \frac{d^3 p_1}{(2\pi)^3 E_1} m_1 \Gamma}{n_1^{eq}}} . \tag{C.13}$$

For illustration, consider now that the particles 2 and 3 are in thermal equilibrium with the thermal bath, then Eq. (C.12) is simply written as

$$\frac{g_1}{(2\pi)^3} \int C[f_1] \frac{d^3 p}{E} = -\Gamma_{1\to 2,3} \left(n_1 - n_1^{eq} \right) , \tag{C.14}$$

and we can express it as in Eq. (C.9):

$$\frac{x}{Y_{1,eq}} \frac{dY_1}{dx} = -\frac{\Gamma_{1\to 2,3}}{H(T)} \left(\frac{Y_1}{Y_{1,eq}} - 1 \right) . \tag{C.15}$$

Note how different are Eqs. (C.9) and (C.15), which is due to consider diverse particles in thermal equilibrium.

Appendix D

β_{ijk} coefficients of two-real scalar model

	Linear
$\beta_{h\theta\theta}$	$\frac{s_\alpha\left(m_\theta^2 - m_h^2\right)}{v_s}$
$\beta_{\rho\theta\theta}$	$-\frac{c_\alpha\left(m_\theta^2 - m_\rho^2\right)}{v_s}$
$\beta_{h\rho\rho}$	$c_\alpha s_\alpha\left(\frac{s_\alpha\left(m_h^2 + 2m_\rho^2\right)}{v} - \frac{c_\alpha\left(m_h^2 - 3m_\theta^2 + 2m_\rho^2\right)}{v_s}\right)$

	Quadratic	*Quartic*
$\beta_{h\theta\theta}$	$-\frac{m_h^2 s_\alpha}{v_s}$	$-\frac{s_\alpha\left(m_h^2 + 2m_\theta^2\right)}{v_s}$
$\beta_{\rho\theta\theta}$	$\frac{m_\rho^2 c_\alpha}{v_s}$	$\frac{c_\alpha\left(m_\rho^2 + 2m_\theta^2\right)}{v_s}$
$\beta_{h\rho\rho}$	$-\frac{c_\alpha s_\alpha\left(m_h^2 + 2m_\rho^2\right)\left(v c_\alpha - s_\alpha v_s\right)}{v v_s}$	$-\frac{c_\alpha s_\alpha\left(m_h^2 + 2m_\rho^2\right)\left(v c_\alpha - s_\alpha v_s\right)}{v v_s}$

	Cubic
$\beta_{h\theta\theta}$	$-\frac{s_\alpha\left(m_h^2 + m_\theta^2\right)}{v_s}$
$\beta_{\rho\theta\theta}$	$\frac{c_\alpha\left(m_\rho^2 + m_\theta^2\right)}{v_s}$
$\beta_{h\rho\rho}$	$\frac{1}{3}c_\alpha s_\alpha\left(\frac{3s_\alpha\left(m_h^2 + 2m_\rho^2\right)}{v} - \frac{c_\alpha\left(3m_h^2 + m_\theta^2 + 6m_\rho^2\right)}{v_s}\right)$

Table D.1: Expressions for the β_{ijk} coefficients in the minimal models in terms of the physical parameters defined in Sec. 6.1.

Appendix E

Friedmann Equation

Regarding the description of the space-time where particles are present, we assume the following. At sufficiently large scales, the Universe is considered to be approximately homogeneous and isotropic, and it can fall into one of the three categories: closed, open and flat; where the space is a 3-dimensional sphere, hyperboloid and plane with a parameter κ describing them as $\kappa = +1$, $\kappa = 1$ and $\kappa = 0$ respectively. The current observations suggest to consider the Universe as spatially flat and so we approximate $\kappa \approx 0$. Accordingly the appropriate metric is the so-called Friedmann-Lemaitre-Robertson-Walker metric (FLRW) [94, 96, 202]:

$$ds^2 = dt^2 - a(t)^2 \, \delta_{ij} dx^i dx^j \, , \tag{E.1}$$

and the expansion depends on the function of time $a(t)$, called the scale factor. For this spatially flat space it is usual to introduce the Hubble parameter H defined as

$$H(t) = \frac{\dot{a}(t)}{a(t)} \, . \tag{E.2}$$

The evolution of the expansion is determined by the *Einstein equation*:

$$R_{\mu\nu} - \frac{1}{2} g_{\mu\nu} R = 8\pi G T_{\mu\nu} \, . \tag{E.3}$$

Eq. (E.3) provides two differential equations for the evolutions of a and ρ, which is the total energy density that describes the energy-momentum tensor $T_{\mu\nu}$; G is the Newton gravity constant The 00-component of Eq. (E.3) gives a first relation between the Hubble parameter and the total energy density ρ as,

$$H^2 = \frac{8\pi}{3} G\rho - \frac{\kappa}{a^2} \, , \tag{E.4}$$

which is called *Friedmann equation.* And the second relation comes from the covariant conservation of the energy-momentum tensor, $\partial_\mu T^{\mu\nu} = 0$:

$$\dot{\rho} + 3\frac{\dot{a}}{a}\left(\rho + p\right) = 0\,, \tag{E.5}$$

and p is the total pressure density. When particles are relativistic the energy density is expressed as

$$\rho = \frac{\pi^2}{30} g_* T^4\,, \tag{E.6}$$

where $g_*(T)$ accounts for the effective number of relativistic degrees of freedom, see Fig. 1.10. The Friedmann equation, Eq. (E.4), can be written as ($G = M_{pl}^{-2}$, the Planck mass is $M_{pl} \approx 10^{19}\,\mathrm{GeV}$):

$$H = 1.66\sqrt{g_*}\frac{T^2}{M_{pl}}\,, \tag{E.7}$$

in the radiation dominated era.